70-80-C-0053-2 / TR-83-13

POLYMERIC MICROELECTRONICS

June 1983

Prepared for the

US Army Night Vision and Electro-Optics Laboratory

Fort Belvoir, VA 22060

by

Stephen T. Kowel
Dennis S. Cleverly
I. H. Loh
Edward Balizer
George C. Martin
Philipp G. Kornreich
B. K. Srinivasan

DEPARTMENT OF ELECTRICAL AND COMPUTER ENGINEERING

SYRACUSE UNIVERSITY

Syracuse, NY 13210

REPORT DOCUMENTATION PAGE		READ INSTRUCTIONS BEFORE COMPLETING FORM
1. REPORT NUMBER DAAK70-80-C-0053-2	**2. GOVT ACCESSION NO.**	**3. RECIPIENT'S CATALOG NUMBER**
4. TITLE *(and Subtitle)* Polymeric Microelectronics		**5. TYPE OF REPORT & PERIOD COVERED** Final 5/80 - 12/82
		6. PERFORMING ORG. REPORT NUMBER TR-83-13
7. AUTHOR(s) Stephen T. Kowel, Edward Balizer, T.T. Su, I.H. Loh. Dennis Cleverly, George Martin, and Philipp G. Kornreich.		**8. CONTRACT OR GRANT NUMBER(s)** DAAK70-80-C-0053
9. PERFORMING ORGANIZATION NAME AND ADDRESS Department of Electrical & Computer Engineering 111 Link Hall, Syracuse University Syracuse, NY 13210		**10. PROGRAM ELEMENT, PROJECT, TASK AREA & WORK UNIT NUMBERS** 62709A 1L162709Dh95 00 00105
11. CONTROLLING OFFICE NAME AND ADDRESS U.S. Army Night Vision and Electro-Optics Laboratory Fort Belvoir, VA 22060		**12. REPORT DATE** 6/1/83
		13. NUMBER OF PAGES 160
14. MONITORING AGENCY NAME & ADDRESS*(if different from Controlling Office)*		**15. SECURITY CLASS.** *(of this report)* Unclassified
		15a. DECLASSIFICATION/DOWNGRADING SCHEDULE

16. DISTRIBUTION STATEMENT *(of this Report)*

Distribution list;
Distribution unlimited.

17. DISTRIBUTION STATEMENT *(of the abstract entered in Block 20, if different from Report)*

18. SUPPLEMENTARY NOTES

The support for this work was provided by the Advanced Concept Team, Office
of the Director of Army Research, Department of the Army, DAMA-ZE,
Washington, D.C. 20310

19. KEY WORDS *(Continue on reverse side if necessary and identify by block number)*

Polymers, microstructures, adaptive optics, liquid crystals, adaptive lenses,
adaptive mirrors.

20. ABSTRACT *(Continue on reverse side if necessary and identify by block number)*

This report contains the results of more than two years' effort to examine
applications for microelectronics and integrated optics of several classes of
organic materials. The first class was ultraviolet curable elastomers; the
second was liquid crystals.

The principal goal of studying the elastomers was to create microstructures
that could be electroded and deformed under applied voltage. Although

DD _{1 JAN 73} **FORM 1473**   EDITION OF 1 NOV 65 IS OBSOLETE   UNCLASSIFIED

theoretical calculations indicated that deformations of as much as 20 percent could be obtained, experimental values fell far short of this. However, as a result of this work it was learned that such materials as polydimethylsiloxane (PDMS) could be electroded with conductive and reflective metallic films by evaporation at low temperatures.

As a result of our experimental work on PDMS, we also found that it was highly transparent and could be formed into optical waveguides which could be integrated with silicon or gallium arsenide technology since it is processed at room temperature. It appears that such a material can act as a host for a variety of species, such as lasing dyes which could permit the creation of optically pumped microlasers. The development of lasing and modulating components based on doped polymers has significant promise.

Significant progress was made in the evaluation of liquid crystals for use in adaptively controlled refractive optics. Extensive theoretical study revealed that a liquid crystal lens employing several hundred electrodes should be capable of near diffraction limited optical performance. By appropriately calibrating such a device, followed by adjusting the voltages on electrodes, arbitrary phase front modification can be obtained for polarized light. The use of linear electrodes would require a lens composed of four cells in order to accommodate two orthogonal polarizations for plane polarized light. Experimental work confirmed all of the major concepts based on a very crude cylindrical lens with only nine linear electrodes in operation. Such lenses, if they can be improved and operated adaptively under microprocessor control, could have significant applications where weight, cost, and size make mechanically controlled lenses impractical.

INTRODUCTION

This report contains the results of more than two years' effort to examine applications for microelectronics and integrated optics of several classes of organic materials. The first class was ultraviolet curable elastomers; the second was liquid crystals.

The principal goal of studying the elastomers was to create micro-structures that could be electroded and deformed under applied voltage. Although theoretical calculations indicated that deformations of as much as 20 percent could be obtained, experimental values fell far short of this. However, as a result of this work it was learned that such materials as polydimethylsiloxane (PDMS) could be electroded with conductive and reflective metallic films by evaporation at low temperatures.

As a result of our experimental work on PDMS, we also found that it was highly transparent and could be formed into optical waveguides which could be integrated with silicon or galluim arsenide technology since it is processed at room temperature. It appears that such a material can act as a host for a variety of species, such as lasing dyes which could permit the creation of optically pumped microlasers. The development of lasing and modulating components based on doped polymers has significant promise.

Significant progress was made in the evaluation of liquid crystals for use in adaptively controlled refractive optics. Extensive theoretical study revealed that a liquid crystal lens employing several hundred elec-trodes should be capable of near diffraction limited optical performance. By appropriately calibrating such a device, followed by adjusting the

voltages on electrodes, arbitrary phase front modification can be obtained for polarized light. The use of linear electrodes would require a lens composed of four cells in order to accommodate two orthogonal polarizations for plane polarized light. Experimental work confirmed all of the major concepts based on a very crude cylindrical lens with only nine linear electrodes in operation. Such lenses, if they can be improved and operated adaptively under microprocessor control, could have significant applications where weight, cost, and size make mechanically controlled lenses impractical.

This report is divided into two major sections, the first devoted to the research on elastomers, the second devoted to liquid crystals. Each of these major sections are self-contained with its own table of contents and numbering of pages and figures.

PART A. LIQUID CRYSTAL ADAPTIVE OPTICS

ABSTRACT

The creation of a field controlled variation of the index of refraction in a liquid crystal cell has been analyzed and experimentally verified. To obtain a spherical lens utilizing a simple electrode structure and capable of focussing arbitrary incoming polarizations requires four flat, nematic liquid crystal cells. With electrodes fabricated well within the current capability of photolithography, near diffraction limited performance in terms of the Optical Transfer Function is predicted.

The focussing capability of a liquid crystal lens was demonstrated using a single cell with linear transparent electrodes. A planoconvex cylindrical lens for a single incoming polarization was thus created. While the cell had a very crude electrode structure, it affirmed all of the major qualitative predictions. The fringing along the edge of the electrodes, required for eventually obtaining near diffraction limited performance, was observed.

TABLE OF CONTENTS

LIST OF FIGURES

NOMENCLATURE

a	Width of transparent electrodes and also the width of space between electrodes
$\overline{B}$	Magnetic flux density
c	Speed of light in a vacuum
$\overline{D}$	Electric displacement
$\overline{d}$	Nematic director
D_i	Component of the electric displacement in the ith direction
d_i	Distance from a lens to the image
$\overline{E}$	Electric field vector
E_i	Component of the electric field vector in the ith direction
f_x	Spatial frequency coordinate
f_y	Spatial frequency coordinate perpendicular to f_x
f	Focal Length
$H(f_x, f_y)$	Optical transfer function
k	Wave number
$\overline{\ell}$	Unit vector in direction of wave propagation
ℓ	Width of square aperture and liquid crystal lens
L	Width of square aperture
MTF	Modulation Transfer Function, the modulus of the OTF
n	Index of refraction
n(x,y)	Index of refraction variable in both x and y
n(r)	Index of refraction varying radially
n_θ	The index of refraction obtained when the nematic director is at an angle θ with the direction of light propagation

Δ_ε Equal to $\varepsilon_o (\varepsilon - \varepsilon)$

$\varepsilon_{||}$ Dielectric constant parallel to $\overline{d}$

$\varepsilon_\perp$ Dielectric constant perpendicular to $\overline{d}$

ε_o Permittivity of free space

ε_{ij} Components of the permittivity tensor

$\phi(x,y)$ Spatially varying phase delay

λ Wavelength of light

$\chi_{||}$ Susceptibility per unit volume parallel to $\overline{d}$

$\chi_\perp$ Susceptibility per unit volume perpendicular to $\overline{d}$

θ_m Maximum nematic director angle

μ_o Permeability of free space

1. INTRODUCTION

Lenses are classically created by varying the optical path length over an aperture by radially shaping a medium with a fixed index of refraction. If the structure has parallel walls but the index of refraction is appropriately varied, the same effect can be achieved.

This paper describes how a series of flat liquid crystal cells can be operated with appropriate electrode voltages to create focussing of light. Calibration and adaptive operation of such lenses would be performed by dedicated microprocessors. Applications for such lightweight, inexpensive systems might include camera optics, telescopy, and robot vision systems. Combined with conventional optics, the liquid crystal lenses could provide adaptive focussing and scanning of optical beams for laser beam technology. The advantages of spatial phase modulation of optical beams without mechanical motion could significantly modify the design of sophisticated optical systems.

All crystals under the influence of an electric field or applied stress exhibit birefringence (1). That is, the index of refraction can be varied. In solids, however, this effect is small since only small distortions of the indicatrix are made. Liquid crystals are unique since the molecules re-orient under the influence of applied electric or magnetic fields (2, 3, 4, 5, 6). In addition, nematic liquid crystals are uniaxial and the optical axis is coincident with the molecular axis. Thus, as the molecules re-orient in the presence of a field, the entire indicatrix is rotated creating large changes in the index of refraction.

Liquid crystals can be divided into two groups. If the dielectric tensor is such that the component along the molecular axis (also the optical axis) is greater than the component perpendicular to the axis $(\epsilon_{||} > \epsilon_{\perp})$, the crystal is said to have positive dielectric anisotropy (PDA). These molecules align parallel to an applied field. If the reverse is true $(\epsilon_{||} < \epsilon_{\perp})$, the crystal possesses negative dielectric anisotropy (NDA). In this case, the molecules will align perpendicular to an applied field. Either type can be used for creation of a lens. Only the voltages applied to the electrodes will differ.

Consider the case of a positive liquid crystal. In order to have a workable lens, the molecules would be in a homogeneous alignment without any voltages applied, the axes of all the molecules aligned in the same direction parallel to the cell walls. This preferential direction for the molecules is established when the cell is fabricated and can be accomplished in a number of ways (7, 8, 9). The simplest method is preferential rubbing of the inside surfaces prior to assembly. As the voltage across the electrodes is increased above threshold, the molecules tend to align with the field. At saturation, all but those molecules "anchored" to the two surfaces will be aligned with the field. If the preferential direction is in the x-direction, then as the molecules move the index of refraction for a wave traveling in the z-direction and polarized in the y-direction remains constant.

Thus Figure 1 with the light traveling in the z-direction shows a configuration which with appropriately applied voltages could be a cross-section of a lens for light polarized in the x-direction. To account for a y-polarized component a second stage would be required.
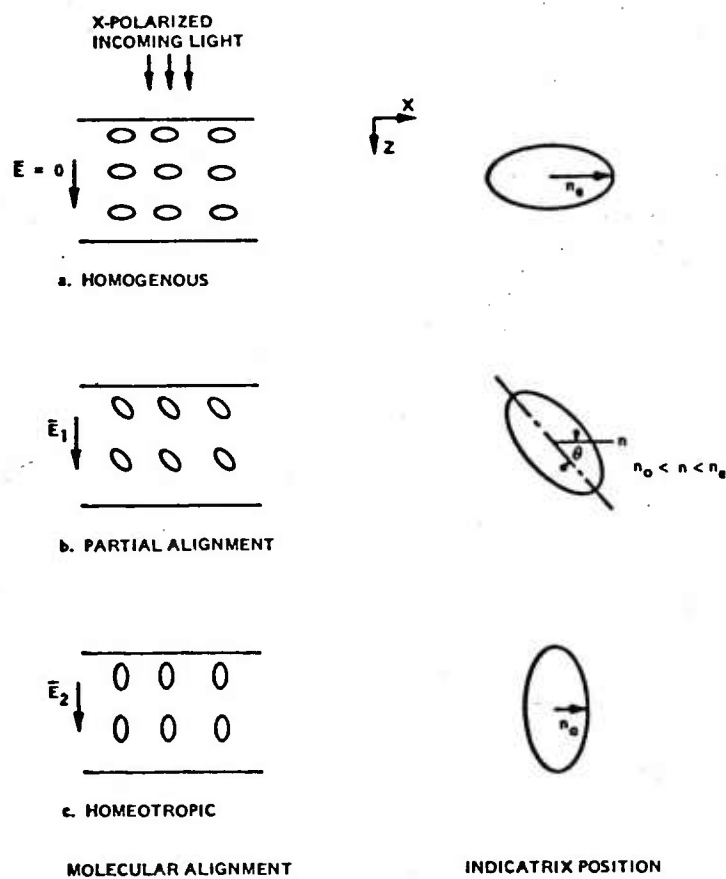
Figure 1-1. DIRECTOR ORIENTATION FOR VARIATION OF THE INDEX OF REFRACTION. VOLTAGES INCREASE FROM TOP TO BOTTOM FOR POSITIVE DIELECTRIC ANISOTROPY.

This would be an identical stage but with the preferential direction in the y-direction.

Once we have determined the required phase delay variation in Section II, we shall estimate the required nematic director variation in Section III. From the literature, it is then possible to obtain the required addressing voltages. Section IV describes the cell and electrode configuration for dealing with plane polarized monochromatic light. The optical performance of the lens is computed in Section V.

Section VI reviews the first experimental verification of the liquid crystal lens concept.

2. CREATION OF A THIN LENS BY INDEX OF REFRACTION VARIATION

Consider a material of thickness Δ and variable index of refraction $n(x,y)$ centered on the z-axis in the x-y plane. A wave at coordinates (x,y) will suffer a phase delay in passing through the material given by

$$\phi(x,y) = k\Delta n(x,y) \tag{2-1}$$

where

$$k = \frac{2\pi}{\lambda} = \text{wave number of incoming light}$$

and

$$\lambda = \text{wavelength}$$

Assume that the index of refraction can be varied as

$$n(r) = A + Br^2 \tag{2-2}$$

where

$$r^2 = x^2 + y^2 \tag{2-3}$$

At the center of the cell, $r = 0$, the index of refraction has its maximum value.

$$n(r = 0) = n_e \tag{2-4}$$

At the outer edge of the cell $(r = r_o)$ the index of refraction is less than the extraordinary index of refraction and greater than or equal to the ordinary value.

$$n(r = r_o) = n_i \tag{2-5}$$

where

$$n_o \leq n_i < n_e \tag{2-6}$$

Using the boundary conditions in (2-4) and (2-5), the index of refraction variation becomes

$$n(r) = n_e + (\frac{n_i - n_e}{r_o^2})r^2 \qquad (2\text{-}7)$$

The resulting transmission function is

$$t(r) = \exp(jk\Delta n) = \exp[(jk\Delta)(n_e + \frac{n_i - n_e}{r_o^2})r^2] \qquad (2\text{-}8)$$

Since $n_e > n_i$

$$t(r) = \exp(jk\Delta n_e)\exp[(-jk\Delta)(\frac{n_e - n_i}{r_o^2})r^2] \qquad (2\text{-}9)$$

Comparing this expression to that commonly used for a spherical lens

$$t_\ell(r) = \exp(jk\Delta n)\ \exp(-j\frac{k}{2f}r^2) \qquad (2\text{-}10)$$

the focal length can be seen to be

$$\frac{1}{f} = \frac{2\Delta(n_e - n_i)}{r_o^2} \qquad (2\text{-}11)$$

From the limits on n_i

$$0 < \frac{1}{f} \le \frac{2\Delta(n_e - n_i)}{r_o^2} \qquad (2\text{-}12)$$

Figure 2 illustrates this limitation. Using a given material, in this case MBBA (4-methoxybenzylidine-4'-n-butylanaline) for which n_e = 1.8062 and n_o = 1.5616 at λ = 0.5145 micron (8) the allowable focal lengths are constrained by lens thickness and required aperture size.
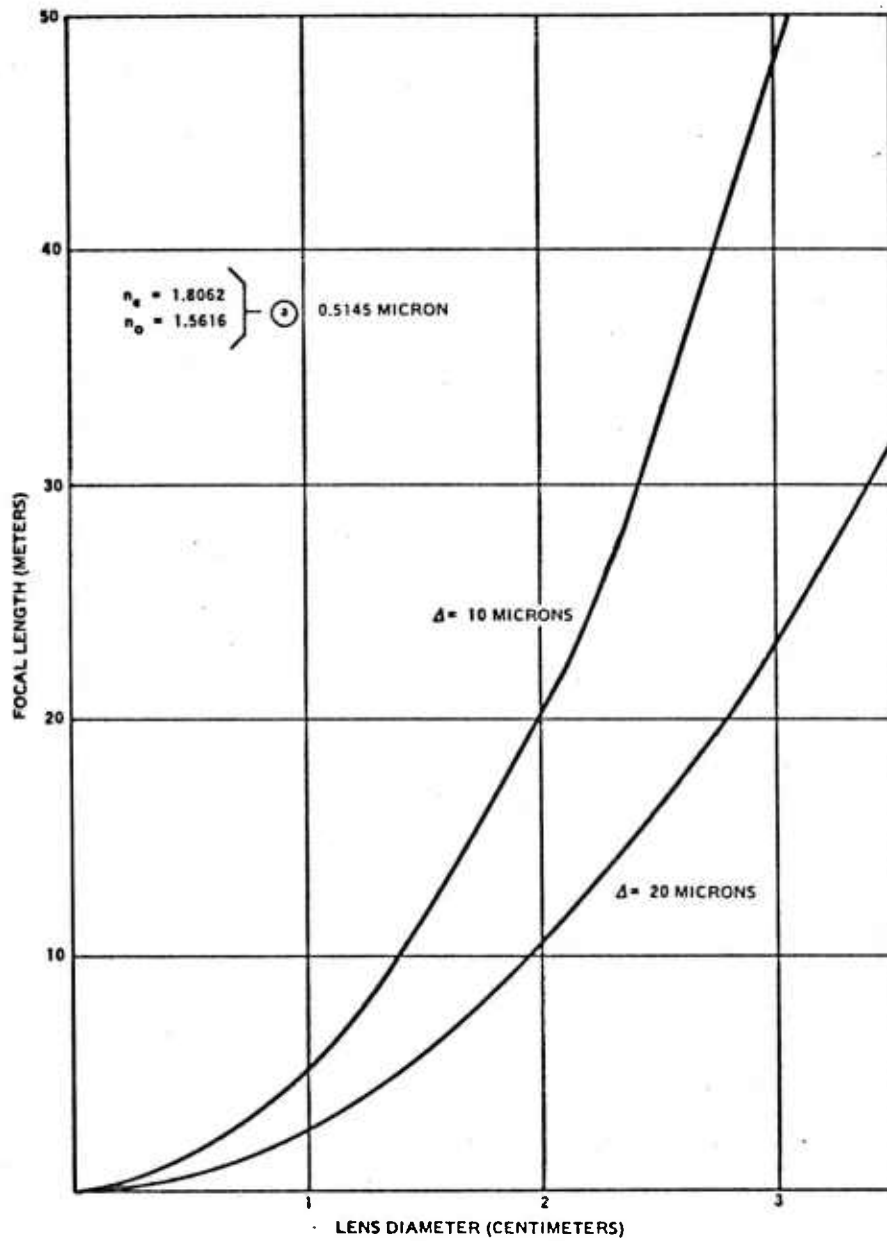
Figure 2-1. FOCAL LENGTH LIMITATIONS USING MBBA

The two lens thicknesses chosen are representative of liquid crystal cells used in display applications. Obviously, the small cell thickness coupled with the given $n_e - n_o$ do not allow large lenses and short focal lengths.

All nematic liquid crystals are positive crystals. They belong to the class of materials whose extraordinary refractive index exceeds the ordinary refractive index.

3. NEMATIC DIRECTOR ORIENTATION TO MATCH INDEX OF REFRACTION VARIATION

Liquid crystals are characterized by an orientational order of their constituent rod-like molecules (8, 10). In nematic liquid crystals this orientational order has uniaxial symmetry, the axis of symmetry being parallel to a unit vector, $\bar{d}$, called the director. The indicatrix formulation applies but since the orientation of the liquid crystal molecules can be altered under application of an external field, the orientation of the indicatrix can be changed. This is analogous to re-orienting a solid so that light passing through it is affected by a different index of refraction. Figure 1 illustrates this phenomenon. In this example, a positive liquid crystal possessing positive dielectric anisotrophy is shown at the top of the figure in the homogeneous state. Correspondingly, the indicatrix is aligned so that a wave polarized in the x-direction is influenced by an index of refraction of n_e. At the bottom of the figure, the orientation has been altered to the homeotropic state, in which case, the same polarized light encounters an index of refraction n_o. At an intermediate point, the index of refraction is dependent on θ, the direction of the nematic director.

Consider the slice of the indicatrix shown in Figure 3. Light propagating in the z-direction and polarized in the x-direction would be influenced by an index of refraction n_e when the indicatrix is not rotated (major axis along x and minor axis along z). However, when the indicatrix is rotated through an angle θ, that same ray is influenced by an index of refraction n_θ.
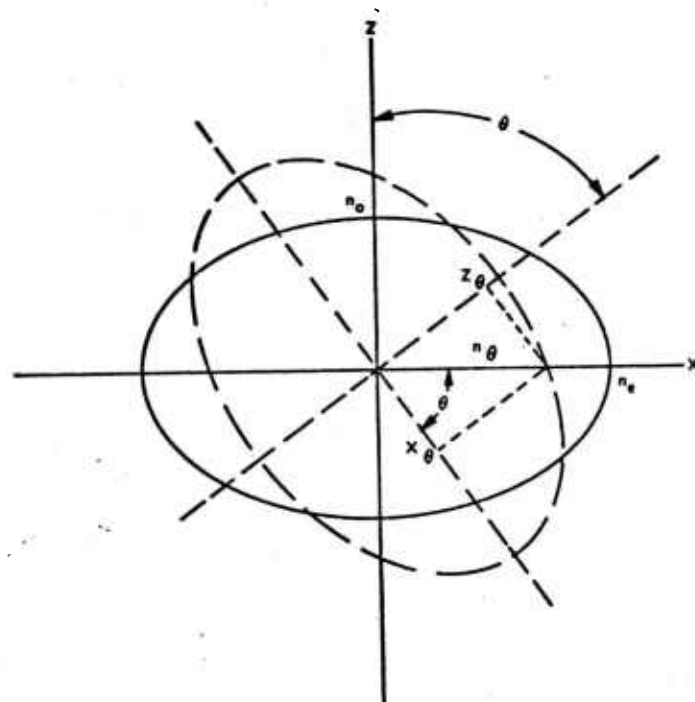
Figure 3-1. GEOMETRY TO CALCULATE CHANGE IN INDEX OF REFRACTION
WITH LIQUID CRYSTAL MOLECULE ORIENTATION.

The slice of the indicatrix shown can be expressed as

$$\frac{x_\theta^2}{n_e^2} + \frac{y_\theta^2}{n_o^2} = 1 \tag{3-1}$$

But

$$n_\theta^2 = x_\theta^2 + y_\theta^2 \tag{3-2}$$

so Equation (3-1) can be written

$$\frac{n_\theta^2 - y_\theta^2}{n_e^2} + \frac{y_\theta^2}{n_o^2} = 1 \tag{3-3}$$

Equivalently,

$$y_\theta = \sqrt{(1 - n_\theta^2/n_e^2)/(1/n_o^2 - 1/n_e^2)} \tag{3-4}$$

From the geometry of Figure 3

$$\theta = \sin^{-1}\sqrt{(1/n_\theta^2 - 1/n_e^2)/(1/n_o^2 - 1/n_e^2)} \tag{3-5}$$

For any desired index of refraction between n_o and n_e, Equation (3-5) gives the required θ or orientation of the nematic crystal director. Note that indeed when $n_\theta = n_e$, $\theta = 0^o$ and when $n_\theta = n_o$, $\theta = 90^o$.

Since the nematic liquid crystals do not align uniformly across the cell in the thickness direction, a more useful form of Equation (3-5) is obtained by solving for n_θ, yielding

$$n_\theta = n_e \bigg/ \sqrt{1 + \sin^2\theta \left[\frac{n_e^2}{n_o^2} - 1\right]} \tag{3-6}$$

This expression gives the index of refraction for light polarized in the x-direction and travelling in the z-direction as a function of the angular orientation of the nematic liquid crystals in the x-z plane. Note that since liquid crystals are uniaxial, light propagation in the z-direction and polarized in the y-direction would be influenced by the index of refraction n_o independent of the orientation change in the x-z plane.

The variation in the thickness direction is caused primarily by the strong anchoring of the molecules at the walls. Below threshold all molecules align in the homogeneous direction. Above threshold, the molecules close to the walls remain in this orientation, with a gradual transition to the orientation θ. At higher voltages, the θ orientation is achieved throughout the vast majority of the cell(8,10).

As an illustration, Figure 4 shows the variation of index of refraction in MBBA as a function of nematic director orientation.

At this junction, we need to calculate the voltages required to obtain these director orientations. This calculation describes the equilibrium conditions in three dimensions as a function of viscous, elastic, and electrical forces. The solution reveals the existence of a voltage threshold, as well as the details of the voltage variation. Figure 5 depicts a typical result. (8,10,14,15)
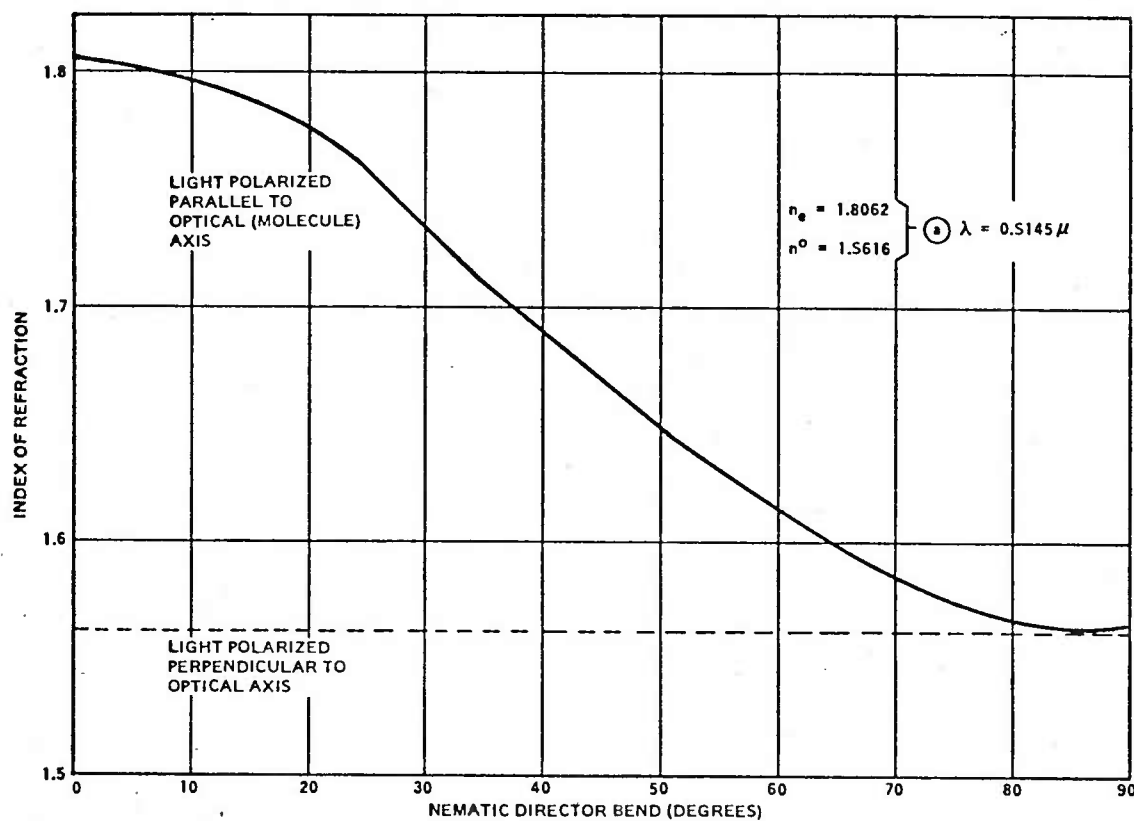
Figure 3-2.   INDEX OF REFRACTION VARIATION WITH CHANGING DIRECTOR
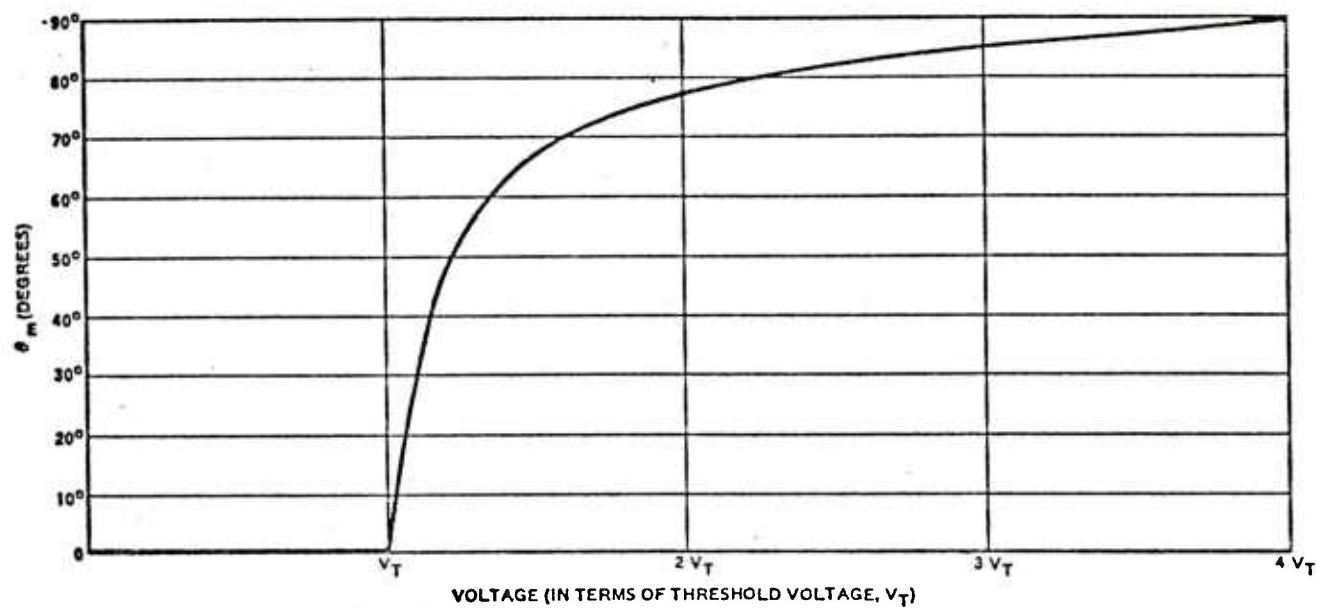ORIENTATION IN MBBA.

Figure 3-3. DIRECTOR ANGLE AS A FUNCTION OF VOLTAGE FOR MBBA.

4. TOTAL LENS CONFIGURATION

It has been assumed to this point that electrodes could be configured to give the required radial variation in index of refraction. Since the voltage variation desired is radial, it would appear that radially symmetric electrodes would be ideal. However, radially symmetric electrodes require difficult mask fabrication and connections made to them could create obscuration of a sector of the device. Row-and column-addressable, rectangular grid electrodes like those used in commercially available liquid crystal displays could be considered. In this case, addressing individual electrodes is easy and mask fabrication is a simple process. However, such electrodes do not inherently possess the symmetry of a lens. Thus, the structure would appear to cause aberrations.

To understand how the correct symmetry can be obtained, consider a square aperture of width L centered at the origin. Let the transmission of the aperture be given by

$$t(x,y) = \text{rect}\left(\frac{x}{L}\right) \text{rect}\left(\frac{y}{L}\right) \exp[jk\Delta n(x)] \qquad (4\text{-}1)$$

where

$$n(x) = n_e - \frac{x^2}{2f}$$

Just past the aperture, if it is illuminated by a unit-amplitude, normally incident plane wave, the field component U is

$$U(x,y) = \text{rect} \left(\frac{y}{L}\right) \text{rect}\left(\frac{x}{L}\right) \exp \left[jk\Delta(n_e - \frac{x^2}{2\Delta f})\right] \qquad (4\text{-}2)$$

Ignoring the constant phase term

$$U(x,y) = \text{rect} \left(\frac{y}{L}\right) \text{rect} \left(\frac{x}{L}\right) \exp \frac{-jkx^2}{2\Delta f} \qquad (4\text{-}3)$$

If there was another transmission factor t_2 directly in front of the aperture with

$$n(y) = n_e - \frac{y^2}{2\Delta f} \qquad (4\text{-}4)$$

then

$$U = t_1(x,y) \, t_2(x,y) \qquad (4\text{-}5)$$

$$U = \text{rect} \left(\frac{y}{L}\right) \text{rect} \left(\frac{x}{L}\right) \exp \frac{-jk(x^2 + y^2)}{2f} \qquad (4\text{-}6)$$

Thus the ideal form of a lens can, in theory, be obtained with linear electrodes. By cascading two stages, the mask fabrication is simplified, and the required symmetry is maintained.

Figure 6 shows a single stage cross section and a representative electrode structure. Note that one side is a uniform ground electrode. Recall that the variation in voltage profile can be used to generate a change in index of refraction for either x or y polarized light. If the preferential direction of the liquid crystal director is in the x-direction, only the component of the light polarized in that direction will be affected.

GLASS   SPACER   GLASS

INSULATING
FILM

SIGNAL
ELECTRODES

SIDE VIEW OF CELL

SOLID ELECTRODE

FRONT VIEW OF
SIGNAL ELECTRODE

NOTE:
BOTH INTERIOR
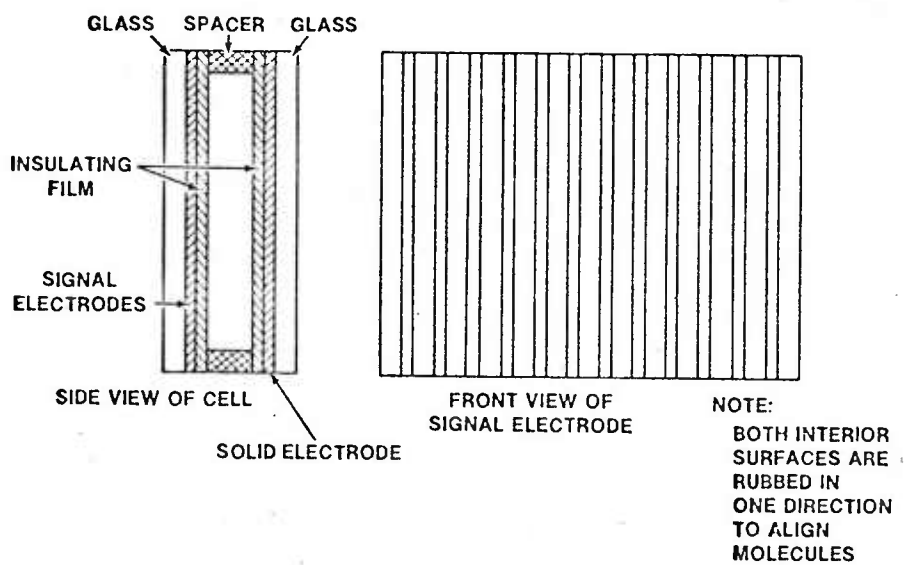SURFACES ARE
RUBBED IN
ONE DIRECTION
TO ALIGN
MOLECULES

Figure 4-1.   SINGLE STAGE OF LIQUID CRYSTAL LENS

To obtain a complete spherical lens,four stages are required.
"Complete" means that any incoming polarization is given the appro-
priate phase transform of a thin lens. Figure 7 illustrates the
functions of the four stages. The first stage gives the appropriate
variation in index of refraction in the x-direction for light polarized
in the x-direction. Similarly, the second stage varies the index of
refraction in the y-direction but still only for light polarized in
the x-direction. Thus, if a lens was to be created for x-polarized
light only, the first two stages would be sufficient. The last two
stages repeat the process but now for the component polarized in the
y-direction.

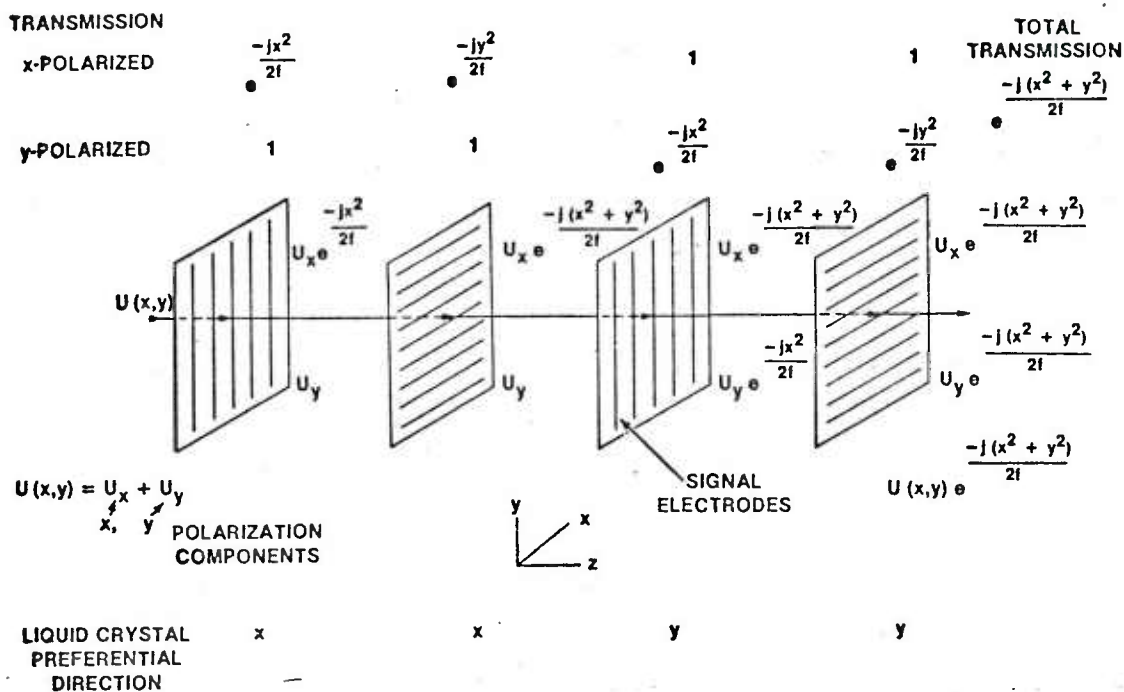Figure 8 shows the cross section of the four-stage liquid crystal
lens.

Figure 4-2. FUNCTIONS OF THE FOUR STAGES IN A LIQUID CRYSTAL LENS. U_x AND U_y CONTAIN UNIT POLARIZATION VECTORS IN THE x-AND y-DIRECTIONS RESPECTIVELY.
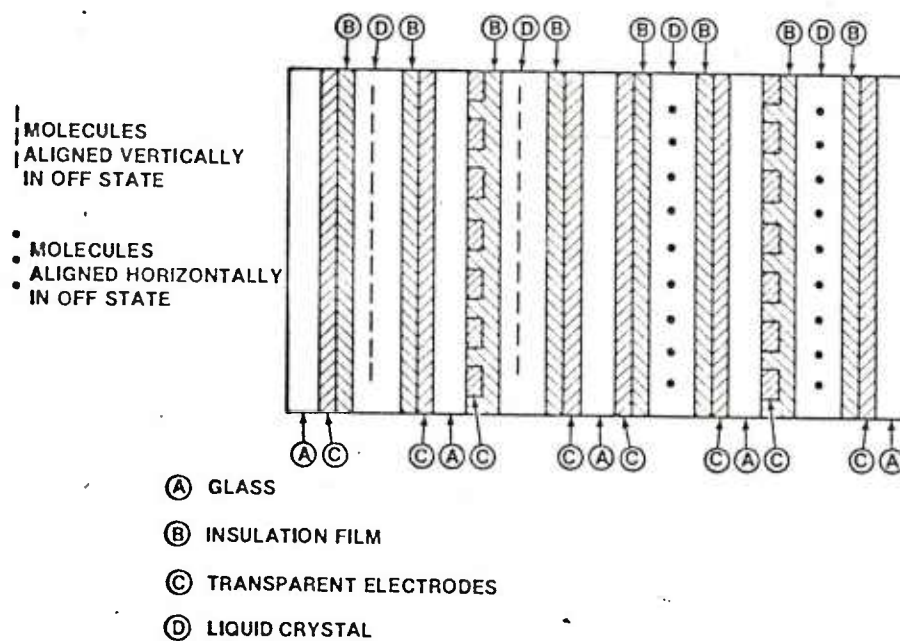

Figure 4-3. FOUR-STAGE LIQUID CRYSTAL LENS.

5. LIQUID CRYSTAL LENS PERFORMANCE ANALYSIS

Although the lens described previously possesses the radial symmetry in index of refraction variation of a common circular lens, by its construction it presents a square exit or entrance aperture. There is no loss in general applicability by considering the performance of the square configuration since either a round or rectangular field stop would be placed in the lens chain whose size would become the limiting factor or the square configuration could be the desired format (for example in television, infrared, or photographic systems with 1 x 1 formats). The main source of aberrations is the discrete nature of the electrodes, and therefore of the index variation.

The common measure of lens fidelity is the Modulation Transfer Function (MTF), which is the modulus of the Optical Transfer Function (OTF) which specifies the complex weighting factor applied by the system to the spatial frequency component at (f_x, f_y) relative to the weighting factor applied to the zero frequencies component.

To evaluate the OTF of the liquid crystal lens, it is first necessary to examine the diffraction limited square lens.

5.1 Diffraction Limited Square Aperture

Following the nomenclature of Goodman (11), the OTF of a diffraction limited system can be written as

$$H(f_x, f_y) = \frac{\displaystyle\int_{-\infty}^{\infty}\int_{-\infty}^{\infty} P\left(\xi + \frac{\lambda d_1 f_x}{2}, \eta + \frac{\lambda d_1 f_x}{2}\right) P\left(\xi - \frac{\lambda d_1 f_x}{2}, \eta - \frac{\lambda d_1 f_y}{2}\right) d\xi d\eta}{\displaystyle\int_{-\infty}^{\infty}\int_{-\infty}^{\infty} P(\xi, \eta)\, d\xi d\eta} \qquad (5\text{-}1)$$

where

$P(x,y)$ = the pupil function

λ = wavelength of light

d_1 = distance from the pupil to the image

and

f_x, f_y = spatial frequencies

If

$$P(x,y) = \text{rect}\left(\frac{x}{\ell}\right) \text{rect}\left(\frac{y}{\ell}\right) \qquad (5\text{-}2)$$

then

$$\int_{-\infty}^{\infty}\int_{-\infty}^{\infty} P(\xi, \eta)\, d\xi d\eta = \int_{-\ell/2}^{\ell/2}\int_{-\ell/2}^{\ell/2} d\xi d\eta = \ell^2 \qquad (5\text{-}3)$$

and

$$\int_{-\infty}^{\infty}\int_{-\infty}^{\infty} P\left(\xi + \frac{\lambda d_1 f_x}{2}, \eta + \frac{\lambda d_1 f_y}{2}\right) P\left(\xi - \frac{\lambda d_1 f_x}{2}, \eta - \frac{\lambda d_1 f_y}{2}\right) d\xi d\eta =$$

$$\int_{-\ell + \frac{\lambda d_1 |f_x|}{2}}^{\ell - \frac{\lambda d_1 |f_x|}{2}} \int_{-\ell + \frac{\lambda d_1 |f_y|}{2}}^{\ell - \frac{\lambda d_1 |f_y|}{2}} d\xi d\eta = (\ell - \lambda d_1 |f_x|)(\ell - \lambda d_1 |f_y|)$$

$$\qquad (5\text{-}4)$$

where

$$\left| f_x \right| \leq \frac{\ell}{\lambda d_i}$$

and

$$\left| f_y \right| \leq \frac{\ell}{\lambda d_i}$$

Substituting Equations (5-3) and (5-4) into Equation (5-1) yields

$$H(f_x, f_y) = \begin{cases} \dfrac{(\ell - \lambda d_i \left| f_x \right|)(\ell - \lambda d_i \left| f_y \right|)}{\ell^2} & \left| f_x \right| \text{ and } \left| f_y \right| \leq \dfrac{\ell}{\lambda d_i} \\[2em] 0 & \text{elsewhere} \end{cases}$$

(5-5)

Let

$$f_c \triangleq \frac{\ell}{\lambda d_i} \qquad (5\text{-}6)$$

f_c then defines the spatial frequency along the axes where the OTF goes to zero. Using the definition of the triangle function, the OTF of the diffraction limited, square aperture can finally be written as

$$H(f_x, f_y) = \Lambda(f_x/f_c) \, \Lambda(f_y/f_c) \qquad (5\text{-}7)$$

5.2 OTF Of The Liquid Crystal Lens

Due to the electrode structure used to create the index of refraction variation in the liquid crystal, a diffraction limited lens cannot be formed. The wavefront leaving the lens will have phase distortions caused by the approximation of a smoothly varying index

of refraction by a sampled function. Thus, the liquid crystal lens
will inherently have aberrations. The effect of these aberrations
on lens performance as measured by the predicted OTF is the goal
of this section.

The common method for analytically describing aberrations is to
model them as a phase-shifting plate. If the phase error at a point
(x,y) in the aperture is repesented by $kW(x,y)$ where $k = \frac{2\pi}{\lambda}$ and W is
an effective path-length error, then the complex transmittance t of
the phase-shifting plate is given by

$$t(x,y) = P(x,y) \exp [jkW(x,y)] \qquad (5\text{-}8)$$

where $P(x,y)$ is the pupil function used in the previous section.
The complex function t is called the generalized pupil function.

Again following the nomenclature of Goodman (11), let $\alpha(f_x, f_y)$
be the area of overlap of

$$P(\xi + \frac{\lambda d_i f_x}{2}, \eta + \frac{\lambda d_i f_y}{2}) \text{ and } P(\xi - \frac{\lambda d_i f_x}{2}, \eta - \frac{\lambda d_i f_x}{2})$$

With aberrations the OTF can be written as

$$H(f_x, f_y) =$$

$$\frac{\displaystyle\iint\limits_{\alpha(f_x, f_y)} \exp \left\{ jk[W(\xi + \frac{\lambda d_i f_x}{2}, \eta + \frac{\lambda d_i f_y}{2}) - W(\xi - \frac{\lambda d_i f_x}{2}, \eta - \frac{\lambda d_i f_x}{2})] \right\} d\xi d\eta}{\displaystyle\iint\limits_{\alpha(0,0)} d\xi d\eta} \qquad (5\text{-}9)$$

For the liquid crystal lens described previously, since the modula-
tions of the index of refraction in x and y are accomplished in

successive stages, the spatial frequency relations are independent and

Equation (5-9) can be written

$$H(f_x,f_y) = \frac{\int_{\alpha(f_x)} \exp\{jk[W(\xi+\frac{\lambda d_i f_x}{2}) - W(\xi-\frac{\lambda d_i f_x}{2})]\} \, d\xi}{\int_{\alpha(0)} d\xi} \; x$$

$$\frac{\int_{\alpha(f_y)} \exp\{jk[W(\eta+\frac{\lambda d_i f_y}{2}) - W(\eta-\frac{\lambda d_i f_y}{2})]\} \, d\eta}{\int_{\alpha(0)} d\eta} \tag{5-10}$$

Only one of the terms (stages in the lens) needs to be considered since the effect in the x-direction is numerically equivalent to that in the y-direction.

Consider the electrode configuration depicted in Figure 9. The electrodes have appropriate voltages applied so that the index of refraction is appropriately sampled at

$$x = \pm \frac{(4m+1)a}{2} \; ; \quad m = 0,1,2,\dots \frac{N+1}{2}$$

and N is the number of electrodes. Assuming that the field underneath each electrode is uniform, the error in the index of refraction under the electrode is

$$\delta n(x) = \overbrace{\left(n_e - \frac{x^2}{2\Delta f}\right)}^{\text{Ideal}} - \overbrace{\left(n_e - \frac{x_o^2}{2\Delta f}\right)}^{\text{Created}} = \frac{x_o^2 - x^2}{2\Delta f} \tag{5-11}$$

where

$$x_o - \frac{a}{2} \le x \le x_o + \frac{a}{2}$$

where x_o represents the center of an electrode.

In the spaces between electrodes it is assumed that cross-talk or "meshing", exists. The spacings are small enough so that the liquid crystal molecules react to a field strength the magnitude of which varies smoothly between that of the bordering fields established by the two electrodes. If this cross-talk is symmetric, the index of refraction would also be appropriately sampled at

$$x = \pm \frac{(2m+1)a}{2} \qquad m = 1,2, \ldots$$

The dotted segments in Figure 10 illustrate this cross-talk within the spacings.

To account for the cyclic nature of the error in index of refraction and the increasing error with distance from the center due to the quadratic phase required, the error in index of refraction is modelled as

$$\delta n(x) = -a^2 \left[\frac{N^2 - (N - \frac{1}{2})^2}{2\Delta f} \right] \cos \left(\frac{\pi x}{a} \right) \qquad (5\text{-}12)$$

Equivalently,

$$\delta n(x) = - \left[\frac{(N - \frac{1}{4})a^2}{2\Delta f} \right] \cos \left(\frac{\pi x}{a} \right) \qquad (5\text{-}13)$$

The variation given in Equation (5-11) has been given a constant worst case value since it has been scaled to the largest error (found at the outside radius).
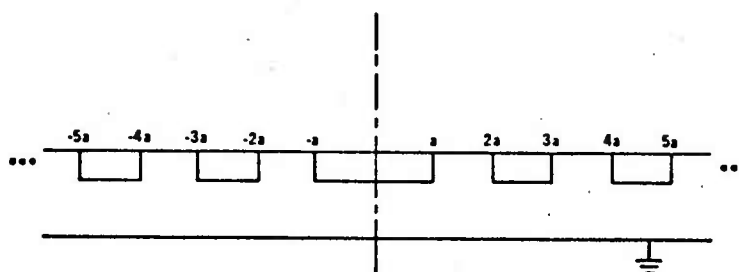
Figure 5-1.   LIQUID CRYSTAL ELECTRODE CONFIGURATION FOR
LENS PERFORMANCE ANALYSIS.   THE CENTER
ELECTRODE WAS CHOSEN TO BE TWICE AS WIDE
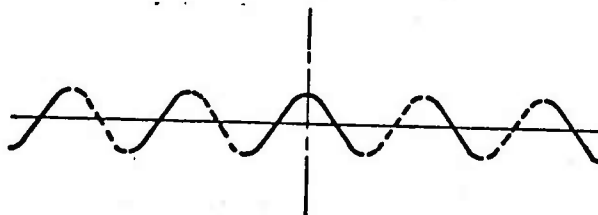FOR CONVENIENCE IN CALCULATION.

Figure 5-2.   ASSUMED ERROR IN INDEX OF REFRACTION

Now

$$W(x) = \Delta\delta n(x) = -a^2 \left[\frac{N - \frac{1}{4}}{2f} \right] \cos\left(\frac{\pi x}{a}\right) \tag{5-14}$$

Using this expression in the numerator of the first integral of Equation (5-10) yields

$$N(f_x) = \int_{\alpha(f_x)} \exp'\left\{jk\left[W(\xi + \frac{\lambda d_i f_x}{2}) - W(\xi - \frac{\lambda d_i f_x}{2})\right]\right\} d\xi = \tag{5-15}$$

$$\int_{\alpha(f_x)} \exp\left[-jka^2 \frac{N - \frac{1}{4}}{2f} \right] \left[\cos\left(\frac{\pi[\xi + \frac{\lambda d_i f_x}{2}]}{a}\right) - \cos\left(\frac{\pi[\xi - \frac{\lambda d_i f_x}{2}]}{a}\right)\right] d\xi$$

Using standard trigonometric identities Equation (5-15) can be expanded to

$$N(f_x) =$$

$$\int_{\alpha(f_x)} \exp\left\{\left[-jka^2 \frac{N - \frac{1}{4}}{2f}\right]\right\}\left[\left(\cos\frac{\pi\xi}{a}\cos\frac{\pi\lambda d_i f_x}{2a} - \sin\frac{\pi\xi}{a}\sin\frac{\pi\lambda d_i f_x}{2a}\right)\right.$$

$$\left. - \left(\cos\frac{\pi\xi}{a}\cos\frac{\pi\lambda d_i f_x}{2a} + \sin\frac{\pi\xi}{a}\sin\frac{\pi\lambda d_i f_x}{2a}\right)\right]\right\} d\xi \tag{5-16}$$

Equvalently,

$$N(f_x) = \int_{\alpha(f_x)} \exp\ jka^2\left[\frac{N - \frac{1}{4}}{f}\right]\ \sin\frac{\pi\xi}{a}\sin\frac{\pi\lambda d_i f_x}{2a}\ d\xi \tag{5-17}$$

For simplicity, let

$$A = \frac{ka^2[N - \frac{1}{4}]}{f}\ \sin\frac{\pi\lambda d_i f_x}{2a} \tag{5-18}$$

So

$$N(f_x) = \int_{\alpha(f_x)} \exp\{j\Lambda \sin\frac{\pi\xi}{a}\} \, d\xi \tag{5-19}$$

This expression can be evaluated by expanding the integrand in Taylor series and integrating term by term.

The first term is

$$\int_{\alpha(f_x)} 1 \, d\xi = \int_{\frac{-\ell+\lambda d_i|f_x|}{2}}^{\frac{\ell-\lambda d_i|f_x|}{2}} d\xi = \ell - \lambda d_i|f_x| \tag{5-20}$$

The second term yields

$$\int_{\alpha(f_x)} jA \sin\frac{\pi\xi}{a} \, d\xi = \int_{\frac{-\ell+\lambda d_i|f_x|}{2}}^{\ell-\lambda d_i|f_x|} jA \sin\frac{\pi\xi}{a} \, d\xi$$

$$= -jA \frac{a}{\pi} [\cos\frac{\pi}{a}(\frac{\ell-\lambda d_i|f_x|}{2}) - \cos\frac{\pi}{a}(\frac{-\ell+\lambda d_i|f_x|}{2})]$$

$$= 0 \tag{5-21}$$

The third term is

$$-\int_{\alpha(f_x)} \frac{A^2}{2} \sin^2 \frac{\pi\xi}{a} \, d\xi = -\int_{\frac{-\ell+\lambda d_i|f_x|}{2}}^{\frac{\ell-\lambda d_i|f_x|}{2}} \frac{A^2}{2} \sin^2 \frac{\pi\xi}{a} \, d\xi = -\frac{a}{\pi}\frac{A^2}{2} \int_{\frac{\pi}{a}[\frac{-\ell+\lambda d_i|f_x|}{2}]}^{\frac{\pi}{a}[\frac{\ell-\lambda d_i|f_x|}{2}]} \sin^2 Z \, dZ$$

$$= \frac{-A^2 a}{2\pi} \left[\frac{Z}{2} - \frac{\sin 2Z}{4} \right]\Bigg|_{\frac{\pi}{a}[\frac{-\ell+\lambda d_i|f_x|}{2}]}^{\frac{\pi}{a}[\frac{\ell-\lambda d_i|f_x|}{2}]}$$

$$= \frac{-A^2 a}{2\pi} \left[\frac{\pi}{2a}(\ell - \lambda d_i|f_x|) - \frac{\sin}{4}(\frac{\pi}{a}[\ell - \lambda d_i|f_x|]) + \frac{\sin}{4}(\frac{\pi}{a}[\ell - \lambda d_i|f_x|]) \right]$$

$$= \frac{-A^2 a}{2\pi} \left[\frac{\pi}{2a}(\ell - \lambda d_i|f_x|) - \frac{1}{2} \sin (\frac{\pi}{a}[\ell - \lambda d_i|f_x|]) \right] \tag{5-22}$$

The fourth term goes to zero and the rest of the terms in the series are negligible. Therefore, the numerator, $N(f_x)$, can be found by substituting (5-20),(5-21), and (5-22) into (5-19) yielding

$$N(f_x) = [\ell - \lambda d_i|f_x|] - \frac{A^2 a}{2\pi} \left[\frac{\pi}{2a}(\ell - \lambda d_i|f_x|) + \frac{1}{2} \sin (\frac{\pi}{a}[\ell - \lambda d_i|f_x|]) \right] \tag{5-23}$$

Equivalently,

$$H(f_x) = [1 - \frac{A^2}{4}] (\ell - \lambda d_i|f_x|) + \frac{A^2 a}{4\pi} \sin (\frac{\pi}{a}[\ell - \lambda d_i|f_x|]) \tag{5-24}$$

Since

$$H(f_x) = \frac{N(f_x)}{\int_{\alpha(0)} d\xi} = \frac{N(f_x)}{\ell} \tag{5-25}$$

Then

$$H(f_x) = [1 - \frac{A^2}{4}][\frac{\ell - \lambda d_i |f_x|}{\ell}] + \frac{A^2 a}{4\pi\ell} \sin \frac{\pi}{a} [\ell - \lambda d_i |f_x|] \tag{5-26}$$

Equivalently,

$$H(f_x) = [\frac{1-A^2}{4}][\frac{\ell - \lambda d_i |f_x|}{\ell}] + \frac{A^2}{4}[\frac{\sin \frac{\pi}{a}[\ell - \lambda d_i |f_x|]}{\frac{\pi}{a}[\ell - \lambda d_i |f_x|]}][\frac{\ell - \lambda d_i |f_x|}{\ell}] \tag{5-27}$$

This can be written as

$$H(f_x) = [1 - \frac{A^2}{4} + \frac{A^2}{4} \text{sinc} (\frac{\ell - \lambda d_i |f_x|}{a})] \ \Lambda (\frac{f_x}{f_c}) \tag{5-28}$$

Figures 11 and 12 compare two configurations with the diffraction limit for the aperture they fill.

Note that the complete optical transfer function is

$$H(f_x, f_y) = H(f_x) H(f_y) \tag{5-29}$$

Each of the factors on the right hand side are of the form given in Equation (5-28). Figures 14 and 15 depict appropriate data along either axis in the spatial frequency domain.
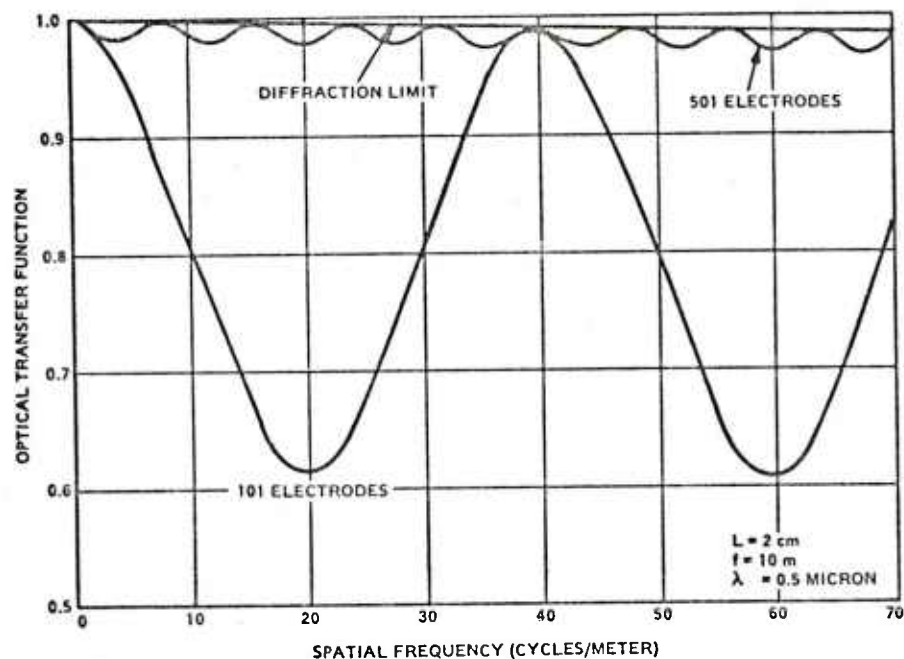
Figure 5-3. OPTICAL TRANSFER FUNCTION OF LIQUID CRYSTAL LENS
FOR LOW FREQUENCY.
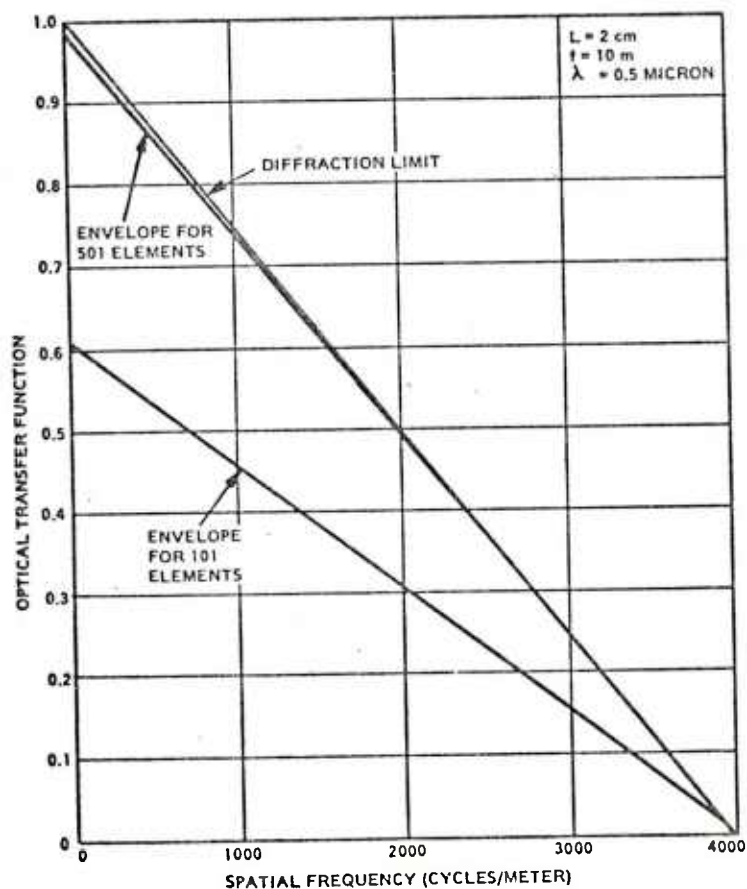
Figure 5-4. OPTICAL TRANSFER FUNCTION OF LIQUID CRYSTAL LENS
FOR HIGH FREQUENCY.

The Optical Transfer Function of the entire four-cell lens is accounted for in Equation (5-29). Consider incoming light polarized in the x-direction. Two of the cells are transparent to it (the nematic director being in the y-direction). The effect of the other two cells is given by Equation (5-29). Just the reverse is true for the component polarized in the y-direction.

The importance of this calculation is that it predicts that a lens of several hundred elements should be capable of near diffraction limited performance. To calibrate and control a cell of this complexity would require a dedicated microprocessor system.

6. EXPERIMENTAL VERIFICATION

To show empirically that a liquid crystal cell could be used
to create a lens, a cell was designed and fabricated. An appropriate
holder was built and the cell mounted. Index of refraction variation
with voltage change data was taken, and then finally the device was
tested as a lens.

Liquid Crystal Cell

The cell tested was fabricated by Dr. Donald Castleberry at
the GE Corporate Research and Development Center. The walls were
made of pieces of glass (2 9/16" x 1 1/2" x 1/16" and 2 1/2" x 1 1/2" x
1/8"). The thin piece had a solid transparent electrode and the thick
one had linear electrodes running the length of the glass. These
electrodes were spaced 36 lines per inch. The electrode material is
a transparent indiun-tin oxide film 20 $\overset{o}{A}$ thick and 0.72 mm
wide. Electrodes are covered with an insulating layer of silicon
dioxide. The two pieces of glass were separated by a teflon spacer
12 microns thick. Before assembly the interior surface was rubbed
to anchor the liquid crystal molecules at the surfaces in a direction
perpendicular to the linear electrodes. With the glass-spacer sand-
wich glued, E44, a liquid crystal available commercially from BDH
Chemicals, was drawn under vacuum through a hole drilled in one piece
of glass, filling the cell. Since the glass had been rubbed on both
interior surfaces in the same direction, the molecules went to the
homogeneous or parallel alignment. The hole was sealed leaving the
cell ready for mounting. E44 was chosen since it had the largest

birefringence ($n_e - n_o = 0.262$) of any broad temperature range mixture available.

A mounting fixture was fabricated out of epoxy glass. Connections are made to individual electrodes by using single, pressure maintaining connectors. Because the connectors above the contact points are wider than the electrode runs, they had to be mounted in three staggered rows. A hole was cut in the holder at the opposite end from these connectors to allow continuity checking after assembly.

Birefringence Measurement

To appropriately drive electrodes to have the cell function as a lens, the change in index of refraction as a function of voltage must be known.

Two experimental techniques were considered for measuring the index of refraction changes: interferometry and birefringence. Interferometry could be used to compare the index of refraction of the liquid crystal under any two electrodes. Using the two electrodes as slits and having one in the off-state (no applied voltage), the shift in the observed interference pattern created by a laser beam passing through both slits would be a measure of the index of refraction difference (12). To accurately measure differences in the index of refraction, shifts in the interference pattern of less than 1 mm at a distance of 5 meters would have to be measured.

By putting the cell between crossed polarizers and measuring the light transmitted as a function of voltage, induced birefringence gives a straightforward method of determining the index of refraction change. Also, liquid crystal cells had been tested previously in this manner (5,8,13) and the results could be compared before proceeding to test the cell as a lens. For these reasons, birefringence was chosen as the method for determining the index of refraction change with variation of the applied voltage.

Birefringence Experimental Arrangement

To measure birefringence, the laser passes through a polarizer and is broken down into two components that pass through the liquid crystal cell. An analyzer passes the portions of these two components matching its polarization axis. Finally, a radiometer collects and measures the transmitted radiation.

In analytical terms, the anticipated irradiance at the radiometer can be described by the expression (8,10,12)

$$I = I_p \sin^2 2\phi \sin^2 \left(\frac{\gamma}{2}\right) \qquad (6\text{-}1)$$

where

$$\gamma = \frac{2\pi\Delta\delta n}{\lambda} \qquad (6\text{-}2)$$

and I = Irradiance at the radiometer

I_p = Irradiance if the polarizer and analyzer were parallel

ϕ = Angle between the liquid crystal molecule preferential direction and the polarizer direction

Δ = Thickness of the liquid crystal layer

λ = Wavelength of the light

δn = Change in index of refraction

To maximize the $\sin^2 2\phi$ term, the cell is mounted at 45° to both the polarizer and analyzer polarization directions. That is, the preferential direction of the liquid crystal molecules is midway between the polarization directions of the polarizer and analyzer.

The device was connected directly to the signal generator with all the electrodes activated. The rms voltage applied to the electrodes was monitored on a digital voltmeter. Light passing through the analyzer was collected by the radiometer and the corresponding current output displayed on an oscilloscope. In this manner, the voltage output of the signal gnerator could be varied and the resulting change in light level measured. What was anticipated was a variation in the observed radiometer output that as a function of applied voltage would closely approximate a sine squared function. From the periodicity of that curve, the index of refraction as a function of voltage could be obtained.

Results of Birefringent Experiments

Birefringence measurements were taken at several different laser wavelengths. Also, for comparison, two different signal generator frequencies were used while the optical wavelength was held constant. Figure 13 shows a typical result. The oscilloscope reading is shown indicating the radiometer output as a function of the rms input voltage as indicated by a digital volt meter.
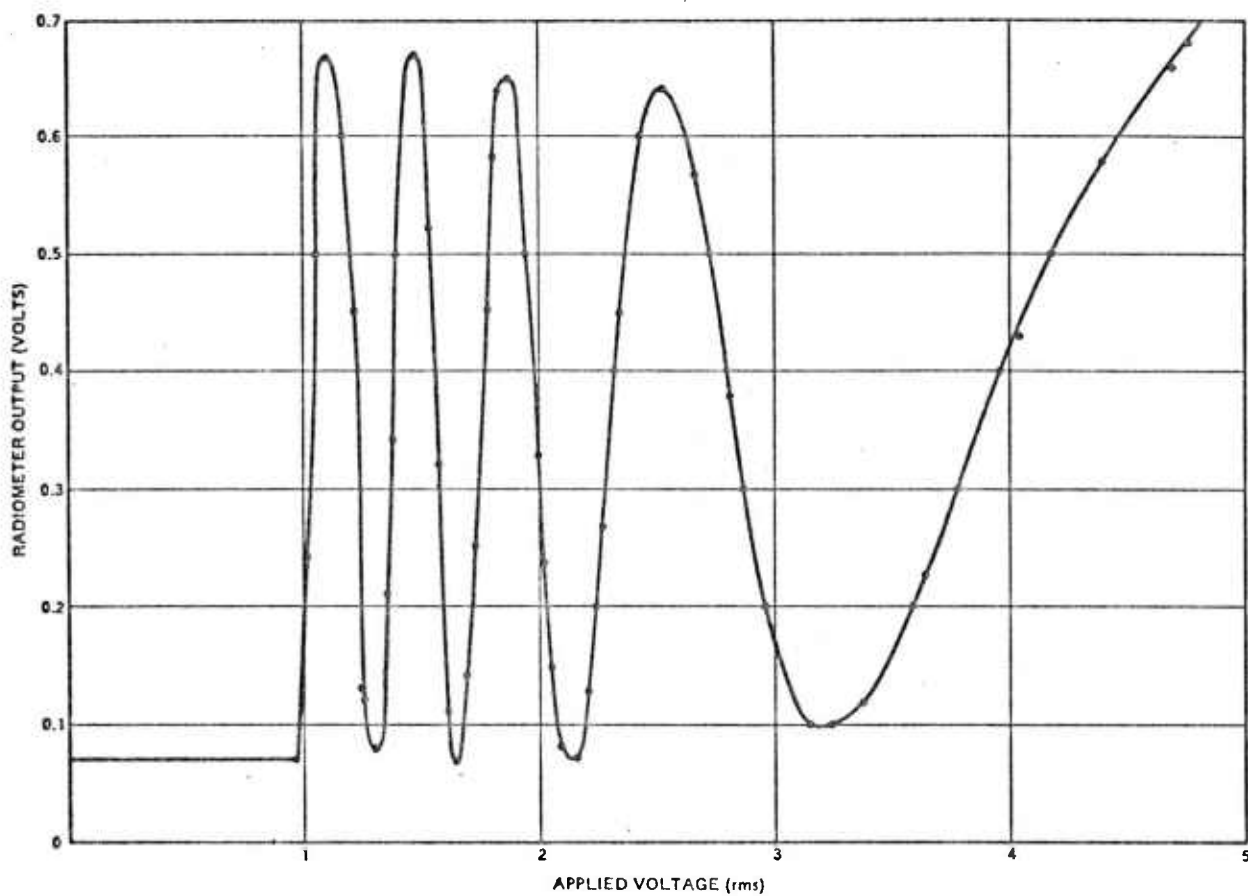
Figure 6-1. BIREFRINGENCE TEST RESULTS AT 200 Hz (λ = 633 nm)

All experiments with 200 Hz and 400 Hz excitation exhibit the anticipated sine squared dependency and are virtually identical. The anticipated sine squared dependency was also found at the 514.5 nm and 457.9 nm argon ion laser lines.

The index of refraction change with voltage variation can be obtained from the birefringence data and Equations (6-1) and (6-2). Each half cycle (maximum to minimum or minimum to maximum) of the data corresponds to γ changing by π. For example, in the case of the helium neon laser, one half cycle represents

$$\delta n = \frac{\lambda}{2d} = \frac{0.633 \times 10^{-6} m}{2(12 \times 10^{-6} m)}$$

$$\delta n = 0.026 \quad (\lambda = 633 \text{ nm}) \tag{6-3}$$

Similarly,

$$\delta n = 0.0214 \quad (\lambda = 514.5 \text{ nm}) \tag{6-4}$$

and

$$\delta n = 0.019 \quad (\lambda = 457.9 \text{ nm}) \tag{6-5}$$

Now by plotting this δn variation against the voltage required to obtain a half-cycle variation, the desired index of refraction versus voltage curves are obtained. Note the similarity of Figure 14 to the theoretical result. (8,14,15) Figure 14 was plotted using the value of $n_e - n_o = 0.262$ quoted by BDH Chemical as the starting point. The figure was plotted using the off-state as a reference. This is the same as using n_e for that particular wavelength as a reference since
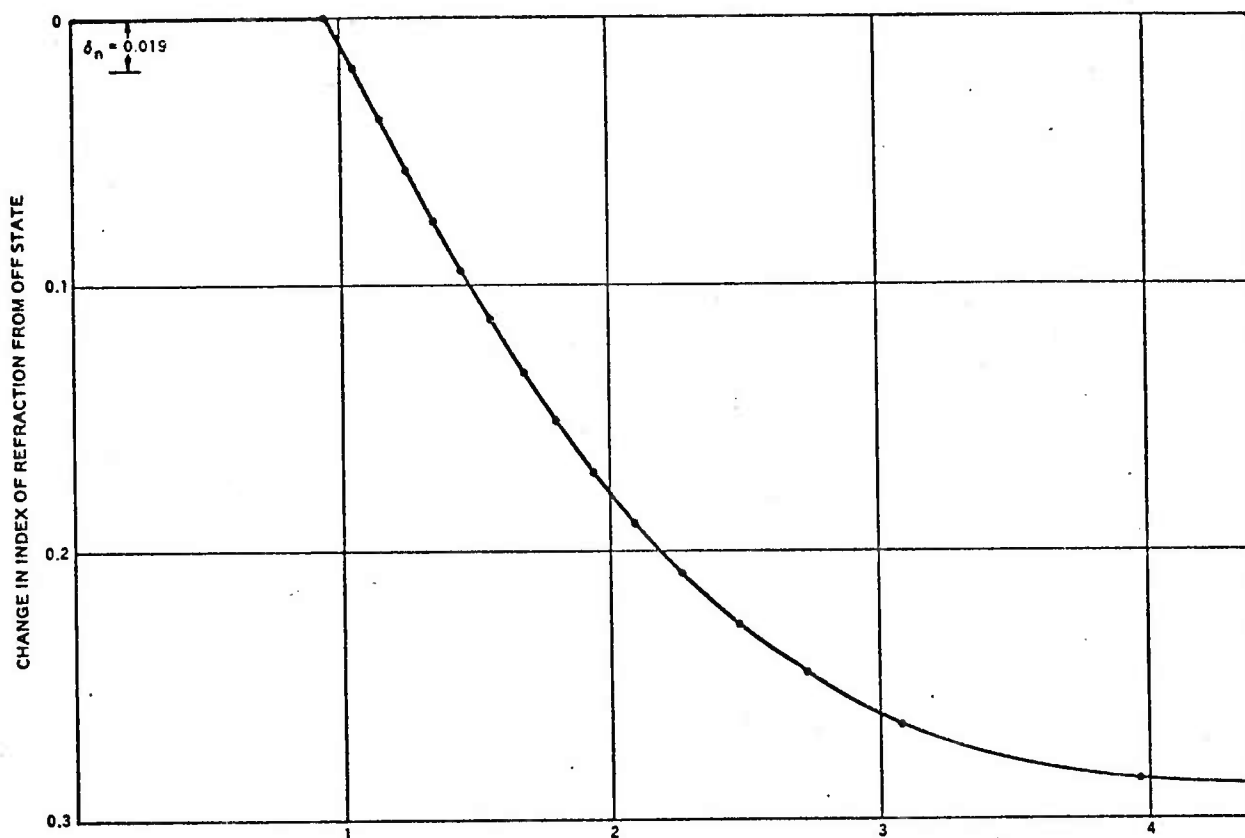
Figure 6-2. EFFECTIVE CHANGE OF INDEX OF REFRACTION VERSUS VOLTAGE
FOR $\lambda = 457.9$ nm.

E44 possesses positive dielectric anisotropy and the molecules are originally in the homogeneous state. This change in reference makes lens calculations in the next section simpler.

Note that for the case of blue light, Figure 14, the manufacturer's quoted value for $n_e - n_o$ is exceeded. Although no wavelength reference was given, it is obviously for a longer wavelength than $\lambda = 457.9$ nm.

Each of the index of refraction variation plots shows a linear relationship between index of refraction change and applied rms voltage for data points close to threshold. This fact is consistent with Kahn's results (5).

Lens Set-Up

The required index of refraction variation to create a lens was given in Equations (2-7) and (2-11)

$$n_e - n(r) = \frac{r^2}{2\Delta f} \qquad (6-6)$$

Given the desired focal length, cell thickness, and distances to the centers of the electrodes, Equation (6-6) can be used in conjunction with Figure 14 to read directly the set of required voltages.

For demonstration, two focal lengths were considered, $f = 1$ meter and $f = 5$ meters. Since the test device had thirty-six electrodes per inch, the center-to-center spacing of the electrodes was 7×10^{-4} meters. The device thickness was $\Delta = 12 \times 10^{-6}$ meters. Tables 6.1 and 6.2 give the index of refraction change and the corresponding voltage required to obtain focal lengths of 1 meter and 5 meters in green light ($\lambda = 514.5$ nm).

TABLE 6.1 REQUIRED VOLTAGES FOR 1 METER FOCAL LENGTH LENS
WITH λ = 514.5 nn

	r (cm)	$n_e - n(r)$	V (volts)
Center Electrode	0	n_e	<0.95
1st Pair	0.07	2.04×10^{-2}	1.06
2nd Pair	0.14	8.17×10^{-2}	1.4
3rd Pair	0.21	1.84×10^{-1}	2.12
4th Pair	0.28	3.27×10^{-1}	----

TABLE 6.2 REQUIRED VOLTAGES FOR 5 METER FOCAL LENGTH LENS
WITH λ = 514.5 nm

	r (cm)	$n_e - n(r)$	V (volts)
Center Electrode	0	n_e	<0.95
1st Pair	0.07	4.08×10^{-3}	.96
2nd Pair	0.14	1.63×10^{-2}	1.04
3rd Pair	0.21	3.68×10^{-2}	1.15
4th Pair	0.28	6.53×10^{-2}	1.31
5th Pair	0.35	1.02×10^{-1}	1.51
6th Pair	0.42	1.47×10^{-1}	1.81
7th Pair	0.49	2.00×10^{-1}	2.3
8th Pair	0.56	2.61×10^{-1}	4.4
9th Pair	0.63	3.31×10^{-1}	----

The size limitation of a liquid crystal lens described in Section
2 appears in Tables 6.1 and 6.2 as the electrode pair where the required
index of refraction exceeds the index of refraction variation capability
of the device (4th pair of electrodes in Table 6.1 and the 9th pair in
Table 6.2).

It is desirable to drive the center electrode as close to threshold
as possible to maximize the effective fringing to the next adjacent
pair of electrodes. This is difficult since threshold effects are
not as uniform as those observed at higher voltages. At threshold,
the liquid crystal director begins responding at the center of the
electrode. As voltage is increased this response spreads toward the
end of the electrodes. Since it does not change lens performance if
an additional constant phase delay is put into the device, a way exists
to avoid working near threshold. The center electrode is driven above
threshold with a correspondingly lower index of refraction than n_e.
This then becomes the reference and the other electrodes are based on
it. Table 6.3 and 6.4 give values when the center electrode is
driven to provide an index of refraction of $n_e - 0.05$.

TABLE 6.3   REQUIRED VOLTAGES FOR 1 METER FOCAL LENGTH LENS
WITH λ = 514.4 nm

	r (cm)	n	V (volts)
Center Electrode	0	0.05	1.22
1st Pair	0.07	0.07	1.34
2nd Pair	0.14	0.132	1.7
3rd Pair	0.21	0.234	2.97
4th Pair	0.28	0.327	----

44

TABLE 6.4   REQIURED VOLTAGES FOR 5 METER FOCAL LENGTH LENS
WITH λ = 514.5 nm

	r (cm)	n	V (volts)
Center Electrode	0	0.05	1.22
1st Pair	0.07	0.054	1.25
2nd Pair	0.14	0.066	1.32
3rd Pair	0.21	0.087	1.43
4th Pair	0.28	0.115	1.59
5th Pair	0.35	0.152	1.84
6th Pair	0.42	0.197	2.26
7th Pair	0.49	0.250	3.6
8th Pair	0.56	0.311	----

Comparing Tables 6.1 and 6.3 shows that offsetting the center electrode did not change the realizable size of the lens. However, in the 5 meter focal length case (Tables 6.2 and 6.4) the size of the lens is reduced because the eighth pair of electrodes now would have to provide a change in index of refraction greater than the cell can achieve. Although there is a loss in achievable lens size, results are much better with the offset. All of the photographs shown later are taken with the electrode voltages arranged according to Table 6.3. Individual electrode voltages were obtained by fabricating a variable resistor ladder out of sixteen 2kΩ precision variable resistors.

Experimental Arrangement

Figure 15 shows the block diagram configuration for verification of the lens effect. The argon ion laser output beam is directed through a collimating telescope, a polarizer, and finally the liquid crystal cell onto a screen. Since the polarization direction of the argon ion laser is initially at 45° to the preferential direction of the liquid crystal molecules, the polarizer in the optical chain allows selecting a component in the direction of the molecular preferential direction or a component perpendicular to it. The effect of the device on the light beam is observed on a screen.

Seven electrodes were driven with voltages given in Table 6.3. With the polarizer rotated to match the preferential direction of the molecules, a plano-convex cylindrical lens was anticipated. Rotating the polarizer 90° to be perpendicular to the molecular axis should result in a uniform pattern unaffected by the voltages being applied (Section 3). In fact, the observed pattern should look like the one obtained by having the polarizer parallel to the molecular axes but all voltages removed.

Results

With the polarizer turned to match the preferential direction of the liquid crystal molecules and seven electrodes being driven with the voltages given in Table 6.3, focusing was observed. Figure 16 shows the observed pattern.

For comparison another electrode separated from the seven was connected to the same voltage as the center electrode of the seven
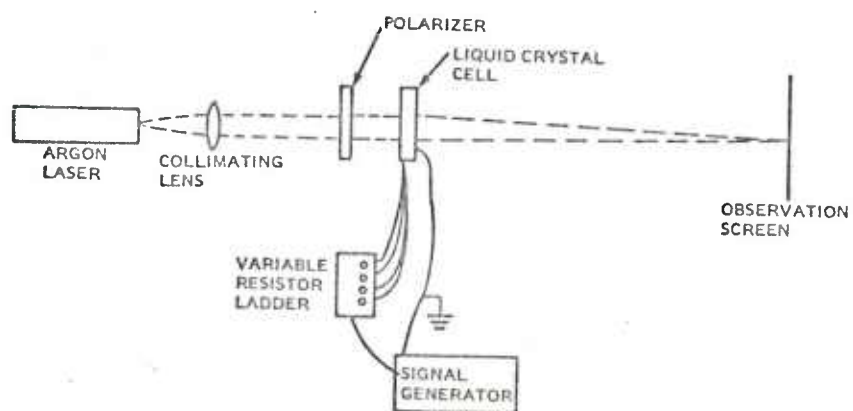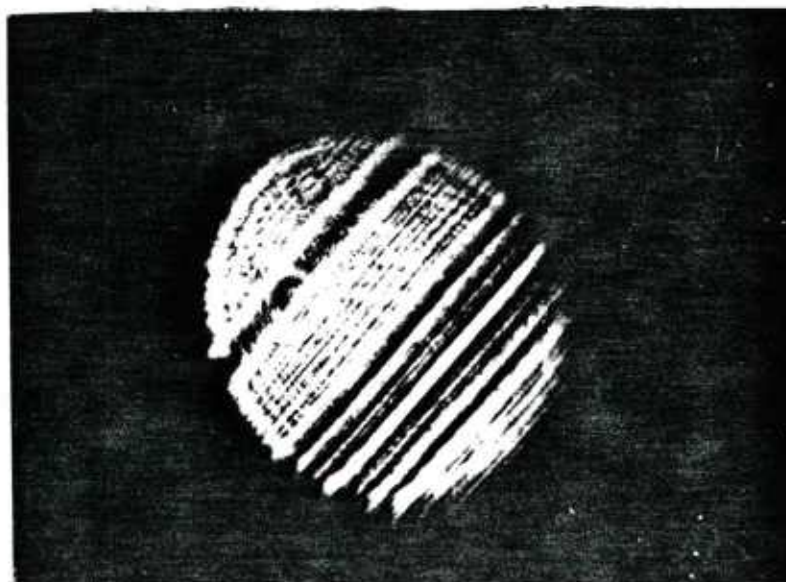
Figure 6-3. EXPERIMENTAL SETUP

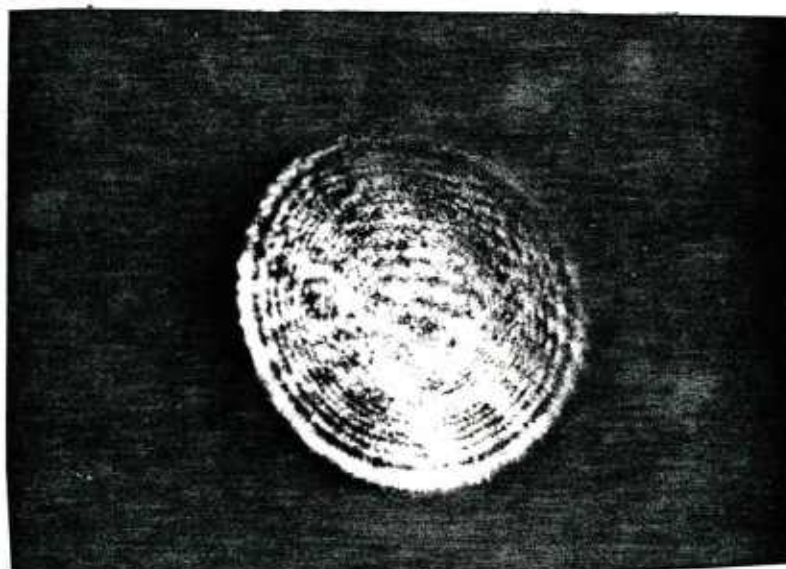Figure 6-4.   SEVEN ELECTRODE ARRAY DEMONSTRATING FOCUSING

Figure 6-5. EFFECT OF SEVEN ELEMENT ARRAY ON CROSS
POLARIZED COMPONENT.

element array. The array of electrodes is seen in the photograph on the right hand side while the dark band on the left is the reference electrode. Although the center electrode of array and the reference electrode are at the same voltage and therefore have the same liquid crystal director orientation under them, the amount of radiation observed is dramatically different. A bright line is visible at the center of the array with dark areas on either side indicating the combined effect of the array is to strongly focus the light.

Another indication of the refraction taking place is that close to the device, approximately 10 cm, the observed field is uniform. This is to be expected if the array is acting as a lens.

Without varying the applied voltages, the polarizer was rotated 90° and the photograph in Figure 17 taken. The polarizer had initially been rotated to the point where its polarization direction and the nematic director preferential direction were aligned. As indicatrix theory indicates, Figure 17 shows a uniform field when the polarization is perpendicular to the nematic director orientation. This substantiates the theory behind the four stage liquid crystal lens given in Section 4.

With the polarizer rotated back to match the nematic director, the effect of lowering all the voltages below threshold yields an observed field which is uniform.

Figure 18 shows the result of lowering the signal generator voltage until the center and reference electrodes are below threshold. The rest of the electrodes in the array still refract light although they are no longer appropriately driven for a lens. In fact, the
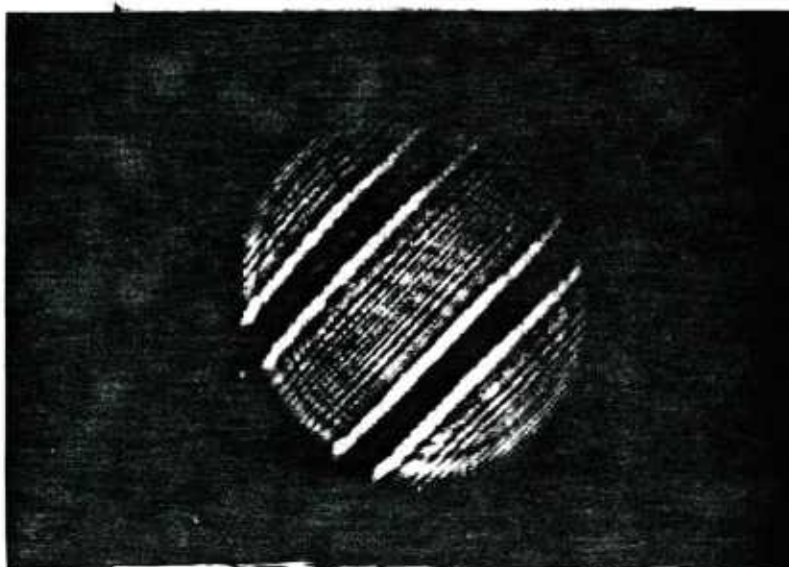
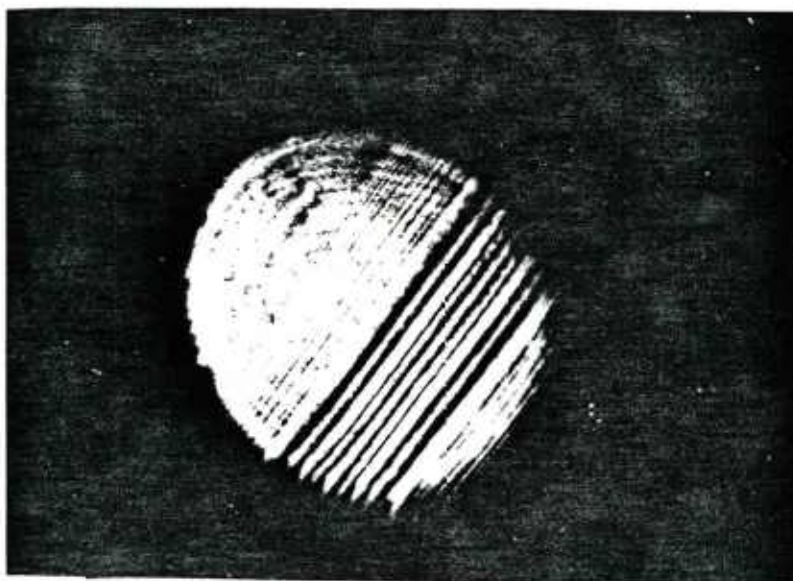Figure 6-6. SEVEN ELEMENT ARRAY AT REDUCED VOLTAGES.

Figure 6-7. FRINGING EFFECT AT SIDES OF ELECTRODES.

central electrode can be distinguished even though the reference electrode (at the same voltage) is not visible. This further verifies the refractive capability of the liquid crystal.

Note the effects of Fraunhoffer diffraction. Each of the areas beneath an activated electrode acts as a phase window causing a diffraction pattern indicative of a rectangular aperture.

Consider Figure 19 where only two separated electrodes are being driven at the same voltage. The voltage has been raised above threshold so that the electrodes have gone through a bright pattern and now appear dark. The effect of fringing can be seen as the two bright lines along the sides of the electrodes. As explained in Section 5, this extension of the reaction of the liquid crystal molecules beyond the area of the electrode is critical to the ultimate lens performance.

The empirical data shown in this section clearly demonstrates the focusing capability of a liquid crystal cell. Further, the independent nature of the cross-polarized component and the observed fringing at the edge of electrodes substantiate the concept of a four state liquid crystal lens. The data presented are quite encouraging considering how few electrodes were used, and how large a fraction of the aperture was covered by electrodes (90%). Thus the sampling of the index of refraction provides large, uniform regions, rather than smoothly varying behavior.

7. SUMMARY

A lens created from field controlled variation of the index of refraction in a liquid crystal cell has been analyzed and empirically verified. To obtain a spherical lens capable of focusing arbitrary incoming plane polarizations while maintaining a simple electrode structure requires four cascaded liquid crystal cells. With electrodes fabricated well within the microelectronics state-of-the-art near diffraction limited performance is predicted.

The focusing capability of a liquid crystal lens was demonstrated using a single crude cell with linear transparent electrodes. A plano-convex cylindrical lens for a single incoming polarization was created. Fringing along the edge of the electrodes was observed, a requirement for the near diffraction-limited performance theoretically obtainable in a structure with much higher electrode number density.

The lens evaluated had few electrodes of width ten times the fringing distance. Future experiments will evaluate the efficiency of thicker cells to obtain greater phase modulation and of higher electrode densities to obtain the smooth change of refraction needed for better optical performance.

The liquid crystal lens holds great promise. Since the ultimate phase front is electronically controlled, capability exists to compensate for system aberrations and accomplish adaptive optical techniques. Also, since the focal length is electronically controlled, the lens or a lens assembly containing the liquid crystal lens as an element

can be focused without mechanical motion. These capabilities are achievable while maintaining the inherent benefits, similar to liquid crystal displays, of low drive voltages, low power consumption, and light weight.

Modern microprocessors and digital to analog converters are small and inexpensive enough to be coupled to liquid crystal technology to produce practical adaptive lenses.

Acknowledgement

REFERENCES

1. Nye, J.F., _Physical Properties of Crystals,_ Oxford Press, London, 1972.

2. Freedericksz, V.; and Zolina, V.; Trans. Faraddy Soc., 29,919, 1933.

3. Gruller, H. and Meier, G., "Electric Field Induced Deformations in Oriented Liquid Crystals of the Nematic Type", Mol. Cryst. and Liq. C ryst. Vol. 16, p. 299 (1972).

4. Deuling, H., "Deformation of Nematic Liquid Crystals in an Electric Field", Mol. Cryst. and Liq. Cryst. Vol. 19, p. 123 (1972).

5. Kahn, Frederic J., "Electric-Field-Induced Orientational Deformation of Nematic Liquid Crystals: Tunable Birefringence", Applied Physics Letters, Vol. 20, No. 5, March 1972, pp. 199-201.

6. Schiekel, M.F. and Fahrenschon, K., "Deformation of Nematic Liquid Crystals with Vertical Orientation in Electrical Fields", Applied Physics Letters, Vol. 19, No. 10, Nov. 1971, pp. 391-393.

7. Kahn, Frederic J., Taylor, Gary N., and Schonohorn, Harold, "Surface-Produced Alignment of Liquid Crystals, " Proceedings of the IEEE, Vol. 61, No. 7, July 1973, pp. 823-828.

8. Priestley, E.B. et al, _Introduction to Liquid Crystals_, Plenum Press, New York 1974.

9. Creagh, Linda T., "Nematic Liquid Crystal Materials for Displays," Proceedings of the IEEE, Vol. 61, No. 7, July 1973, pp. 814-822.

10. deGennes, P.G. _The Physics of Liquid Crystals_, Clarendon Press, Oxford, 1974.

11. Goodman, Joseph W., _Introduction to Fourier Optics_, McGraw Hill, New York, 1968.

12. Born, Max and Wolf, Emil, _Principles of Optics_, Macmillan Co., New York, 1964.

13. Schadt, M. and Helfrich, W., "Voltage-Dependent Optical Activity of a Twisted Nematic Liquid Crystal," _Applied Physics Letters,_ Vol. 18, No. 4, Feb. 1971.

14. Kowel, S.T., and Cleverly, D.S., "A Liquid Crystal Adaptive Lens", Proceedings of the NASA Conference on Optical Information Processing for Aerospace Applications, Hampton, VA, 1981.

15. Cleverly, D.S., "Creation of a Lens by Field-Controlled Variation of the Index of Refraction in a Liquid Crystal", Ph.D. Dissertation, Syracuse University, 1982.

PART B. THE FABRICATION AND CHARACTERIZATION OF POLYMER MICROELECTRONICS DEVICES

ABSTRACT

The most significant goal of the microelectronic indus-
try is to produce smaller components which are capable of
performing complex electronic functions at an ever lower
cost. When compared to conventional electronic components,
such as silicon, the less expensive polymer materials are
becoming increasingly useful making them prime candidates
for use in microoptical devices. The primary goal of this
research was to explore the fabrication and characterization
of polymer microstructures and their application as microe-
lectronic components or optical devices.

The physical properties and deformation characteristics
of a microelectronic component, based on silicone
elastomers, were investigated in this study. For the pur-
pose of this study, the microelectronic component consisted
of a series of polymer ridges with a rectangular
cross-section metallized on both the top and the bottom sur-
faces. Typical dimensions of the microcomponent were 25 um
in width and 20 um in thickness. The microcomponent was
fabricated by crosslinking the silicone polymer via exposure
to ultraviolet radiation through an opaque mask. The defor-
mation of the devices in response to an electronic field
applied to the metal films was measured with a laser inter-
ferometer. The deformation behavior of the elastomer
depended upon the structure geometry, the tensile modulus,

the applied voltage, and the breakdown voltage of the polymer. A model, based on rubber elasticity, was developed for describing the electromechanical deformation behavior under a static electrical field. The results indicated that the optimal elastomer structure depends upon the shape factor of the structure and the modulus of the elastomer.

In addition to the deformable microstructures, contactless lithographic techniques were also studied in this research. A laser system with a microcomputer control was developed to fabricate a polymer microstructure. The geometry of the microstructure depended upon the polymer cross-linking kinetics and experimental parameters such as beam intensity, wavelength, and processing time. A polymer microstructure with a width of 2.6 um was successfully fabricated by carefully controlling these parameters.

CONTENTS

LIST OF FIGURES.

v

LIST OF TABLES.

1. INTRODUCTION

(1.0) General

Polymers, only recently recognized as potentially important transducer materials, have several advantages over more conventional ceramic materials. Ceramics are hard, stiff, brittle, heavy, and difficult to produce in large sizes or complex shapes. Elastomers, on the other hand, are soft, pliable, durable , light in weight, and easily fabricated into complex shapes. Furthermore, they are inexpensive to produce [1]. The increased usage of polymers in place of metallic and ceramic materials in microelectronic components has certainly increased. A new branch within polymer technology is the use of polymeric materials in electronic devices, such as deformable display devices, Fresnel lenses, electronically focusable mirrors, optical wave guides, and color filter arrays.

The primary goal of this research was the fabrication of polymer microstructures via conventional photolithography [2] and newly developed laser-addressing techniques. An additional aim of this study was to create adaptive optical components [3].

(1.1)   Objectives

The primary emphasis of this polymer microelectronics research was to continue improving and evaluating the deformable components. A new theoretical model of the deformation process, based on the theory of rubber elasticity, was derived and utilized in comparison with the experimental deformation characteristics of the device in an electrical field.   In addition, the research concentrated on the new laser-addressing techniques used to fabricate polymer microelectronic components.   Finally, several new concepts and applications in polymer microelectronics were explored.

(1.2) The Characterization of Polymeric Microelectronic Devices

(a) Theoretical Models of Deformation

A theoretical model, based on the rubber elasticity theory, has been formulated in order to analyze the static deflection of a polymer microstructure. The equilibrium equations were derived from an energy function composed of two parts. One contribution was the strain energy, as employed in the rubber elasticity theories. The second part was that of the electrostatic energy due to a potential across a capacitor. The model yielded expressions for the static deformation in terms of the applied potential and the modulus of the elastomer.

(b) Fabrication of Optical Polymer Microcomponents

A process was devised by Su [4] for the fabrication of an elastomer microstructure on a glass substrate through the use of semiconductor photolithographic techniques. This process consisted of the exposure of the polymer to ultraviolet radiation through an opaque mask, the development of an elastomer pattern, and the metallization of the polymer surface.

(c) Experimental Measurements of the Deformation

The deformation of the gel was measured by an interferometric technique using the red band from a He-Ne laser. The thin film electrodes yielded interference patterns from which the deformation was measured as a function of the applied voltage.

(1.3)   Laser Lithography of Silicone Elastomers

(a) Laser Addressing System

The laser system consisted of a 5 watt Spectra Physics argon ion laser, a two-step motor driven platform stage with microcomputer control, an electronically operated beam shutter, and an optical focusing apparatus. This system was capable of 1 um precision with the potential of approximately 1 um spot size. The laser could operate in the visible region (green, blue), or in the near ultraviolet region.

(b) Microcomputer-Controlled Table Motion

A system was invented which causes the stage to move in a plane, in response to commands from a microcomputer.* Two-dimensional motion was achieved by using two single axis step motors, with one motor, the y-axis drive, mounted on the platform of the x-axis drive.

----

* The software for this system was designed by Dr. J. Brule in the Department of Electrical and Computer Engineering, Syracuse University.

2. CHARACTERIZATION OF THE POLYMER MICROSTRUCTURE

(2.0) General

Using polymeric elastomer in electronic devices is an innovative new area of research. Because of the large deformation of ·the elastomer (as a result of temperature, composition, and electric field), elastomer microelectronic components, such as switching systems, electrically program-mable light deflector arrays, programmable Fresnel mirrors, and adjustable Fresnel lenses could be developed.

Essentially, the polymer electronic devices consist of large arrays of small polymeric structures having dimensions of only a few microns. As shown in Figure (2-1), each microstructure consists of a core of low-elastic constant material and two electrical contacts. Such a structure implements conventional diode matrix addressing and fabrication of the resistor array. By applying a voltage across any given resistor , a spatially varying electric field is induced, sufficient to cause a movement of the upper metal film due to deformation in the soft elastomer. The structure could be used as a display, a Fresnel mirror, etc. Of course, this structure could function as a focusing lens by adjusting the voltage in equipotential rings.

MICROELECTRONIC COMPONENT

REFLECTIVE METAL LAYER ≈ 50 nm

METAL LAYER ≈ 6 nm

(a)

COMPONENT UNDER DEFORMATION

REFLECTIVE INDIUM FILM AT POTENTIAL V

METAL FILM AT GROUND POTENTIAL

(b)
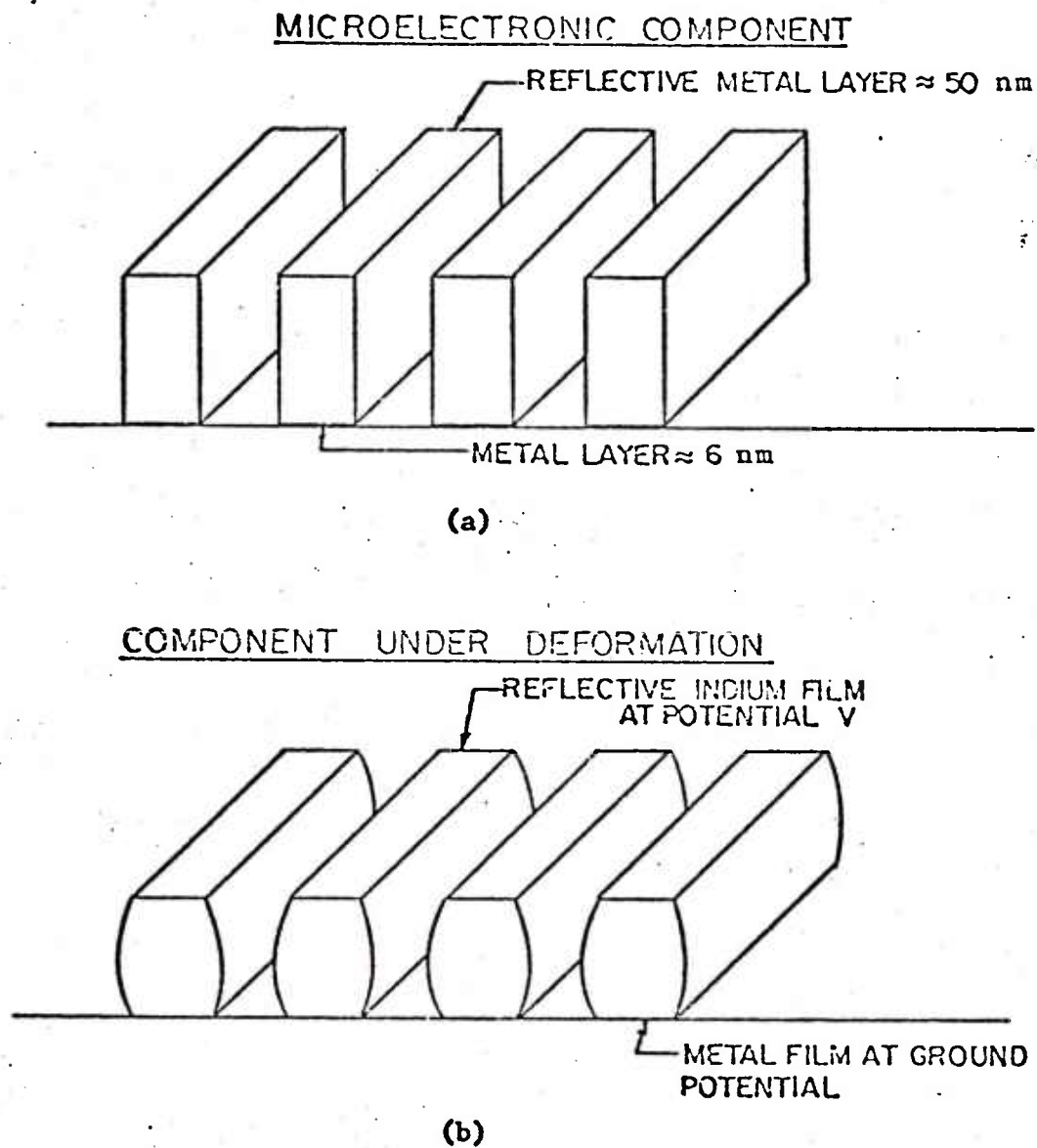
FIGURE 2-1   Typical Polymer Microstructures

The polymer microstructure was fabricated using photo-chemical lithography techniques [2, 4]. In the deformable devices, it was necessary to use very thin metal contacts so that the metal would not contribute appreciably to the stiffness of the structure [5]. For high quality reprod-uction of images, the quality of the metallized elastomer films had to be capable of displaying an undistorted phys-ical image. A new technique was developed by Martin et al.[6] to deposit the contacts on the polymer gels at 100 K.

The two specific goals discussed in this chapter are (a) to provide a description of the deformation behavior of the elastomer using a model based on the structure geometry, the tensile modulus (or the crosslinking concentration), the applied voltage, and the limiting boundaries based on the breakdown voltage of the polymer, and (b) to develop laser interference techniques in order to measure the small defor-mations of the microstructures under an electric field.

(2.1)　Deformation Model

　The elastic deformation of the elastomer and metal layer give the microelectronic device its most characteristic properties.　Several authors [7,8,9] have applied strong electric fields to dielectric polymer films to study field-induced mechanical stresses.　The deformation behavior of the elastomer was also investigated by several researchers [10-21].　A general statistical treatment of the stress-strain relations of rubbers was reviewed by Treloar [10].　Under small deformations, a good approximation of the stress-strain behavior can be obtained by employing conventional elastic analysis in which a linear relationship is assumed [19, 21].　The purpose of this section is to present a model based on rubber elasticity to describe the behavior of the structures under an electromechanical deformation.

(2.1.1) Theory

· A model, which used an electrostatic field as the external driver, was developed to describe the deformation behavior of an incompressible isotropic medium such as a silicone elastomer. The structure can be envisaged as a capacitor with a dielectric gel of silicone elastomer. The elastomer is assumed to be incompressible and isotropic. In this polymer structure, the top and bottom sides are bounded to a metal layer and the substrate. When an elastomer is loaded in compression, with the bounded faces prevented from slipping, the deformation is no longer a simple displacement. It is convenient to assume that the overall deformation consists of the superposition of two simple deformations [19,21], a pure homogeneous deformation defined by the displacement of the surface and shear displacements which restore points in the planes of the bounded surfaces to their original positions in these planes. The corresponding forces, F_1 and F_2, must be applied to the bounded surfaces and the total force F_s is given by their sum.

When a potential is applied across the structure ,as shown in Figure (2-1b), the total energy of the deformed system, E_t , consists of two terms, the electrostatic energy, E_e, and the strain energy, E_s, such that:

$$E_t = E_e + E_s \qquad (2\text{-}1)$$

For a uniaxial compression in the Z-direction (Figure (2-2)), the net force, F_z, is

$$F_z = \frac{\partial E_t}{\partial Z} = \frac{\partial E_e}{\partial Z} + \frac{\partial E_s}{\partial Z} \qquad (2\text{-}2)$$

where the potential derivatives are evaluated at constant voltage. At equilibrium, the net force is zero and the electrostatic attraction is balanced by the mechanical strain, i.e.,

$$\frac{\partial E_e}{\partial Z} = -\frac{\partial E_s}{\partial Z} \qquad (2\text{-}3)$$

or
$$F_e = -F_s \qquad (2\text{-}4)$$
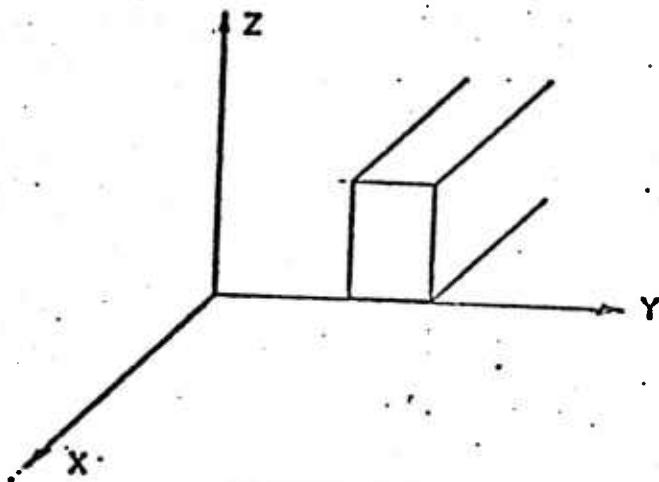
FIGURE 2-2

Coordinate System for the Deformation Microstructure

(2.1.1) Electrical Force (F_e)

For a parallel plate capacitor with dielectric materials between the plates, the capacitance is

$$C = \varepsilon \varepsilon_o A/d \qquad (2\text{-}5)$$

where ε is the dielectric constant, ε_o is the permittivity of free space ($8.85 \times 10^{-12} F/m$), A is the structure area and d is the thickness of the dielectric. The stored energy, E_e, in the capacitor at a static applied voltage, V, is

$$E_e = \frac{1}{2}CV^2 = \frac{1}{2}\frac{\varepsilon\varepsilon_o A}{d}V^2 = \frac{1}{2}\varepsilon\varepsilon_o AV^2\frac{1}{d} \qquad (2\text{-}6)$$

Therefore, F_e is

$$F_e = \frac{\partial E_e}{\partial d} = -\frac{1}{2}\varepsilon\varepsilon_o AV^2\frac{1}{d^2} \qquad (2\text{-}7)$$

(2.1.3) Linear Elastic   Force (F$_c$)

. An approximate theoretical treatment for small com-
pressions of bounded blocks has been developed [9, 21, 22].
The homogeneous compression force F is given by

$$F_1 = KEAe \qquad (2-8)$$

where E is Young's modulus of the elastomer, D is the thick-
ness of the structure prior to deformation, e is the frac-
tional compression of the block (= 1 - d/D), and K is a
numerical factor which depends upon the geometry of the
structure. For a structure in which the length exceeds five
times the width , it can be assumed that the pure homogene-
ous deformation results in zero strain in the length direc-
tion and an expansion only in the width direction. Since
the rubber is virtually incompressible in bulk, under this
consideration, a factor K=4/3 can be derived from elastici-
ty theory [23].

A second force, F$_2$, due to the outward bulging of the
initially vertical planes, arises from the requirement that
the volume of rubber is conserved. A hydrostatic pressure,
P, is set up in the interior of the rubber leading to an
additional normal force F$_2$. Relations for the pressure dis-
tribution over the cross-section of the bulk may be derived

from the assumption that the horizontal planes remain plane during the deformation. The vertical planes consequently take up curved forms as represented diagrammatically in Figure (2-3).
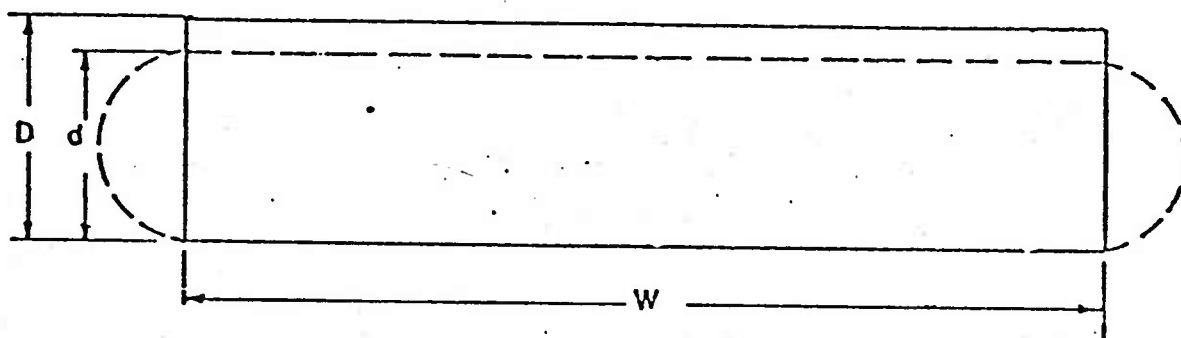
FIGURE 2-3 Cross-section of a Compressed Block

The corresponding force F_2 is given by [19]

$$F_2 = (1/3)EA(D-d)(W^2/D^3)$$

$$= (4/3)EA(1-(d/D))S^2 \qquad (2-9)$$

where W is the width of the structure, S is a shape factor (W/2D for a long strip structure [24]). More information regarding the shape factor has been presented by Long [24].

The total elastic force F_s is given by the sum of F_1 and F_2

$$F_s = F_1 + F_2$$

$$= (4/3)EA(1 + s^2)(1 - (d/D)) \qquad (2\text{-}10)$$

(2.1.4) Elastic Force (F_s).

Since linear elastic analyses do not describe the stress-strain behavior of the polymer under large deformations, a model [10, 11] which incorporated the statistical theory was derived to describe the behavior of the structure for large deformations. It is noteworthy to observe that in Treloar's experiment [11] the compression data fit the statistical theory for compressive strains up to 50%.

From the statistical theory of rubber elasticity, the strain energy per unit volume of deformed rubber which has a shear modulus G can be expressed as

$$H = \frac{1}{2} G(\lambda_x^2 + \lambda_y^2 + \lambda_z^2 - 3) \qquad (2-11)$$

where G is the shear modulus and λ_x, λ_y, and λ_z are the linear extension ratios in the X, Y, and Z directions respectively (Figure (2-2)). For an incompressible, isotropic uniaxial compression along the Z-axis, and for a structure where the length exceeds five times the width, this equation can be expressed by the conditions of

$$\lambda_x \lambda_y \lambda_z = 1$$

$$\lambda_x = 1$$

$$\lambda_y = \frac{1}{\lambda_z} = \frac{D}{d}$$

and

$$dH = f_1 d\lambda_z \qquad\qquad (2-12)$$

where f_1 is force per unit area

Thus, the force f_1 is given as

$$f_1 = \frac{\partial H}{\partial \lambda_z} = G \left(\frac{d}{D} - \left(\frac{D}{d}\right)^3\right)$$

and $\qquad\qquad\qquad\qquad\qquad\qquad (2-13)$

$$F_1 = f_1 A = GA\left(\frac{d}{D} - \left(\frac{D}{d}\right)^3\right)$$

The hydrostatic force based on the shape factor of the structure is given by

$$F_2 = F_1 S^2 = GAS^2\left(\frac{d}{D} - \left(\frac{D}{d}\right)^3\right) \qquad (2-14)$$

The total elastic force F_S can then be expressed as

$$F_s = GA(1 + S^2)\left(\frac{d}{D} - \left(\frac{D}{d}\right)^3\right) \qquad (2-15)$$

(2.1.4) Equilibrium Condition.

At a condition of equilibrium , the elastic force should be equal to the electrical force. From equations (2-7) and (2-10),

$$\frac{4}{3} EA(1 + S^2)(1 - (\frac{d}{D})) = \frac{1}{2}\epsilon\epsilon_o AV^2/d^2 \qquad (2-16)$$

From equations (2-7) and (2-15),

$$GA(1 + S^2)[(\frac{D}{d})^3 - (\frac{d}{D})] = \frac{1}{2} \epsilon\epsilon_o AV^2/d^2 \qquad (2-17)$$

(2.1.6) Results and Discussion.

The behavior of the structures under an electromechani-cal deformation, which can be described by rubber elastic theories, is shown by equations (2-16) and (2-17) and plot-ted in Figures (2-4), (2-5), (2-6), and (2-7).

The dependence of the deformation on the initial thick-ness, D, of the structure and the electric field is illus-trated in Figures (2-4) and (2-5) in which the displacement is plotted versus the applied voltage for two values of the tensile modulus. Increasing the thickness decreases the electrostatic force and results in a decrease in deformation; however, increasing the thickness diminishes the shape factor which enhances the deformation. The two effects tend to cancel each other which explains the vari-ation of the displacement with electric field shown in the figures.

When displacement versus thickness is plotted, as in Figures (2-6) and (2-7), it is found that there is an opti-mal thickness which gives the maximum deformation. Figure (2-8) indicates how the optimum thickness depends on the applied voltage and the polymer structure. From the analy-sis of the statistical theory, there is no significant change in the optimum thickness for different applied volt-ages and different modulus elastomers. The optimum thick-
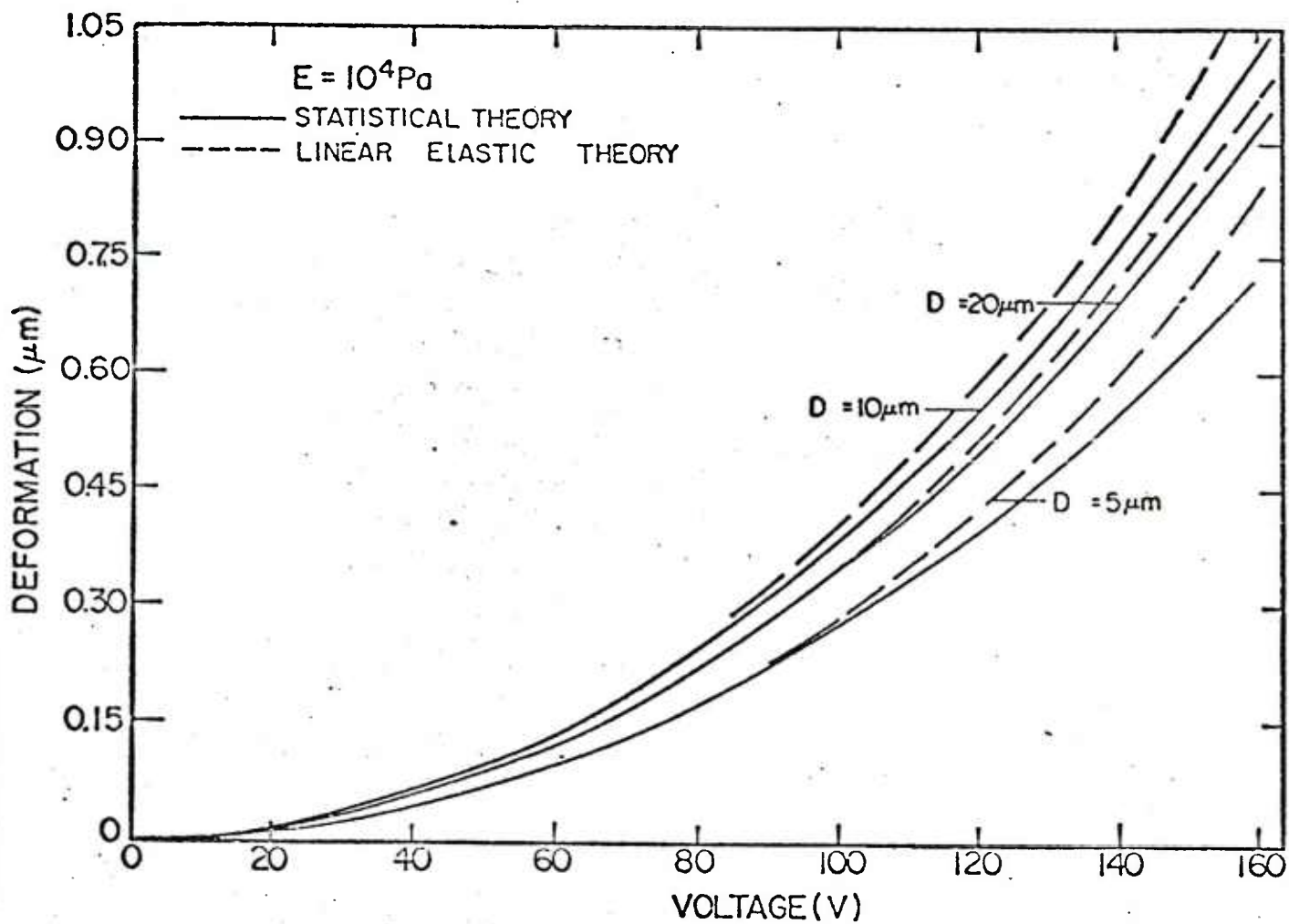
FIGURE 2-4

Component Deformation Versus Applied Voltage
(E = 10 ^{4} Pa)
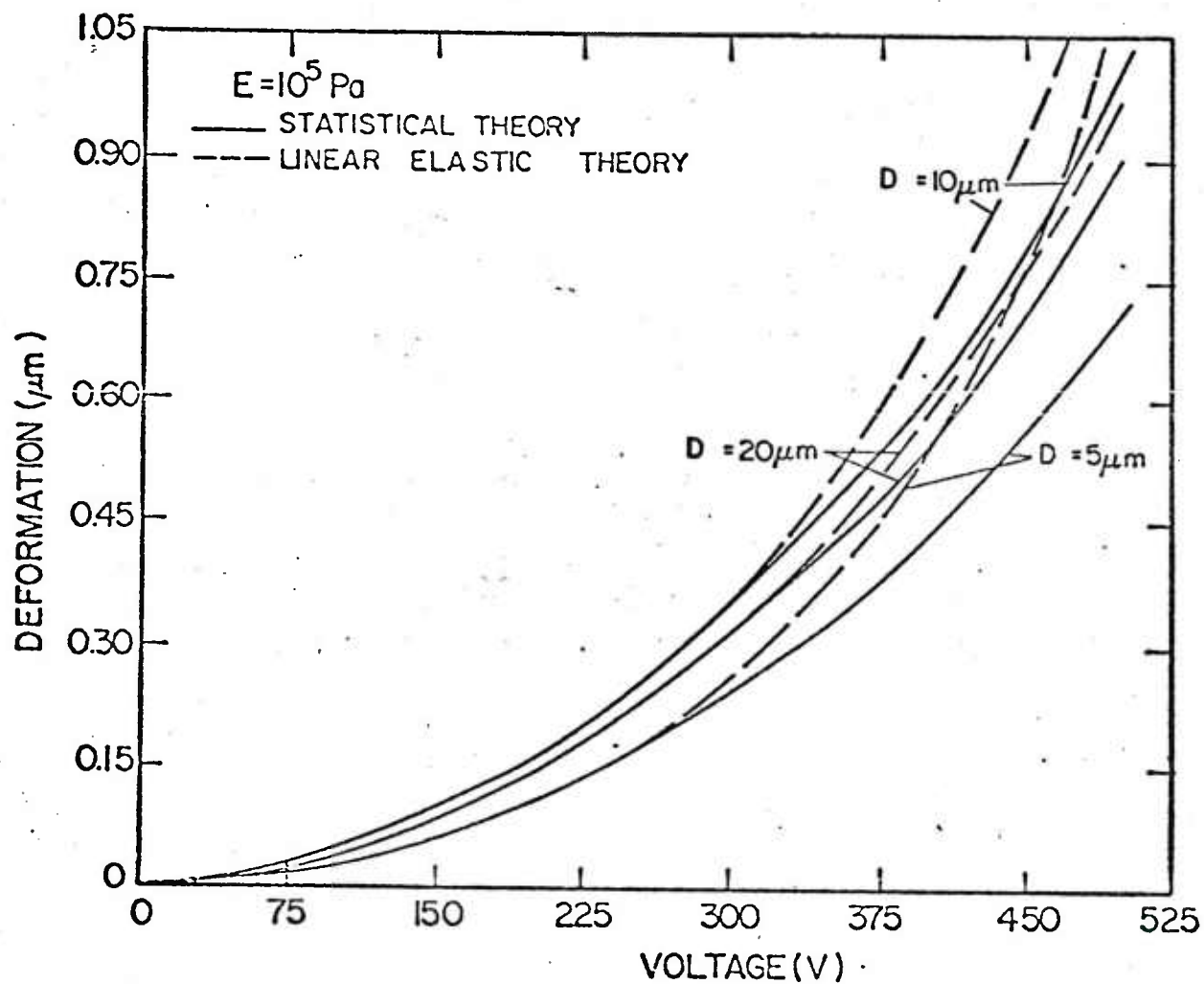
FIGURE 2-5

Component Deformation Versus Applied Voltage
($E = 10^5$ Pa)
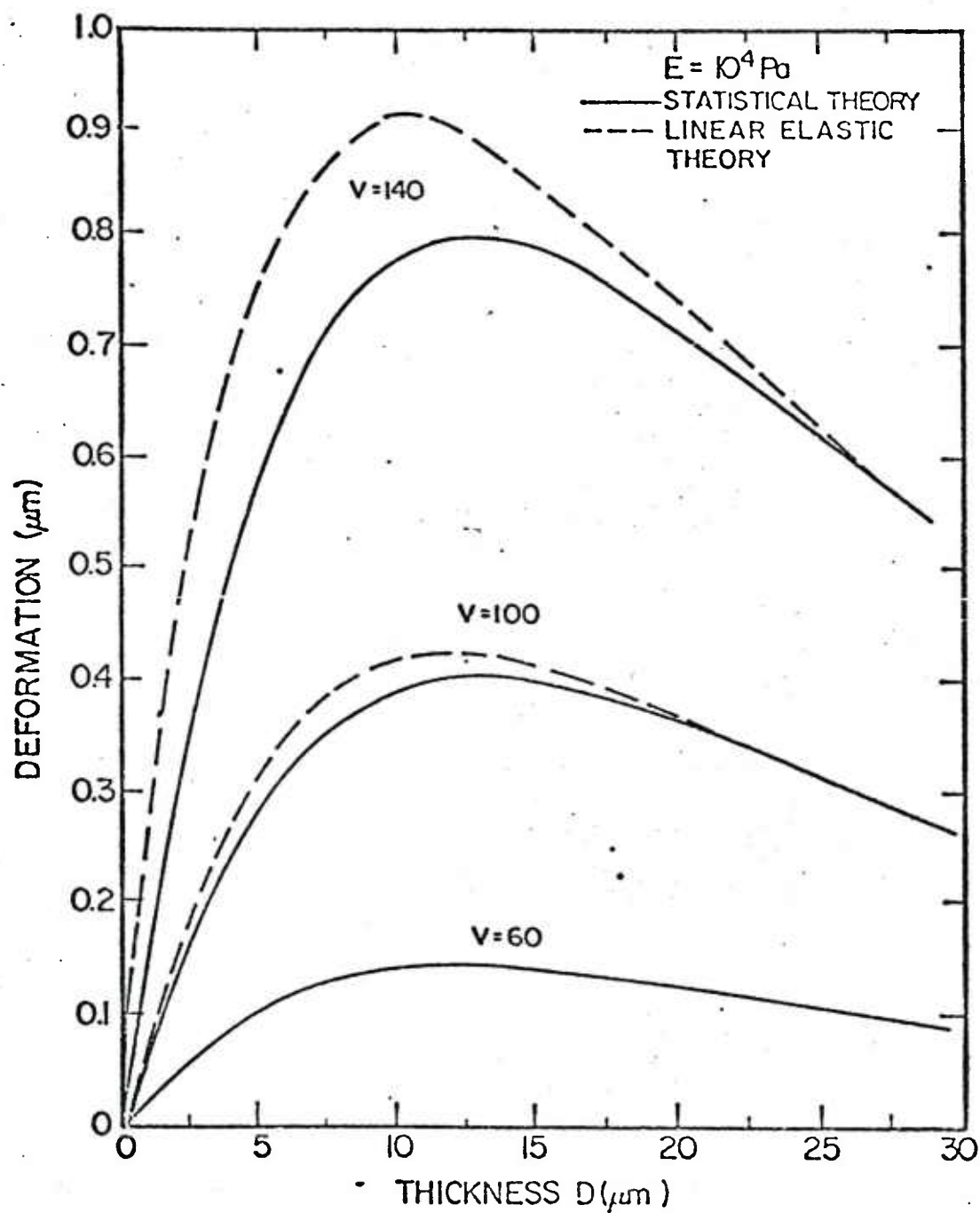
FIGURE 2-6

Component Deformation Versus Component Thickness
(E = 10^4 Pa)
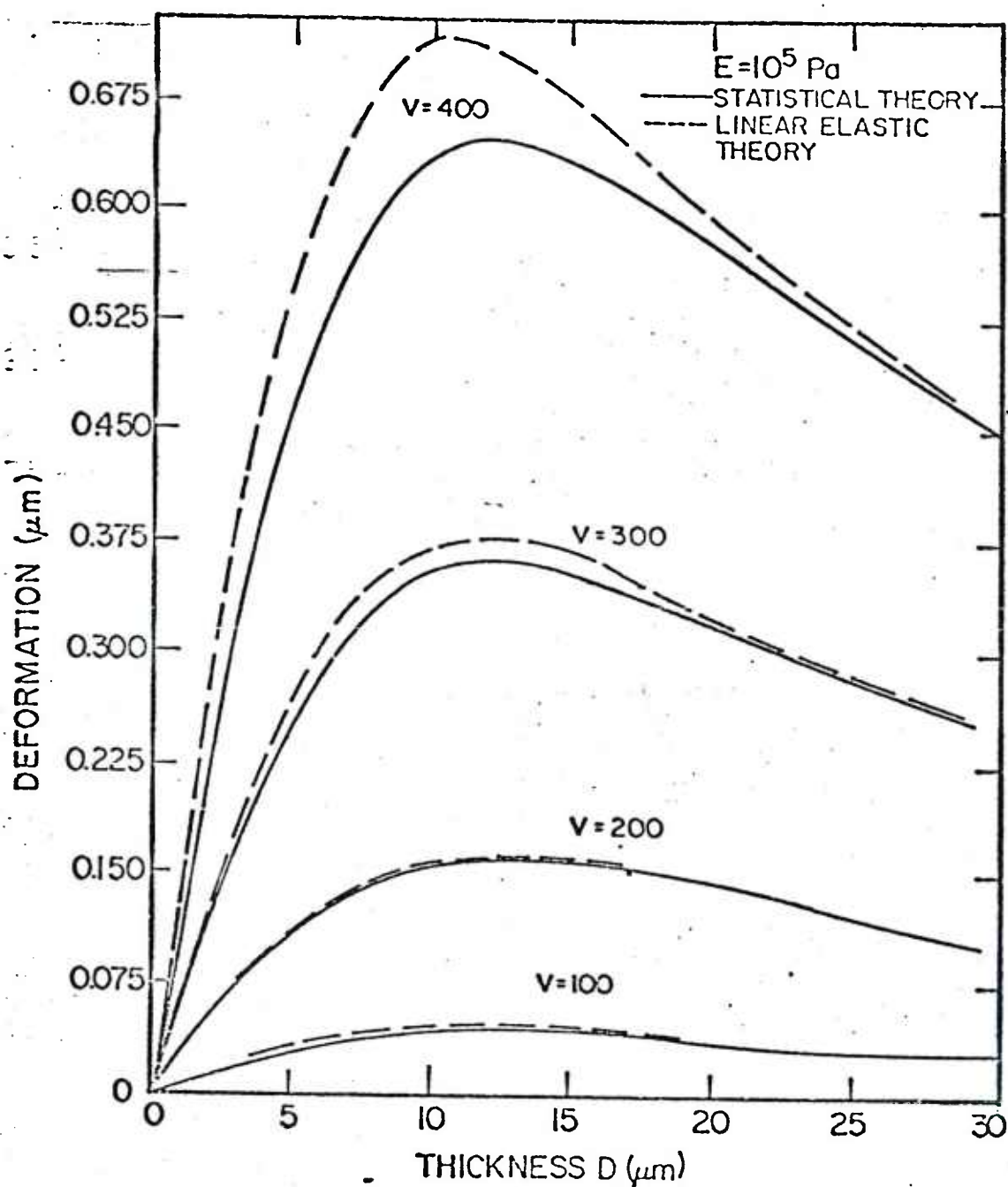
FIGURE 2-7

Component Deformation Versus Component Thickness
(E = 10⁵ Pa)
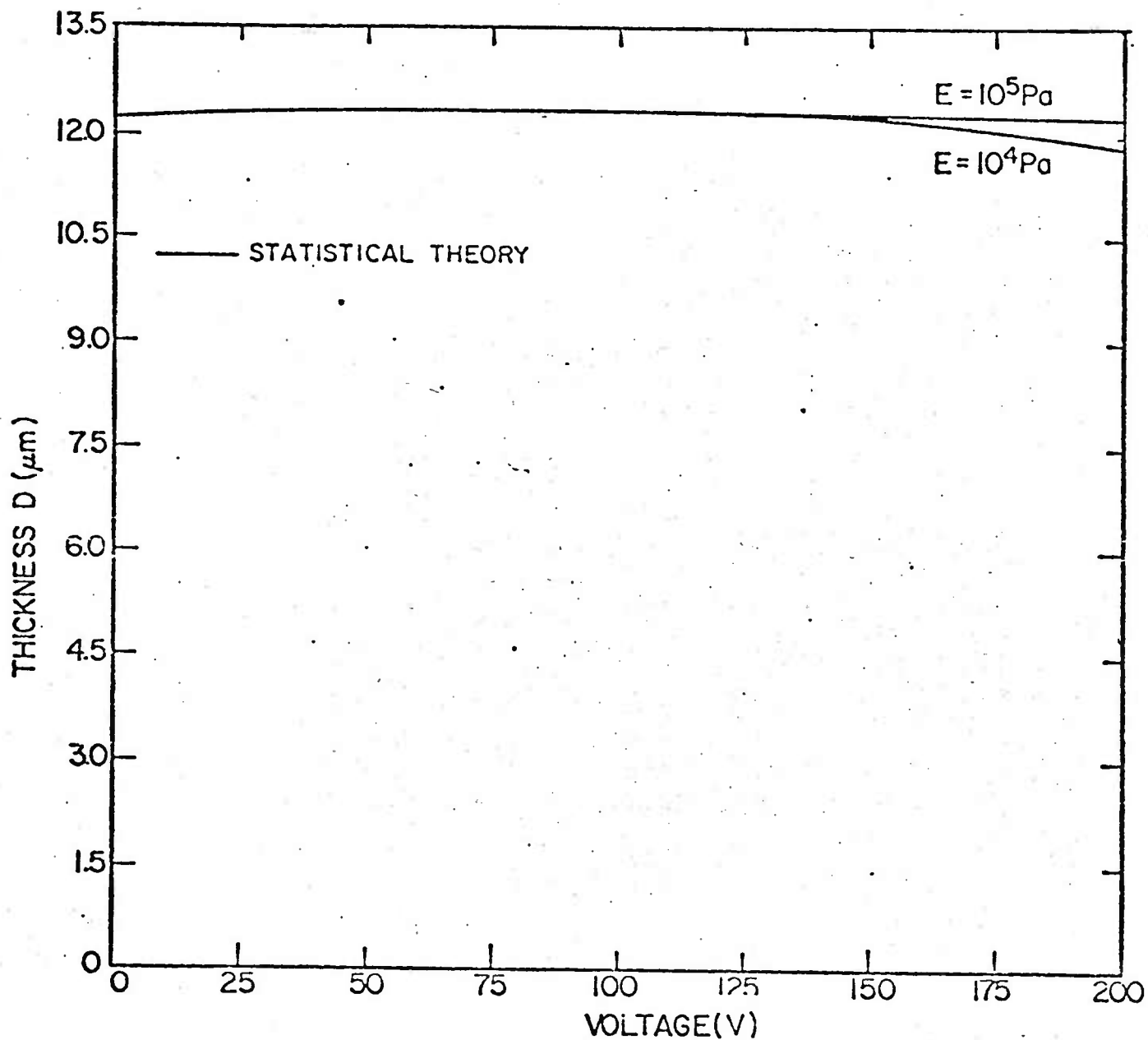
FIGURE 2-8

Component Optimal Thickness Versus Applied Voltage

ness depends only on the width of the structure and is equal to one half of the width. In other words, the optimum structure is that structure which has a shape factor equal to one.

The maximum deformation, corresponding to the optimum thickness, versus voltage for two different polymer moduli is plotted in Figure (2-9). The results show that, in order to get a large deformation, a low modulus elastomer is needed.

Gent [20] indicated that the internal cracks and voids are found to develop suddenly in bonded rubber blocks at well-defined tensile loads. To avoid internal fractures of this kind, it is necessary to restrict the mean stress applied to thin bonded blocks to less than about E/3 . The applied electrical field limit can thus be calculated by assuming that the maximum shear deformation should not exceed that of about 100 % [22]. This yields a value of 33 % for the allowable compressive strain. The corresponding maximum voltage, V_m, based on the statistical theory, is

$$V_m = 1.55 \left(\frac{G(1 + S^2)}{\varepsilon \varepsilon_o} \right)^{1/2} D \qquad (2-18)$$
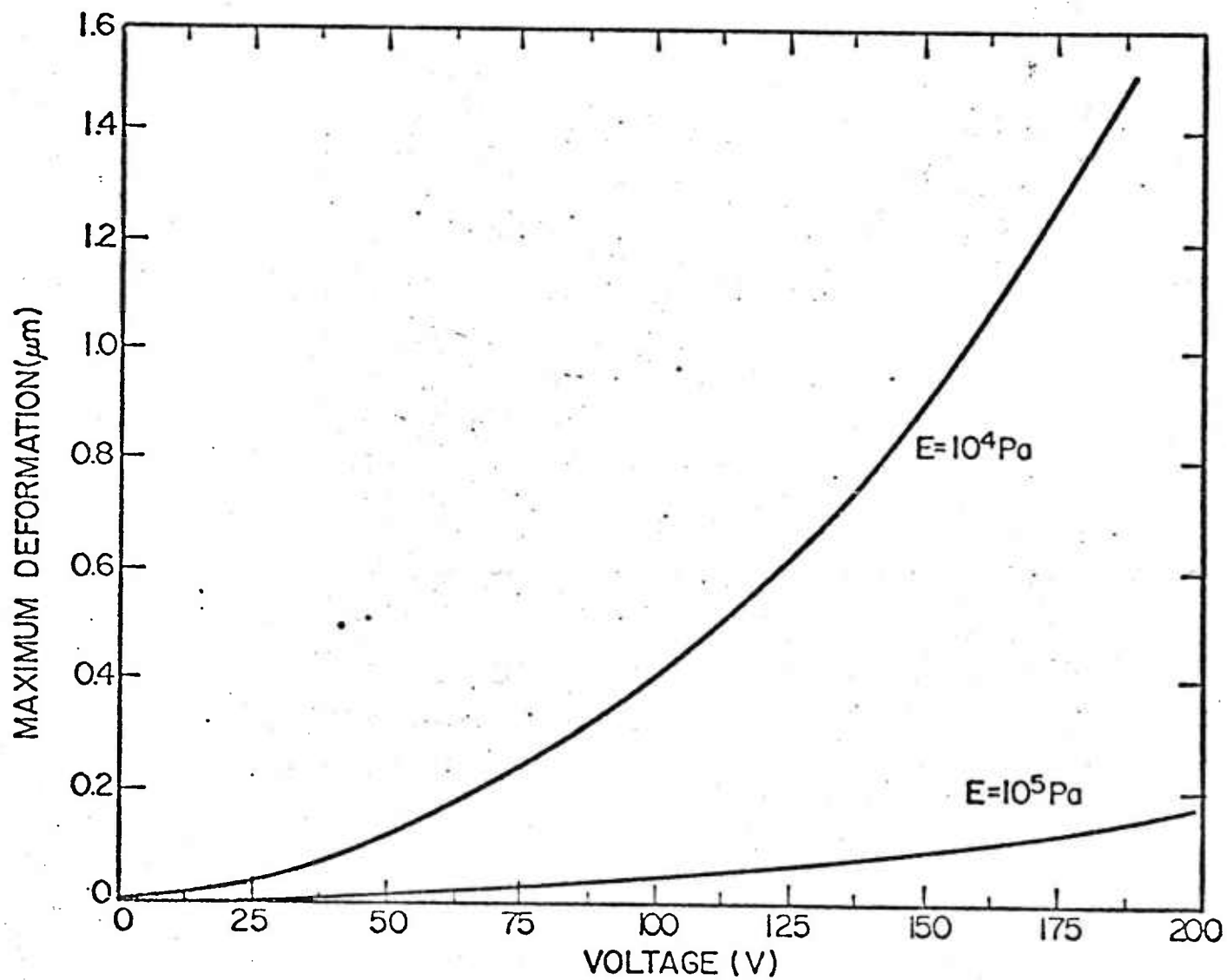
FIGURE 2-9

Component Maximum Deformation Versus Applied Voltage

Figure (2-10) shows the maximum voltage versus the thickness of the structure for different moduli. Equation(2-18) and Figure (2-10) indicate that the maximum voltage of an elastomer system having a modulus E_1 is about (E_1/E_2) times the maximum voltage of a polymer system having a modulus E_2 .

If one does not consider the shape factor, the corresponding maximum voltage changes linearly in conjunction with the thickness of the structure as shown in Figure (2-11). The maximum voltage approaches zero when the thickness of the structure approaches zero. This is impossible in a real situation. Schultz [25] indicated that hydrostatic pressure acts to increase the modulus and the yield stress. When the thickness of the structure approaches zero, the hydrostatic force, as a result of the shape factor of the structure, becomes significant.
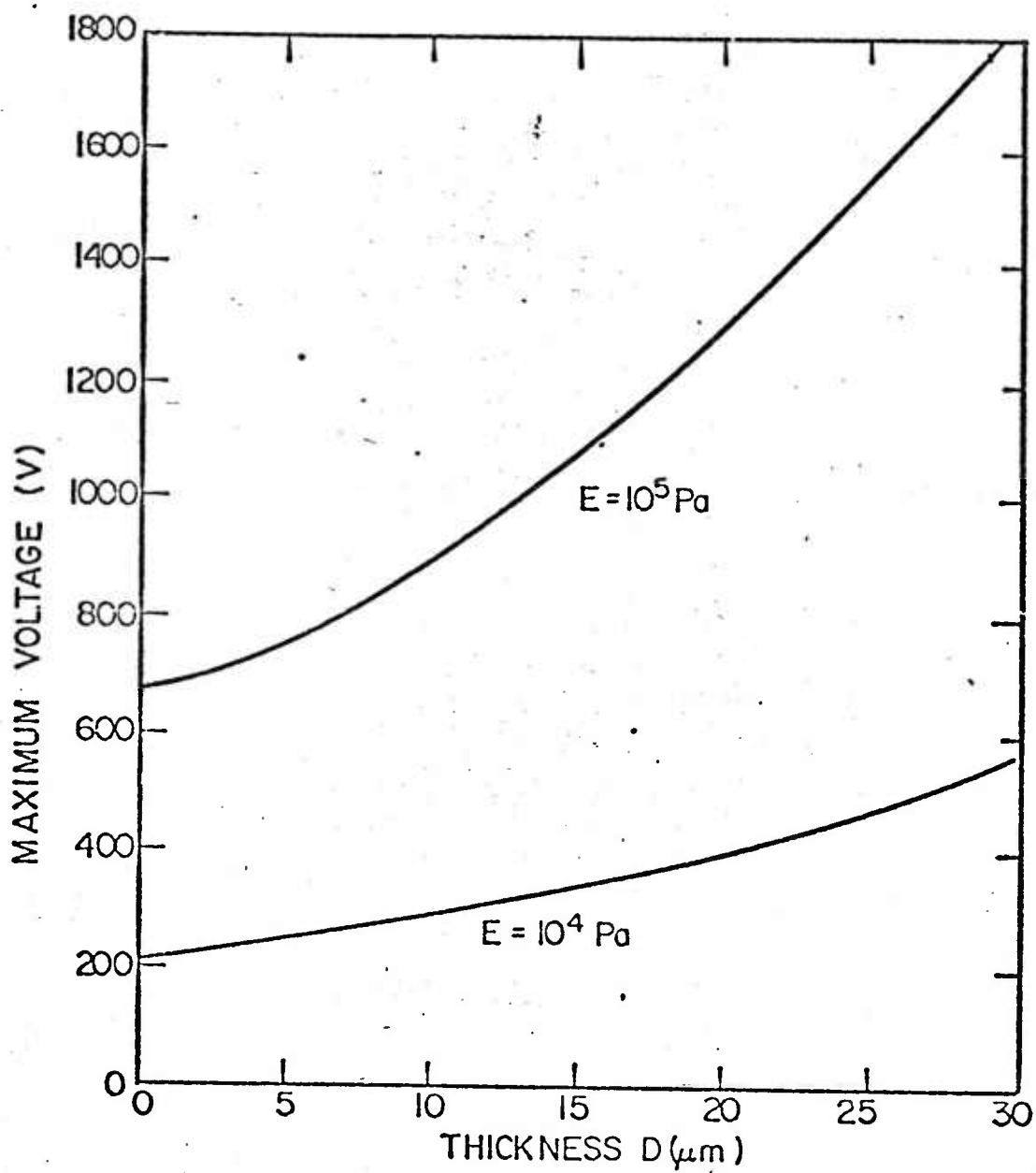
FIGURE 2-10

Maximum Voltage Versus Component Thickness
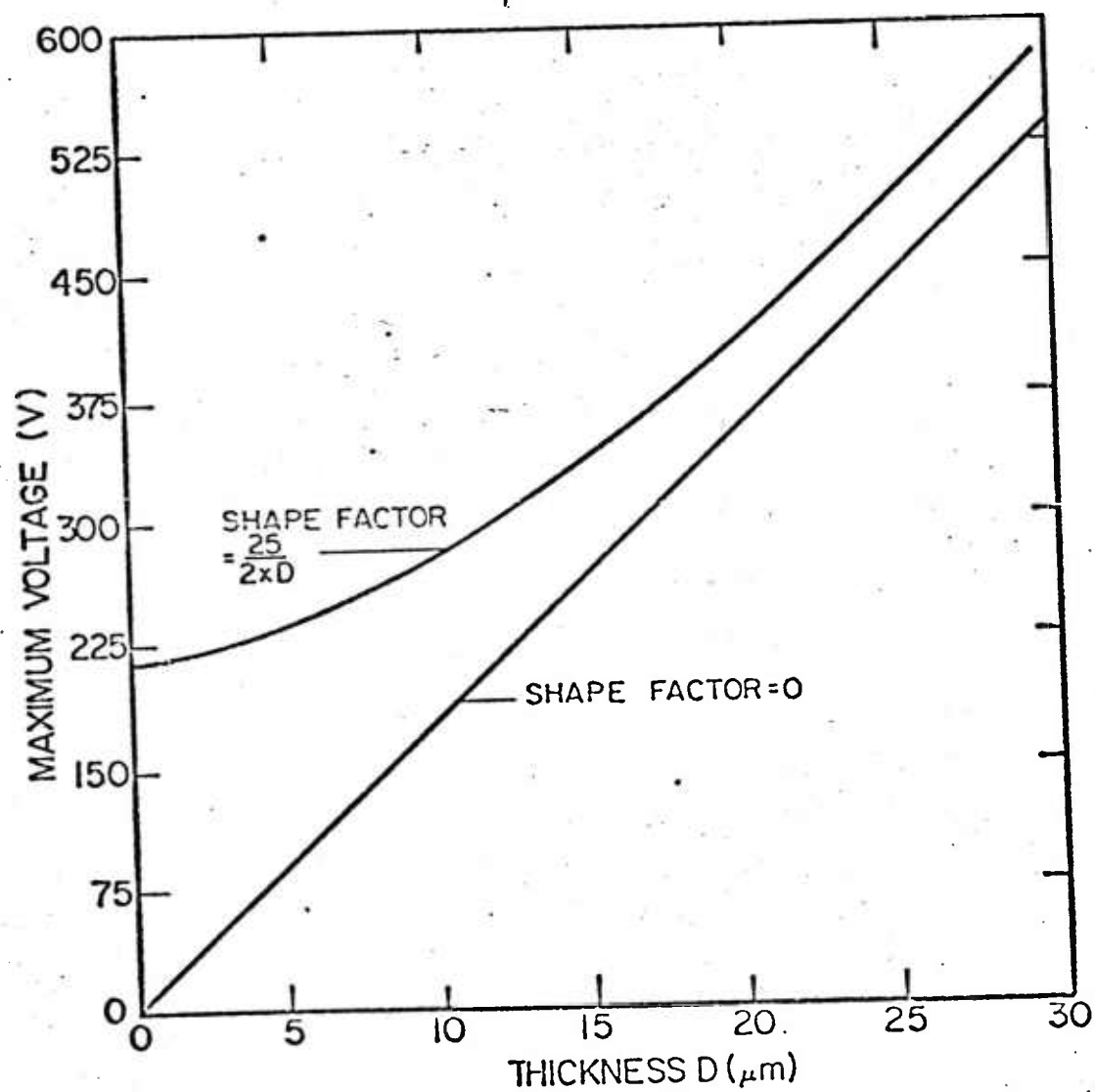
FIGURE 2-11

Maximum Voltage Versus Component Thickness

(2.1.7) Conclusion

This analysis of the electromechanical deformations in rectangular blocks of an elastomer yields a number of novel results:

1. The shape factor of the optimum structure is equal to one.

2. Deformation behavior becomes unstable when the applied voltage approaches or exceeds V_m such that

$$V \geq V_m$$

where V_m is given by

$$V_m = 1.55 \left(\frac{G(1 + S^2)}{\varepsilon \varepsilon_o} \right)^{1/2} D$$

(2.2)   Experimental

(2.2.1) Materials

Polymers are particularly useful in the deformable microelectronic devices because of their low modulus and creep and thermal stability. Silicone elastomers embrace a unique combination of these properties that permit them to satisfy the important need for softness, stability and easy deformability in the application. The most common, or widely used, silicone polymer is polydimethylsiloxane,

$$RO-\left[\begin{array}{c} CH_3 \\ | \\ Si - O \\ | \\ CH_3 \end{array} \right]_p R$$
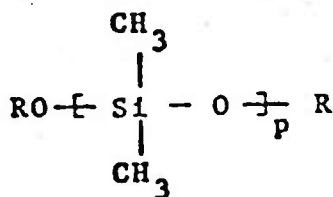
where R is a hydrogen atom, an organic group, or a triorganosilyl group [26]. The unit in the bracket is repeated many(or p) times, typically p ranges from 3000 to 5000 [27].

It is often advantageous to combine several kinds of organic groups in the same polymer to achieve specific combinations of properties. A variety of groups, including

trifluoropropyl, cyanopropyl, phenyl, and vinyl are used in subsititution for the methyl groups in order to impart specific cure, mechanical or chemical properties to silicone rubbers. The introduction of phenyl groups reduces elasticity and increases the tensile and tear strength of vulcanizates. Phenyl groups reduce the vulcanization yield. The introduction of a low percentage of vinyl groups reduces the vulcanization temperature and imparts greater elasticity and lower compression set to rubbers [26].

Crosslinking begins as a result of initiating a radical(unbonded electron) on the methyl group. This occurs when the polymer is exposed to ultraviolet radiation or reacted with peroxide by the following mechanism:

$$
\begin{array}{c}
CH_3 \\
| \\
-Si-O-]_p \\
| \\
CH_3
\end{array}
\xrightarrow[\text{peroxide}]{h\nu \text{ or}}
\begin{array}{c}
CH_3 \\
| \\
-Si-O-]_p \\
| \\
\cdot CH_2
\end{array}
+ H\cdot
$$
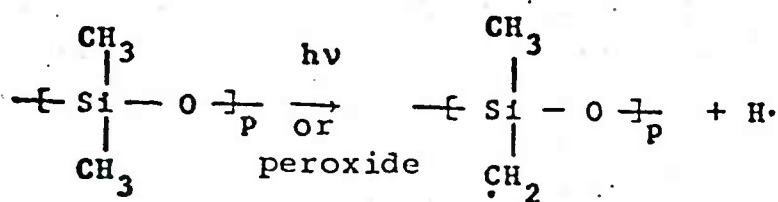
The unpaired electron of the side group carbon atom is now reactive and capable of bonding to a similar species in the following manner:

$$2 \begin{array}{c} CH_3 \\ | \\ \text{--} Si \text{--} O \text{--} \\ | \\ CH_2 \cdot \end{array} \quad \rightarrow \quad \begin{array}{c} CH_3 \\ | \\ \text{--} Si \text{--} O \text{--} \\ | \\ CH_2 \\ | \\ CH_2 \\ | \\ \text{--} Si \text{--} O \text{--} \\ | \\ CH_3 \end{array}$$
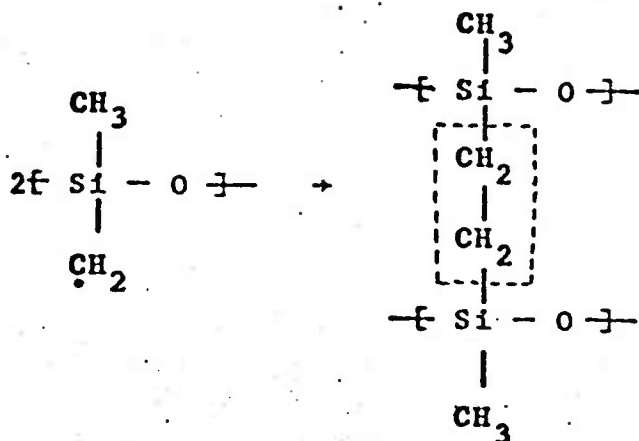
The resulting crosslink is bracketed above.

In the case of the saturated siloxanes, the crosslinking mechanism is hydrogen atom abstraction by a peroxide-derived radical, followed by polymeric radical coupling to give crosslinks. Crosslinking occurs randomly within the networks. However, fluctuations may occur due to an aggregation of the peroxide so that a nonuriform crosslinking density occurs. This problem may be circumvented by periodically substituting a diene $-CH=CH_2$ group for a methyl group in the polymer chain, as the diene group can uniformly attach itself to the silicone backbone resulting in a network with a uniform crosslink density. For vinyl crosslinking, an initiator, such as benzophenone, which is unreactive with saturated bonds and reactive only with the double-bonded vinyl groups, is used.

The polymers selected for this study were two Dow Corning ultraviolet-curable materials, denoted by the designations System A and System B, and Dow Corning Dielectric

Gel. System A consisted of a mercapto-functional siloxane (X2-7077) and a vinyl-functional fluid (X2-7078) with the crosslinking reaction between these sites. System B was a vinyl-functional siloxane (X2-7079) and a silane-functional polymer (X2-7080). The Dielectric Gel (Q3-6537) was a two-part system consisting of a vinyl-functional fluid and a silane fluid. The detailed prescriptions for the ultraviolet-curable silicone polymers are presented in Table (2-1) [28].

TABLE 2-1

Components of the Silicone Polymers

		Material Components	Mixing Ratio (by weight)
System A	X2-7077	Copolymer of $Me_3Si(Me_2SiO)_{242}$ and $(MeSiO)_{13}$ $(CH_2)_5SH$ benzophenone(3%)	97
	X2-7078	$(MeViSiO)x$ $x = 3 \sim 5$	3
System B	X2-7079	Copolymer of $(Me_2SiO)_x$ and $(MeViSiO)_y$ $x/y = 8/1$	75
	X2-7080	$(MeHSiO)_x$ and $(Me_2SiO)_y$ $x = 0.01y$	25

(2.2.2) Procedure Summary

A series of steps used to fabricate the silicone elas-
tomer microstructure was developed by Martin et al. [2] and
Su [4]. First, an opaque aluminum mask was made directly on
the glass substrate via a conventional photolithographic
technique [29]. For the deformable microstructure fabri-
cation, a very thin transparent aluminum film (~6 nm) was
evaporated over the opaque pattern as shown in Figure
(2-1a). The polymer gels were spun over the aluminum pat-
tern and then irradiated with an ultraviolet lamp through
the aluminum pattern. The exposed area was crosslinked while
the unexposed area remained uncrosslinked. The crosslinked
gel was insoluble, and thus the soluble fraction was washed
away by a solvent. In order to create a display device, a
shiny, mirror-like conducting surface was applied to the top
of the structure. The quality of the metallized elastomer
films must be capable of displaying an undistorted physical
image. A cryogenic metallization technique [6] was intro-
duced to coat the device with a very thin reflected conduct-
ing layer which would not disturb the elastic properties of
the silicone elastomer. Indium was found to have both good
reflectivity and thermomechanical properties for a low tem-
perature process (see Appendix A).

(2.2.3) Experimental Evaluation of the Deformation

An optical interference experiment was set up in order to detect displacements of the gels within a fraction of the wavelength used (HeNe laser source). A schematic of the system is illustrated in Figure (2-13). The laser beam was divided into two optical paths by the beam splitter at 7 , one path using the reflected light from 7 to shine on the sample at 4, then through 7 to the screen at 10 . The other path was transmitted through the splitter, then reflected from a mirror at 8, and combined with the first beam at 10 . The experimental set-up is shown in Figure (2-12).
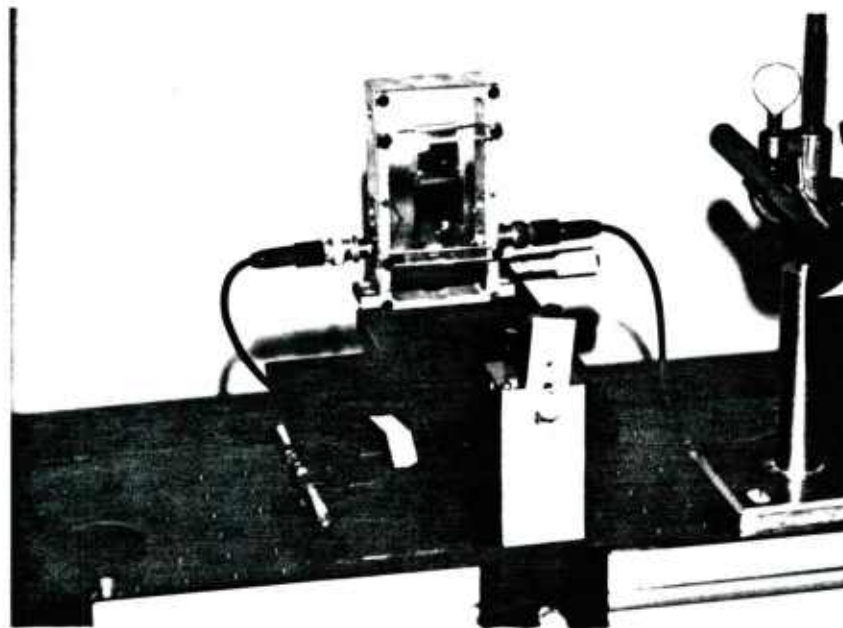
FIGURE 2-12

Deformation Measurement Apparatus
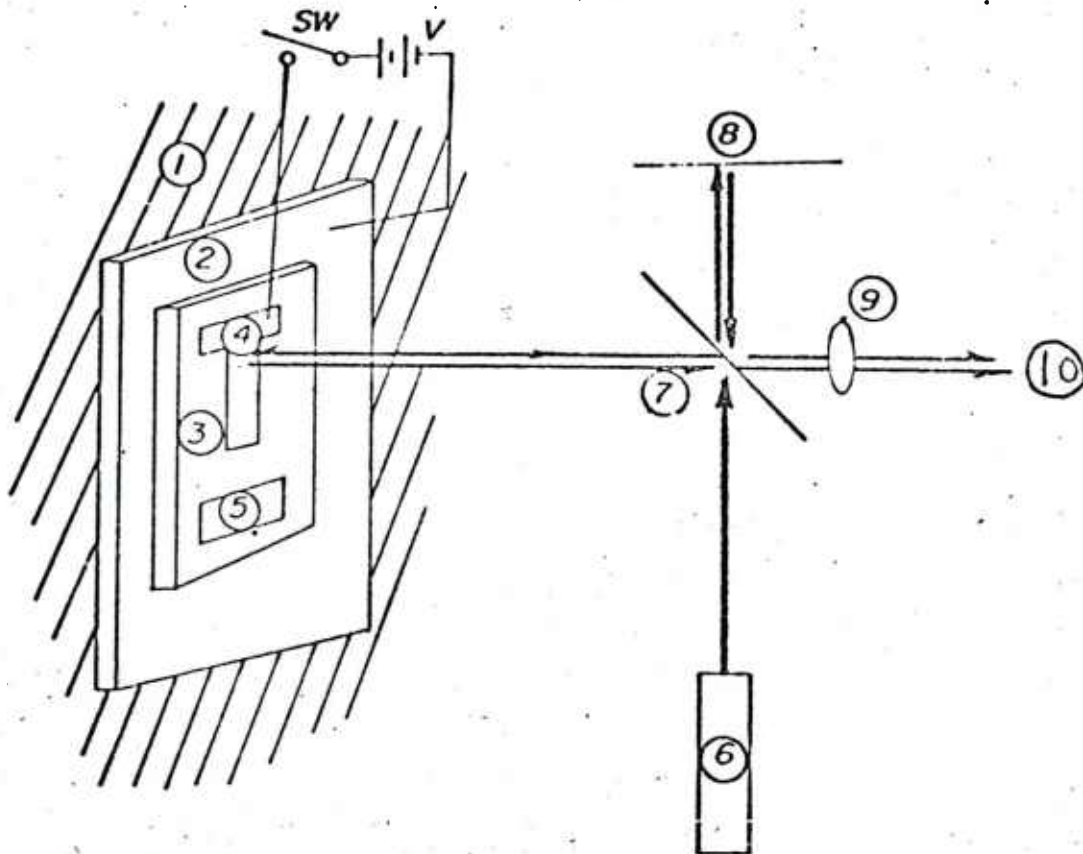
(1) Plastic   holder
(2) Glass substrate with Aluminum thick film
(3) Silicone dielectric gel
(4)/(5) Indium thin film
(6) Laser
(7) Beam splitter
(8) Mirror
(9) Beam expander
(10) Screen

FIGURE 2-13

Schematic of the Deformation Measurement Apparatus

Care was taken to eliminate vibration so that when the beams overlapped on the screen 10 , the interference fringe pattern could be observed. The deformation of the metal surface on the polymer caused the reflected beam to travel a longer distance , resulting in a shift of the interference fringe pattern on the screen.

The deformation of the silicone dielectric gel was measured as a function of voltage for L-shaped surface electrodes. These devices were made of an aluminum metallized glass slide which was coated with an 800 µm layer of dielectric gel. This was then cured at 140°C for different time periods (20, 25, 30 minutes). An indium film, 50 nm thick, was evaporated onto the gel under cryogenic conditions in the form of several L-shaped patterns. Each side of the L was 1 cm long and 0.3 cm wide, as shown in Figure (2-13). A positive potential was applied to these electrodes and the aluminum layer was grounded. A separate island of metal film , which was not connected to the electrode, was used as a reference which should not deform when a potential is applied to the L.

The deformation was evaluated using equation (2-19) [30]:

$$\Delta d = (\lambda x)/2h \qquad (2-19)$$

where Δd is the deformation, λ is the laser wavelength, x

is the displacement of the interference fringe, and h is the width between two consecutive interference fringe patterns (Interference fringes of alternating light and dark were produced by the superposition of the two light waves).

The deformation is plotted for different values of the tensile modulus in Figure (2-14). The uncertainty of the data is 80 nm by the limitation of the measurement. The deformation curves derived from the model are also plotted at different modulus values in Figure (2-14) for comparsion with the experimental curves.
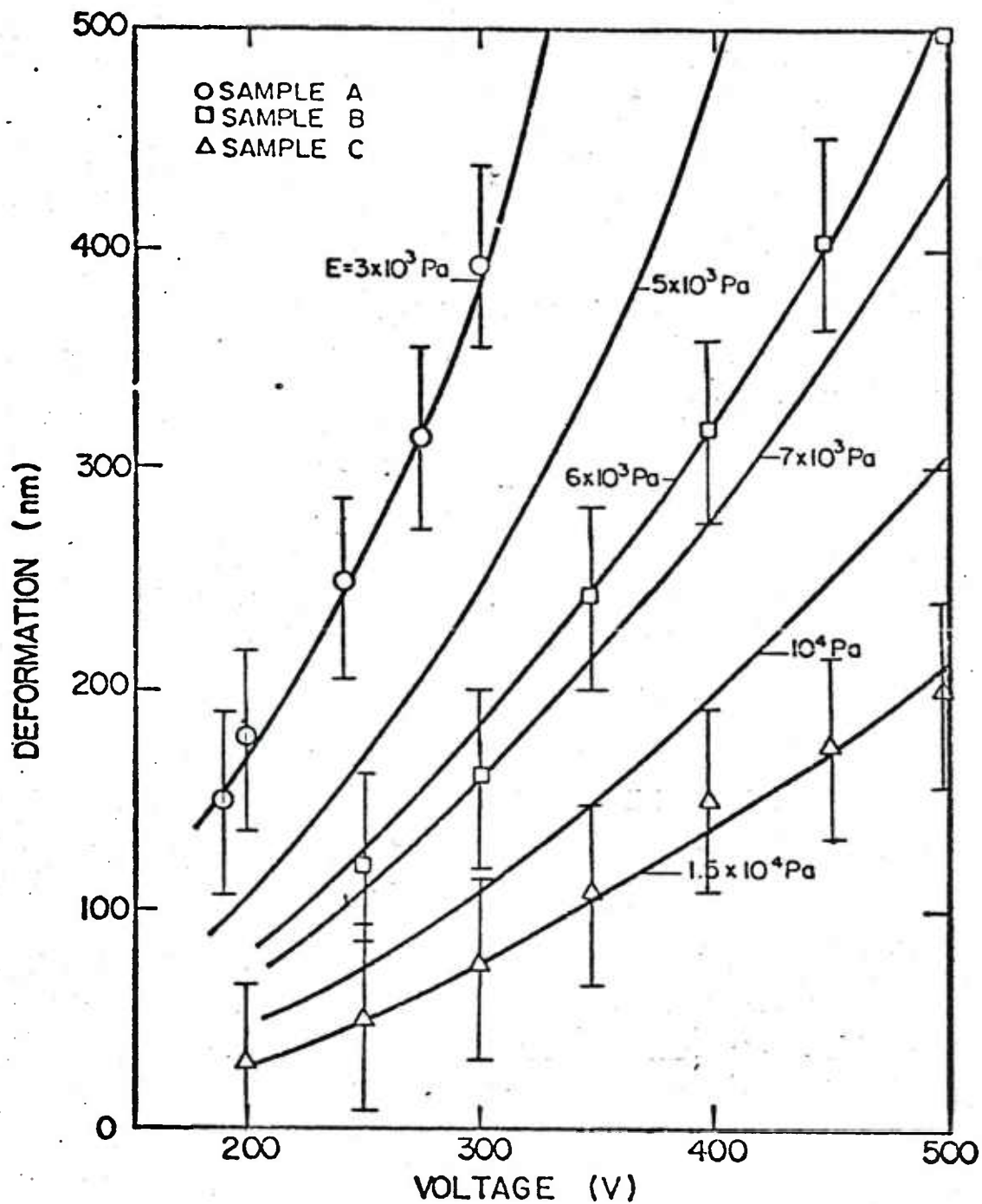
FIGURE 2-14

Experimental Plane Deformation Data are Compared to the
Equation (2-17) by Chosing Different Modulus Values into
the Equation. The material is dielectric gel with a thickness
of 800 um.

(2.3)   Discussion and Results

According to the results of Su [4], the tensile modulus of the photocrosslinkable silicone polymer has a value of the order of 10^5 Pa. This is too high for deformable device applications. According to the kinetic theory of rubber elasticity, the modulus of polymer gels depends upon the number of crosslinked chains per unit volume. A modulus of polymer gels with an order of 10^4 Pa, or even less, might be obtained by decreasing the crosslinking density. This can be achieved by decreasing the ratio of crosslinking agents, such as the number of vinyl groups in the polymer chain.

In the previous section, a theoretical model was developed for describing the behavior of the structure under an electromechanical deformation . It is difficult to verify, quantitatively, this model because of the difficulty in getting accurate values for the elastomer moduli and the effect of the metallized layer. One method of qualitatively verifying the model is to apply the voltage across the polymer microstructure, as shown in Figure (2-15), and to analyze the resulting deformation by optical interference experiments. The polymer microelectronic devices were examined in this manner and the potential V across the devices was varied up to 200 V. The voltage could not be increased beyond this range because of difficulties involved with the electrical breakdown of the polymer. These difficulties are

discussed in detail in Appendix B. The deformation of this particular type of polymer microstructure was not detectable by optical interference experiments. One explanation for this is that the top metal film on the microstructure was attached to both the glass substrate and the polymer (see Figure (2-15)) and therefore acted as a support to keep the structure in place. This restricts the full extent of deformation of the structure.
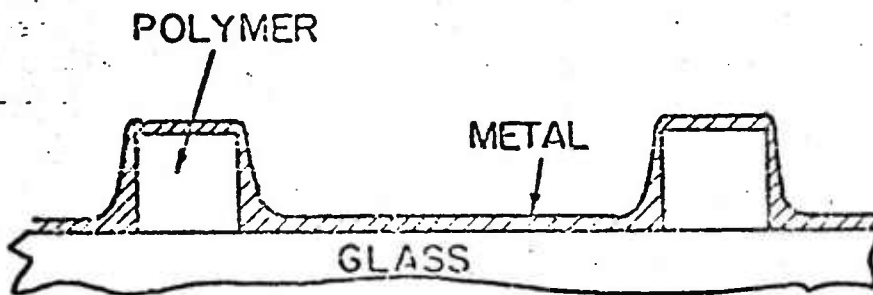
FIGURE 2-15   Metallized Polymer Structure

In order to construct and deform polymer microstructures, the compromise between softness and structure factor should be considered. That is, it is important to realize a relationship exists between how steep and sharp the sides of the structures are and how soft they are. Unfortunately, it appears that in order to obtain sufficiently straight walls so that electrode metallization can be performed without attaching to the glass substrate and the polymer, the cross-linking state of the elastomer must be such that it is

extremely hard and not easily deformed.

Because of the difficulty in deforming the microstructure as shown in Figure (2-15), the experiment concentrated on the deformation of the plane microstructure, shown in Figure (2-13). From examining the equilibrium swelling measurements, it was found that the silicone dielectric gel has a modulus with an order of 10^5 Pa. Figure (2-14) gives the deformation of the polymer pattern as a function of potential. The values of the modulus for the best fit are 3,000, 6,000 and 15,000 Pa. These data were compared to the value as measured from the swelling experiments and are shown in Table (2-2). There were experimental uncertainties involving the method of the swelling experiment resulting from the evaporation of the solvent during the measurement that may account for the discrepancy found in Table (2-2).

The deformation results show that the values of the moduli, measured from optical interference experiments, are quite close to the value predicted by the model. It can be seen that the deformation of microstructure components was dominated by three factors: the applied voltage, the moduli of the gels, and the component geometry (width and thickness). The results also indicate that elastomer microstructures are capable of plane deformation at lower applied voltages than conventional adaptive optical components which can only move 0.1 um and require higher voltages on the order of several thousand volts [5].

The restriction of the deformation measurement depends upon the choice of the light and the experimental circumstance. Any vibration in the room will produce uncertainty in the resulting data. In this experiment, the detectable displacement of the interference fringe, x, was 1/3rd of the width of the interference fringe, h. The sensitivity of the laser interferometer is 80 nm by using the red band laser (wavelength equal to 480 nm). Deformation measurements lower than this value are not reliable by interference methods.

TABLE 2-2

The Modulus of the Dielectric Gel at Different Crosslink Concentrations

Curing Time (min)	Tensile Modulus (Pa)	
	Interference Measurement	Swelling Measurement *
20	3000 ± 800	7000
25	6000 ± 1000	8000
30	15000 ± 5000	11300

* The value given is the average value for three samples

3. LASER LITHOGRAPHY OF SILICONE POLYMERS

(3.0) General

In a previous study [2,3], the fabrication and characterization of a two-dimensional array consisting of a metal layer overlaid with an elastomer microstructure and a reflective metal film was investigated. This elastomeric device was prepared using a photolithographic technique in which the radiation-crosslinkable polymer was exposed to ultraviolet light through an opaque mask. The structure was developed using a solvent to remove the uncrosslinked polymer. One limitation of this method is the requirement of a metal mask in order to transfer the desired pattern onto the substrate . Higher resolution, more complex structures, and the elimination of masking defects are obtainable using non-contact lithographic processes involving light or electron-beam writing techniques [31] In this study, the use of a microcomputer-controlled laser exposure system for the fabrication of polymer microstructures for electronic and optical application was investigated. The specific goals of the research were: (i) the development of a laser lithographic process for the preparation of polymer microstructures and the determination of the effects of experimental parameters such as beam intensity, wavelength, and

processing time on the structure geometry; (ii) the fabri-
cation and characterization of polymer structures for actual
component evaluation such as optical wave guides or display
devices; and (iii) the exploration of several polymer/laser
reaction schemes for polymer lithography.

(3.1) Characteristics of Laser Light

A laser is a device in which many electrons are "pumped" to a higher-than-normal energy state. When they fall to a lower state, they emit photons or light of a particular wavelength. The light bounces back and forth in an optical cavity formed by two mirrors, one of them partially transparent so that some light is emitted. A narrow powerful light beam results, with waves in step with each other (coherent) and close to the same frequency (monochromatic).

The main difference between laser and conventional sources consists in the spatial coherence. In contrast to arc sources which emit in 4π steradians, the laser emits a narrow beam with an angular divergence θ limited by diffraction [32,33], i.e.,

$$\theta = f_\ell \frac{\lambda}{d_\ell}$$

(3-1)

where λ is the light wavelength; d_ℓ, which is equal to 1.25 mm in the argon-ion laser system, is the output diameter through which the light radiates from the cavity; and f_ℓ is a constant factor which is equal to 1.22 for a uniform beam and $2/\pi$ for a Gaussian beam.

In the argon-ion laser system, the beam divergence is 0.69 mrad. at a light wavelength of 514.5 nm. This collimation allows a focusing of all of the emitted energy onto a small spot, the size of which is limited only by focusing

lens diffraction [34]. The optical spot size is given by

$$s = 1.27 \lambda F \qquad \text{for } 4f/(\pi d_\ell^2) << 1 \qquad (3-2)$$

where s is the minimum focused laser beam spot size (measured to $1/e^2$ points of intensity), f is the lens focal length, and $F(=f/d_\ell)$ is the F-number of the lens.

The calculated depth of focus of a focused Gaussian beam is approximately equal in magnitude to that given by the Rayleigh quarterwave criteria for uniform illumination, which is [35]

$$\Delta b = 2 \lambda n F^2 \qquad (3-3)$$

where Δb is the depth of focus, and n is the refractive index of the medium in which the beam is propagating.

Table (3-1) lists the beam characteristics for three different F number lenses with a beam diameter of 1.25 mm and shows the relationship between the spot size and the focus tolerance (or depth of focus). The spot resolution depends upon the size of the beam and decreases with the F-number; this is accomplished by a proportional reduction in the depth of the focus.

TABLE 3-1 Optical Characteristics of the Laser System

Lens Magnification	F Number	Focused Spot Size (μm)	Depth of Focus (μm)
10x	12.80	5.9	120.0
20x	6.64	3.0	32.0
47.5x	3.20	1.5	7.4

The laser is equivalent to a point source of very high brilliance. For example, an argon-ion laser emitting 60 mW single line in the ultraviolet spectrum has a brilliance of 6×10^6 watt/cm^2 compared to 10^3 watt/cm^2 for the entire spectrum of a 200 watt high pressure mercury arc lamp. This property shortens the exposure time in microlithography for pattern generation.

For conventional focused light, a physical deviation called an "aberration" arises from the fact that light of different wavelengths is focussed at different distances from the lens. These aberrations require correction. The laser, a monochromatic light source, has no aberrations.

A comparison of the beams produced by lasers and by conventional ultraviolet light sources is given in Table (3-2).

TABLE 3-2 Comparison of the Laser System with a 200 W Hg Lamp

	5W Laser	200W Hg Lamp
Wavelength (λ)	351.1 and 363.3 nm	240 - 366 nm
Focused beam diameter	4.06λ	7.78λ
Energy density	High	Low
Aberrations	None	High

In additon to its use as a writing beam, the laser also makes an interesting illuminator for image projection in lithography. The monochromatic emitted light is well suited to narrow bandwidth optics, and the high power shortens the exposure time, particularly in the ultraviolet range.

(3.2) Experimental

(3.2.1) Materials

Laser lithography should be applicable to a large number of polymeric materials involving laser-induced reactions such as crosslinking, degradation, or polymer synthesis. In this study, polymers were selected which crosslink with ultraviolet radiation, i.e., the polymers are negative photoresists. The primary system studied was an ultraviolet-curable silicone polymer consisting of a mercapto-functional siloxane and a vinyl-functional fluid [36]. The properties of Dow Corning Dielectric Gel and commercial photoresists were also investigated.

(3.2.2) Laser System

The laser system consists of a 5 Watt argon ion laser, a two-step motor-driven platform stage attached to an optical table, microcomputer control instrumentation, an electronically operated beam shutter, and optical focusing lenses. This apparatus, shown in Figure (3-1), is similar

to laser lithographic systems developed by Becher et al. [37] and by Lacombat et al. [33].

The laser can be operated in the visible (blue, green or over the near-ultraviolet range (351.1 to 263.8 nm). The beam is focused onto the stage with a microscope lens. The computer-controlled stages are capable of X, Y, or rotational motion with a speed range of 28 um/s to 2 m/s with 1 um resolution. The pattern of travel is determined by a programmed magnetic disc which issues instructions to open or close the shutter, determines the duration of exposure to the beam, selects the directions of travel, and controls the speed of stage motion. Accurate focusing is accomplished with the use of a beam splitter, an additional lens, and a fluorescing screen.

(3.2.3) Focusing Techniques

A simple focusing technique was developed by setting a beam splitter between the shutter and the microscope lens(see Fig.(3-1)). The beam passes through a beam splitter, a 50 x microscope objective lens, and focuses onto the specimen. Simultaneously, some reflected light from the specimen
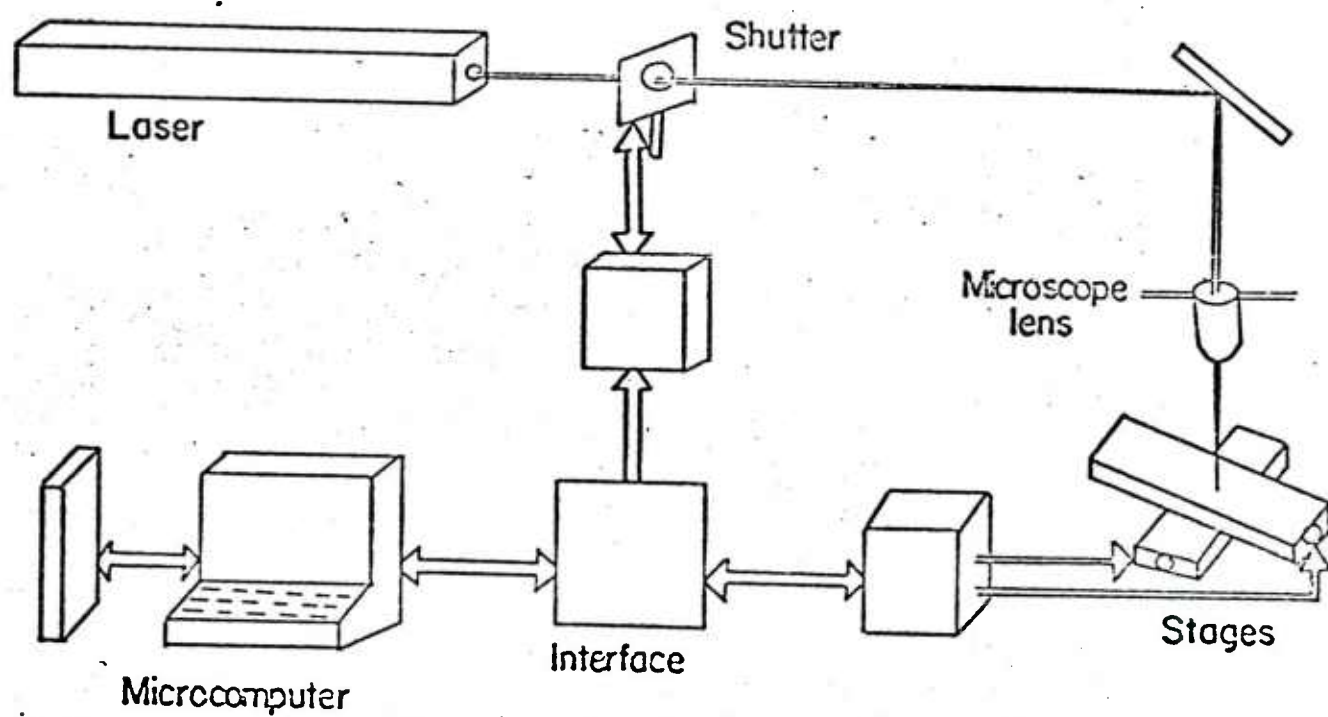
FIGURE 3-1   Laser Exposure System

returns upward through the objective lens and reflects from the beam splitter onto a viewing screen. The position of the object lens was then adjusted so that the reflected beam on the screen was focused.

(3.2.4) Microcomputer-Controlled Table Motion

In the laser addressing system, substrates are exposed to the focused laser beam while attached to a table driven by stepping motors designed to carry out programmed X-Y movement. The movement of the table is controlled by a microcomputer. Current pulses for the step motors are obtained from a translator that accepts signal pulses from an interface driver, as shown in Figure (3-1). The translator can accept manual inputs and also control pulses supplied by the microcomputer. Each pulse corresponds to a motion of 1 μm, and the speed of motion is determined by the pulse repetition frequency of the control pulses. The control pulses are obtained under software control as needed, and include another signal that opens or closes a shutter as desired. The shutter is in the beam of a laser, and thus determines whether writing is done on the material mounted on the two dimensional table.

In operation, the microcomputer generates pulses of the

proper width and frequency, as decoded from a command line input. The command lines can either be entered one at a time from the keyboard or they can be stored in a file which is stored in the floppy disk system. The motion described by the command line is displayed on the video unit of the microcomputer to give the operator a visual check on the operation of the system. The speed of motion of the table is selected under software control, and the maximum speed is limited only by the mechanical limits of the stepping motors. The mechanical characteristics of the optical exposure system are given in Table (3-3).

The physical motion of the table is governed by the command lines, but the details of the actual motion are controlled by the software. Since a mechanical system is involved, it is necessary to accelerate the table from rest to its top speed, and then decelerate it to the stop condition. This causes uneven exposure at the two ends of the routine. This error was diminished by employing the following procedure. First, when the system responds to a command to move with the shutter opened, there is a preamble motion in which the motor is stepped in the 'opposite' direction to the command direction for the distance that the motor requires to accelerate to the command velocity. This preamble motion is done at slow speed, with the shutter closed. Then, the motor is commanded to accelerate to high speed in the command direction, still with the shutter closed. When the motor has stepped back to its original position, a

TABLE 3-3   The Mechanical Characteristics of the
Optical Exposure System

X-Y table travel	100 mm x 100 mm
Linear table speed (max)	2000 µm/sec
Linear table speed (min)	28 µm/sec
Speed stability	±5%
Drive	Stepper motor operated in half step mode
Step size	1 µm
Shutter opening speed	1.1 ± 0.5 ms
Shutter minimum exposure	2.0 ms

"shutter open" command is sent to the shutter, and motion continues at the commanded high speed. When the commanded distance has been travelled, the shutter is closed, and the motor is decelerated to slow speed and then stop. Then a command is sent to step back the overshoot distance to the desired end of travel. This last postamble is done with the shutter closed. Thus, the desired motion with the shutter open is achieved at the desired speed, with no slow-speed overlap.

Figure (3-2) illustrates in detail how the plate moves when given a move command with the shutter open. The plate moves along 1-2-3-4-5-6, with the shutter opened at 3 and closed at 4.
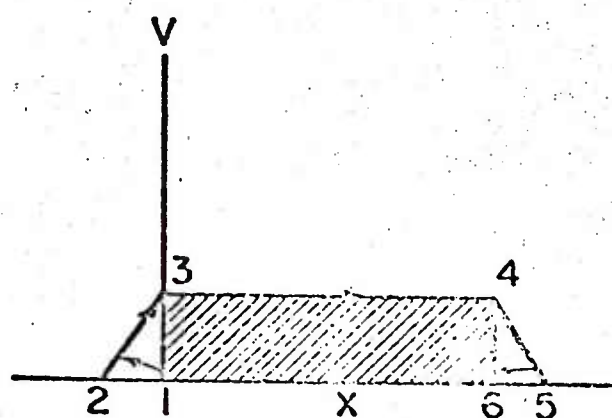
FIGURE 3-2   Velocity Profile of the Stage

(3.2.5) Exposure Routine

Figure (3-3) illustrates in detail how the routine is used to produce two orthogonal 10 um wide lines: one line from A to B and the other from B to C.
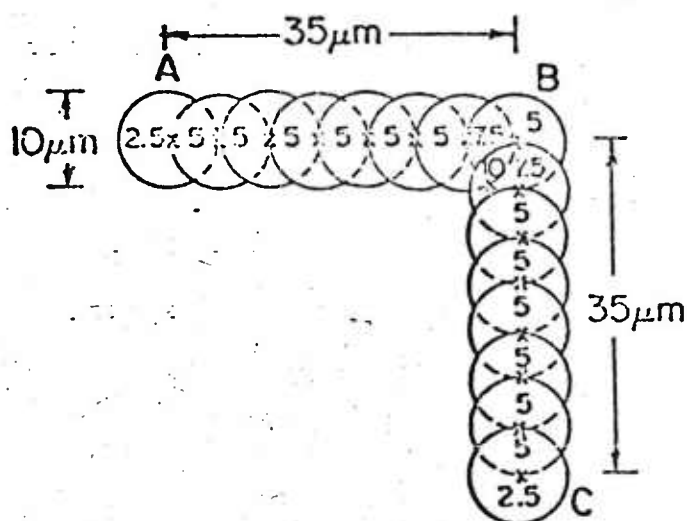
FIGURE 3-3   Exposure Routine

In Figure (3-3), the numbers shown within the incremental areas of the lines give the approximate exposure times which these areas receive for an X-Y table motion of 2 mm/s. Non-uniform exposure occurs within the incremental circles at A and B. The exposure times are from 2.5 to 5.0 ms in these areas. The line from B to C is formed in the same manner through the execution of another set of commands from the program. The area around B receives additional exposure before the table is moved to C. The incremental area around B is exposed with accumulated exposure times ranging from 5 to 10 ms. The non-uniform exposure accounts for the irreg-

ularities at the junction of the two lines.

(3.2.6) Procedure

A solution of the polymer in isooctane was spin-coated onto a glass substrate producing a coating with a thickness of approximately 5 μm. The sample was mounted on the X-Y stage and the ultraviolet beam was focused onto the sample. The computer program was then executed such that the substrate moved under the beam crosslinking only in those areas exposed to the radiation. The software was designed so that the duration of exposure was uniform throughout the sample motion. After completion of the program, the sample was removed from the stage and developed with isooctane.

Equilibrium swelling measurements, laser interferometry, and optical and scanning electron microscopy was used to characterize the resulting microstructures. Micrographs of the silicone elastomer microstructure are shown in Figures (3-4),(3-5),and (3-6).
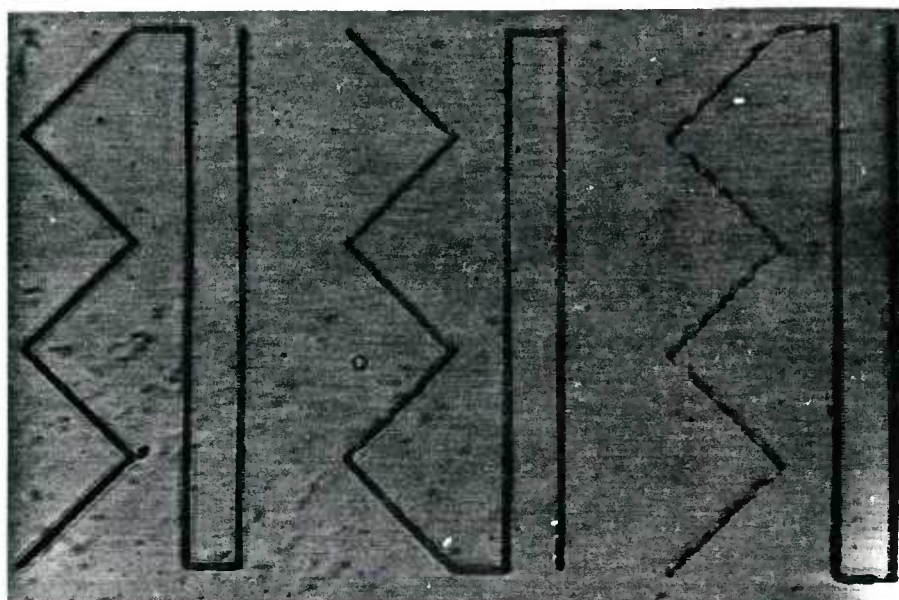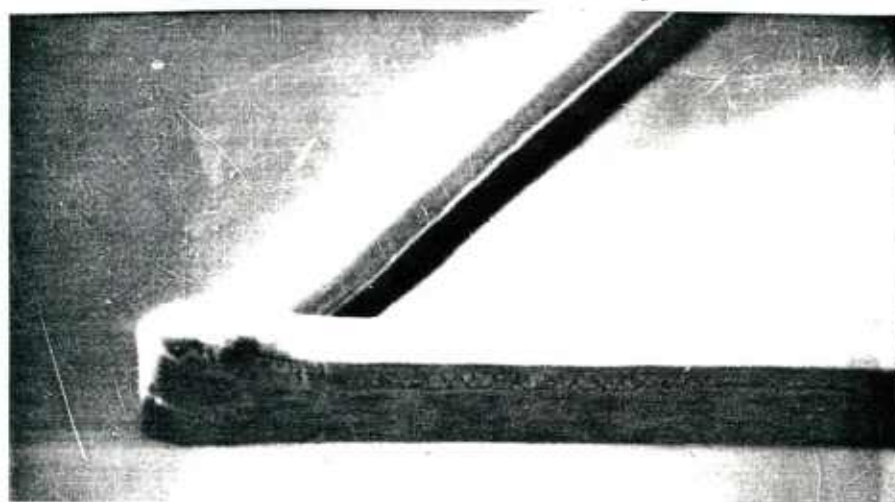
FIGURE 3-4   Polymer Microstructure.(I)

30 µm

FIGURE 3-5   Polymer Microstructure (II)
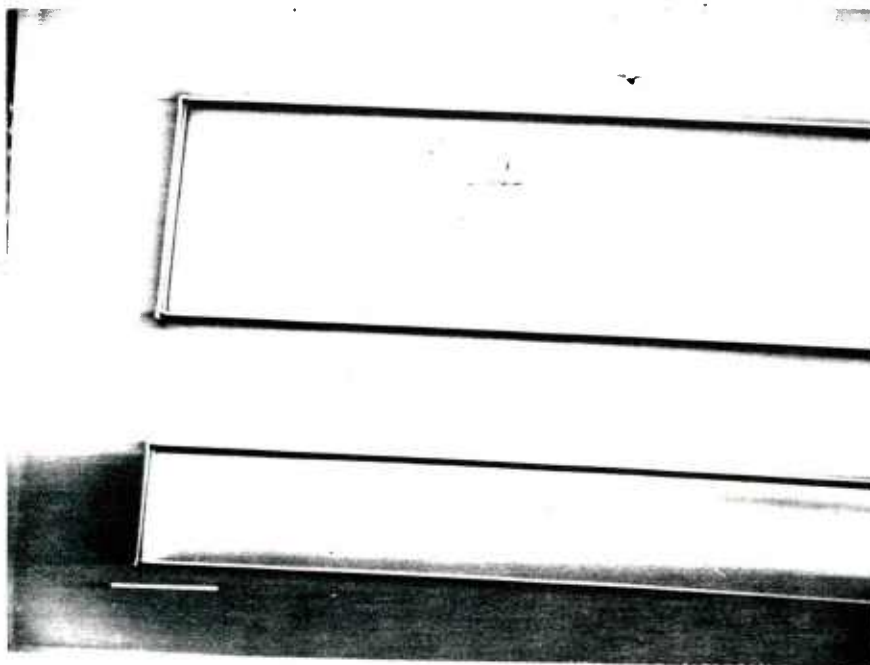
FIGURE 3-6   Polymer Microstructure (III)

(3.3)   Results and Discussion

The characteristics of the microstructure depend on the beam wavelength, the exposure energy, the writing speed, and the focused size of the beam. Microstructures were formed only for wavelengths in the near ultraviolet range and for relative exposure energies greater than 0.20. (The relative exposure energy is defined as the ratio of the beam power to full power over the ultraviolet band (~50mW).) The linewidth of the microstructure decreased with increasing writing speed and decreasing exposure energy. This result is shown in Figure (3-4), in which a typical structural pattern is shown for three exposure energies at a writing speed of 2 mm/s. and in Figures (3-7) and (3-8) in which the linewidth is plotted as a function of the writing speed and the exposure power. The minimum linewidth achieved with the laser system is on the order of 2μm for the silicone elastomers and 3μm for positive photoresists.

The irregularities, caused by overexposure of the polymer to the laser beam, at the juncture of two lines of the structure are shown in Figure (3-5). This result is similar to that reported by Brenneman et al. [31] for optical and electron beam systems. Figure (3-6) shows the uniform microstructure produced at a beam power of 50 mW and an addressing speed of 2.0 mm/s.

For the silicone polymers, the dimensions of the structure depend on the system optics, the crosslinking kinetics, and the nonuniform intensity of the laser beam. The effects of writing speed and exposure energy on the linewidth may be explained by considering the Guassion energy profile of the laser beam. For the negative photoresists, an insoluble polymer is formed only in those areas which receive sufficient energy and processing time such that the polymer reaches the gel point. Consequently, the actual microstructure may be smaller than the beamwidth. It may be possible to make submicron lines with this technique even though the beam cannot be focused to such a narrow width.

This lithographic technique may be applied to any polymer system which undergoes a reaction or a change in structure induced by the laser. Further work will concentrate on determining the minimum structure dimensions, the fabrication and characterization of electro-optical devices, and the exploration of other polymer/laser systems.
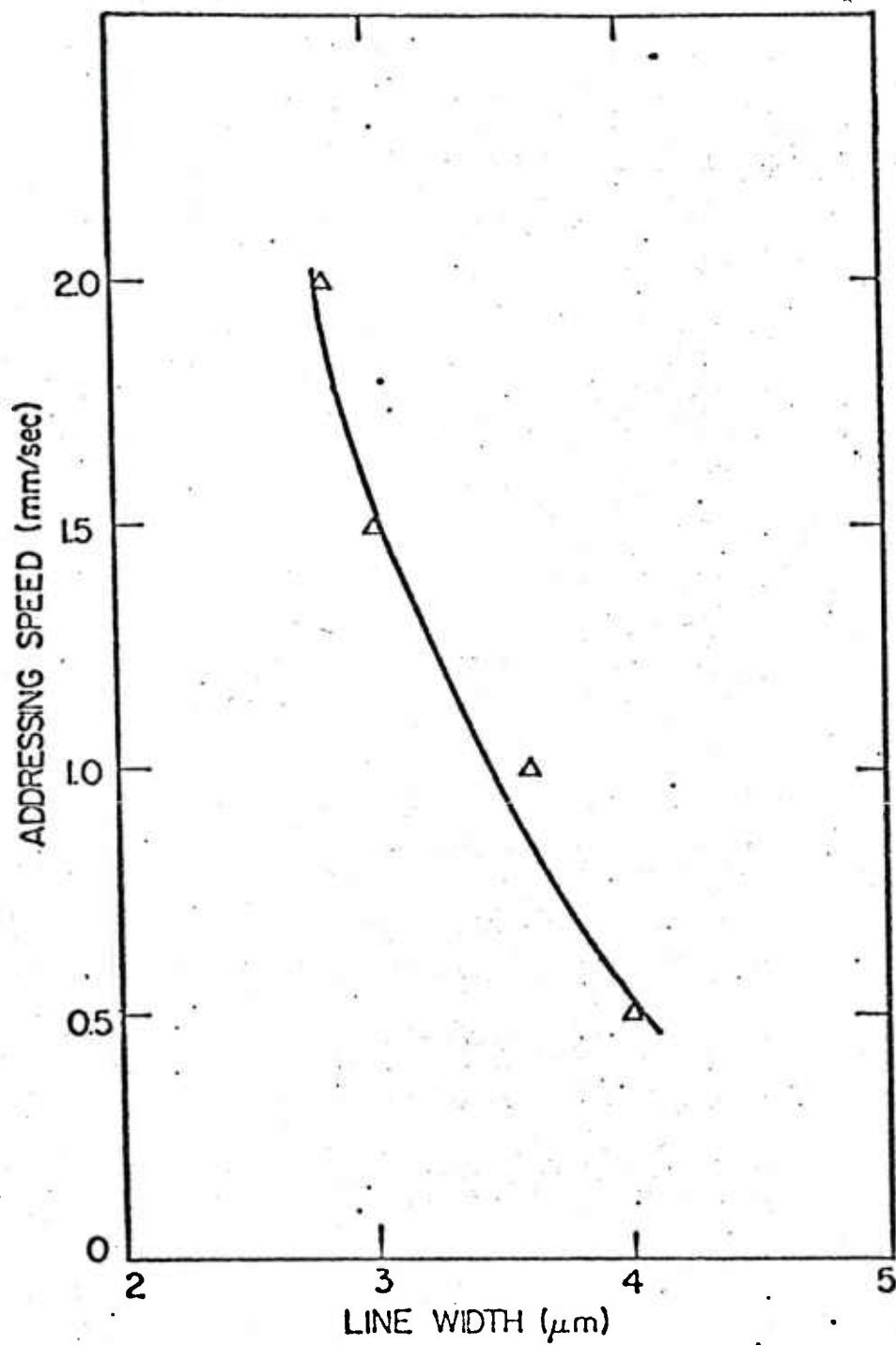
FIGURE 3-7

The Width of the Polymer Microstructure
Versus Addressing Speed
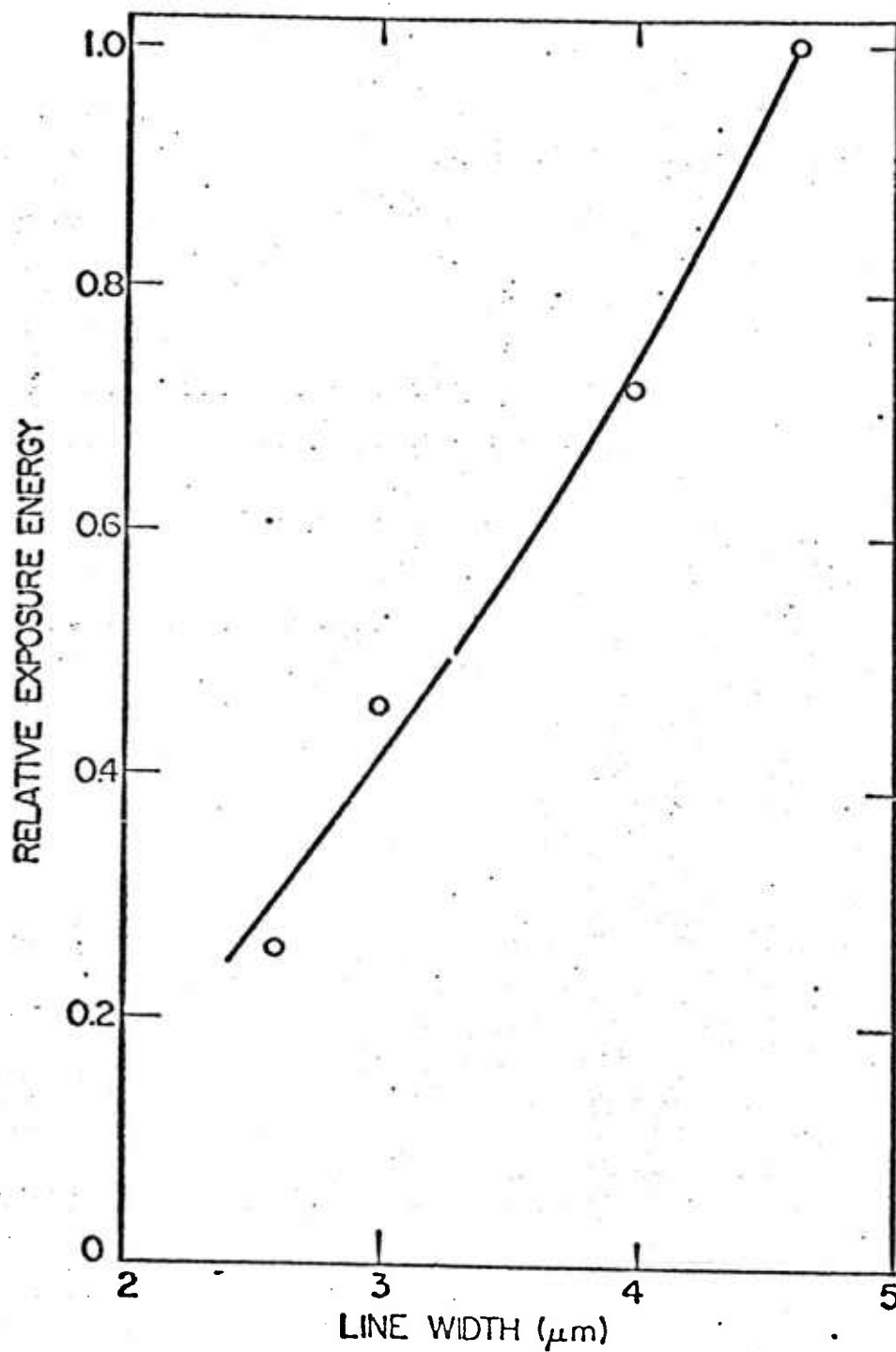
FIGURE 3-8

The Width of the Polymer Microstructure
Versus Exposure Energy

4. CONCLUSIONS AND SUGGESTIONS FOR FUTURE WORK

(4.0)   Conclusions

A new area in the application of polymers as active components in electronic and optical devices has been investigated. Three-dimensional polymer microstructures have been successfully fabricated in this research by photochemical and laser addressing lithographic techniques. Applications of such microelectronic components include electronically and electro-mechanical focusing lenses, switching systems, optical waveguides and color image devices.

A theoretical model, based on the rubber elasticity theory, has been derived to analyze the static deflection of a polymer microstructure. The analysis showed that the deformation of microstructure component was dominated by three factors: the applied voltage, the moduli of the elastomers and the component geometry (shape factor). The analysis indicated that the structure which has a shape factor equal to one will give a maximum deformation under a static field, and the deformation behavior will become unstable when the applied voltage exceeds a value, V_m, which depends on the shape factor and the material itself.

In the case of deformable mirrors, analysis indicated that elastomer microstructures should be capable of larger deformations than conventional adaptive optical components. In order to construct and deform polymer microstructures , the compromise between softness and structure factor should be considered. That is, it is important to realize that a relationship exists between how steep and sharp the sides of the structures are and how soft they are. Unfortunately, it appears that in order to obtain sufficiently straight walls so that electrode metallization can be performed without shorting the electrodes, the crosslinking state of the elastomer is such that it is extremely hard and not easily deformed.

The microfabrication techniques were expanded to a new laser addressing technique utilizing microcomputer control. A 2.6 μm width polymer microstructure was successfully fabricated. Future study will concentrate on applying this technique to develop new polymer applications in electronic devices, such as the fabrication of color image devices and the fabrication of optical waveguide devices.

(4.1) Color Imaging Devices

Photofabrication of various devices using light-sensitive polymers is well-known . Typical devices made using photofabrication techniques include cathode ray screen filter elements and light-absorbing matrices for charge-coupled imagers. A color imaging device typically comprises a radiation-sensitive surface superposed with a layer of a polymer containing an array of filter elements . One method of making color cathode-ray tube screens is described by Martin et al. [38]. The method in this patent involved using a photocrosslinkable, high-temperature-resistant polymer and a conventional micro-registration-technique. The radiation-sensitive sur-face of a CRT screen included a semiconductive wafer surface having an array of photosensors. A color filter array was placed in microregistration with the array of photosensors. As used here, the term microregistration means that the fil-ter array and the photosensor array are precisely aligned on a micro-scale. One method of this microregistration derived in the patent was to apply a photoresist to the polymer lay-er, expose the photoresist through a conventional mask and a mask aligner, and develop it so as to form window areas cor-responding to the photosensor areas. A new laser addressing system was developed to provide a simple, convenient and accurate technique, which can simplify the microregistration procedure.

An array of filter elements can be formed in the polymer by placing heat-transferring dyes into the polymer through window areas formed in a photoresist which is coated on the polymer layer. High temperature resistant polymers are prefered in this process as dyes should be transferred at a temperature below the T_g of the polymer. Increasing the T_g of the polymer widens the selection of useful dyes. Recent patents [38,39] have described this kind of high temperature resistant polymer.

A new application of the laser addressing technique is to fabricate a three-color filter on a semiconductor wafer having an array of charge-coupled photosensors according to the following procedure:

1. The surface of the semiconductor wafer is coated with a layer of polymer which is a photocrosslinkable polymer having a T_g greater than 200°C. The polymer layer is approximately 4 um in thickness (Figures (4-1),(4-2)). The polymer is then exposed under the ultraviolet radiation to form a crosslinked polymer.

2. The wafer is spin-coated with a positive photoresist. After that, the photoresist is exposed under the laser addressing system by computer control. (Figure (4-3))

3. The wafer is then developed in an organic solvent to remove the uncrosslinked photoresist, producing the

window areas (Figure (4-4)). The dye can be diffused into these areas.

4. The red dye is transferred into the polymer through the window so as to form filter elements in microregistration with the photosensors. (Figure (4-5))

5. Step (2),(3) and (4) are repeated using a blue dye (Figure (4-6))

6. Step (2),(3), and. (4) are repeated with a green dye. (Figure (4-7))

The result should be a color filter array superposed in microregistraton with the charge-coupled photosensor of the underlying semiconductive wafer.

Figure 4

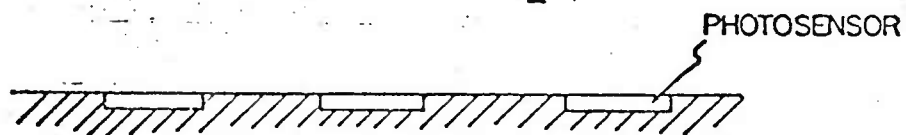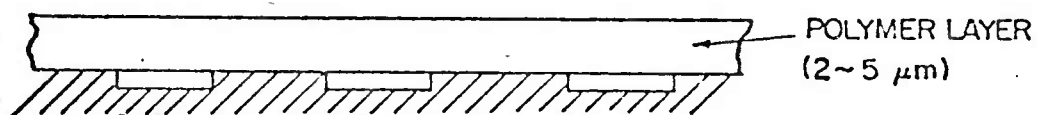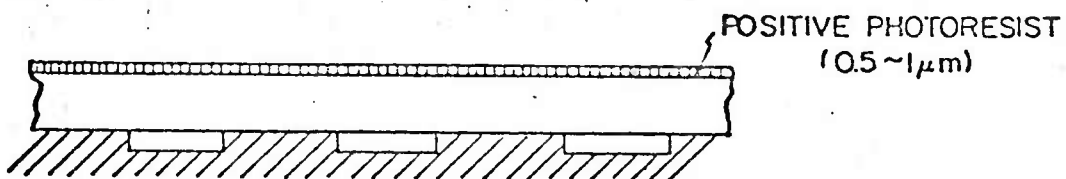### Fabrication Procedures for the Color Imaging Devices

PHOTOSENSOR

FIG. 1

POLYMER LAYER
(2~5 μm)

FIG. 2

POSITIVE PHOTORESIST
(0.5~1μm)

FIG. 3

FIG. 4

RED DYE DIFFUSE IN

FIG. 5

BLUE DYE DIFFUSE IN

.FIG. 6

GREEN DYE DIFFUSE IN
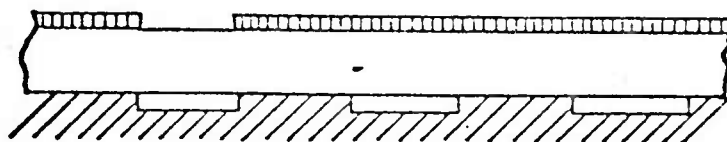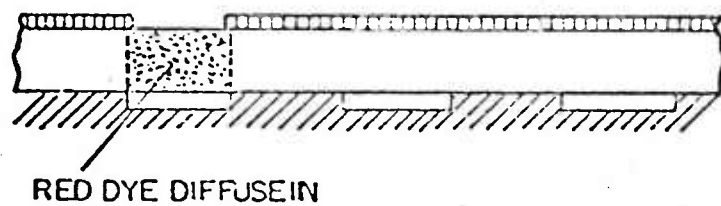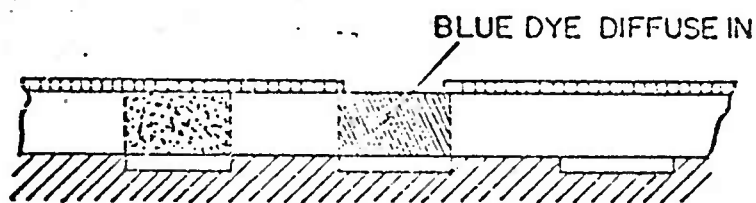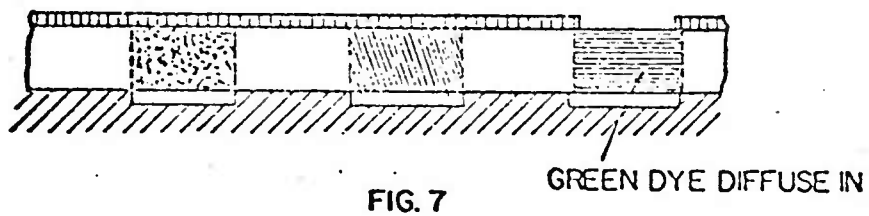
FIG. 7

(4.2)   Optical Waveguide Devices

Integrated optics is a rapidly developing field that could have an important impact on future optical communication systems [40]. The main objective is the development of a family of optical and electro-optical elements in a thin film planar form that will allow the integration of a large number of devices on a single substrate. To communicate using light, the beam is directed down an optical light guide. The guide consists of a tiny core surrounded by a lower refractive index medium. To propagate down the guide, the light beam must be reflected back into the core each time it hits the interface with the surface. Only light beams launched at certain angles, called critical angles, will do this. As long as the beam of light travels down a light guide and bounces off the interfaces so that it always makes an angle greater than the critical angle, it will be continuously reflected internally. In this way, tiny waveguide optical devices that can modulate, filter, multiplex, and switch optical signals have been fabricated. Some have been built monolithically into the same multilayer semiconductor structures used to make the injection lasers that act as light sources. Some are hybrid devices using waveguides diffused into electrooptic crystals, particularly lithium niobate. But even the most advanced semiconductor waveguides need a series of fabrication procedures which are photolithography, mask addressing and diffusion.

In many ways, guided wave optics technology today has demonstrated the ability to integrate multiple devices onto a single chip and to simplify the fabrication. From research experience, it may be possible to use a polymer as a waveguide component and apply the newly derived laser-addressing lithographic techniques to fabricate such optical devices.

There are two requirements in the choice of polymer materials. First polymers must have a high refractive index, larger than 1.45. Poly (methyl methacrylate) (n=1.49), poly (butadiene) (n=1.50), poly (urethane) (n=1.5-1.6) and poly (ethylene) (n=1.5-1.55), etc., [41] having high refractive indices, are the possible polymer materials which can be used as the waveguides. Secondly, a polymer must be ultraviolet curable. Examples are (1) a mixture of carboxylated butadiene and acrylonitrile copolymer with photosensitive elements [42], (2) a mixture of non-crystallizing polyurethane elastomer with 1-butene-3,4-diol [43], and (3) a mixture of polyethylene and poly (ethylene/acryloxybenzophenone) blended with a light sensitizer [44].

The method of making a polymer waveguide involves the following steps: (i) coating a thin layer of polymer onto the metallized substrate, (ii) exposing this polymer thin film under the laser addressing system by accurate computer control, and (iii) dissolving the unexposed part of the

polymer by isooctane and etching the exposed metal using a suitable etchant. The remaining structure, a polymer micro-structure with a metal layer beneath, will be the waveguide component.

II. CURRENT STATES

Experiments have been carried out to produce polymeric microstructures which behave as optical wave guides. The polymer, PDMS, was crosslinked using a UV laser beam.

The polymer solution comprising , 97% by weight, of a polymer of PDMS and a mercapto-substituted methyl siloxane with 3% initiator, and 3% by weight of vinyl functional siloxane, was spun onto glass and silicon substrates to produce a uniformly thick film. The diluant employed to facilitate spinning was isooctane. The films were spun at 2000 rpm for 30 seconds in order to produce films of 6-8 microns thickness. In most experiments thin metal films were first deposited on the substrates to confine the guided wave to the film.

After baking for one minute, the polymer film was cross-linked in the desired regions using an UV beam from an Ar+ ion laser. The incident beam had a wavelength range from 351.1 nm to 363.8 nm. The beam was focused onto the substrate using a microscope lens. We employed 47.5 magnification to give a spot size of 2 microns with a depth of focus of 7.4 microns.[57]

The substrate was mounted on a stepper - motor stage system capable to one μm linear septs. and $0.01°$ rotation increments. Patterns (linear and curved) were written by controlling the mechanical motion of the stages (two linear, one rotational),

and the shutter opening with a computer.

After development in hexane, we are left with the required guide since PDMS acts like a negative resist. Different patterns of varying width have been produced. Lines as thin as 2 μm have been produced.[57] Figure 1 is a block diagram of the exposure system employed. Figure 2 has photographs of a few structures made by this laser lithography method.

The polymer solution has been doped with Rhodamin 6G dye and crosslinked. Absorption and emmission plots were then made. It was found that light corresponding to 530 nm was absorbed while light corresponding to 555 nm was emmitted. The absorption and emisiion plots are given in Figure 3. It appears that polymeric microstructures could host dye lasers as a component in a highly integrated optical system.

60 micron wide channel structures were then fabricated on glass substrates and these were found to guide light. In order to reduce trapped light in the substrate it was decided to employ metallized silicon wafers.

To facilitate coupling light into the structures, the guides were made 30 - 60 microns wide. To measure the transmission characteristics of the wave guides, a He Ne laser was employed. as the light source. The substrate was held on a vacuum check which was capable of motion in the X,Y,Z directions, as well as rotary motion in the XY plane. A photodiode was employed to measure the output intensity of the guide. Data was collected

on curved structures in order to overcome the problem of light entering the diode directly from the source.

.From data collected it was observed that the intensity of the transmitted light decreased exponentially along the guide. Mathematically the decay could be expressed as

$$I = I \exp(-2kl)$$

where

I is the output intensity

I is the input intensity

k is the amplitude decay constant

l is the length of the guide.

The average value observed for the amplitude decay constant was 0.05 mm^{-1}. [60]

As a silicon wafer is employed as the substrate it was decided to fabricate a photodiode in the substrate. This will lead to more accurate measurement of the output intensity and will be a step forward in creating highly integrated optical systems.

. Experiments have also been underway to study the electron beam crosslinking characteristics of PDMS. It was felt that with the higher resolution available in the EBF, the structure formed will have fewer distortions or 'unwanted growth'[58,59] and the cross section will be more rectangular. Experiments conducted thus far have had very promising results and it is planned to study effect of 'dosage' on structure characterisitics.

FUTURE

The future for a highly integrated system seems very promising work will be centered around the following points:

1. Application of wave guides to various electronic requirements such as switches, optical couplers, displays, etc. (Ref. 3,6).

2. Fabrication and characterization of dye lasers.

3. Characterization of the optical wave guides fabricated from PDMS in terms of dependence of the amplitude decay constant on the incident wave length and also the chemistry of the guide employed - role of substituent groups in polysiloxane.

4. E beam or UV processibility of other siloxane polymers especially by laser lithography or in a EBF (ref.4,5).

APPENDIX A : THE CHOICE OF MATERIALS IN METALLIZATION

For high quality reproduction of images, the polymer microelectronic devices require a large reversible deformation of the elastomer and a highly reflective metallic coating. It is necessary to use very thin metal contacts so that the metal does not contribute appreciably to the deformation of the elastomer. To solve this problem, a new technique [3] was developed in which the contacts were deposited on the silicone polymers at 100 K. At this temperature, the silicone is in the glassy state [45]. Thin reflective metal films can be produced by a technique which involves the evaporation of metal onto a polymer surface that has been cooled below its glass transition temperature via a liquid nitrogen reservoir in thermal contact with the polymer. With the cryogenic techniques, deformable components with highly reflective and conducting metal surfaces have been prepared.

Gold, indium, aluminum, and silver films have been investigated for their possible use in the low temperature evaporation process. The properties to be optimized were the conductance and reflectance of the films. An summary of the properties of the metals is provided in Table (A-1). This provides the information necessary to substantiate the choice of the metal best fitted for the reflecting surface.

TABLE A-1

Properties of Materials Used in Vacuum Technology

	Melting* Point (K)	Evaporation* Temperature at 10^{-5}torr (K)	Coefficient* of linear thermal expansion (K^{-1})	Young's* Modulus (Pa)	Electrical* Resistivity $(\Omega \cdot m^2)$	Intrinsic** Stress (Pa)
Aluminum (Al)	933	1160	2.4×10^{-5}	5.7×10^9 to 6.9×10^9	2.8×10^{-2}	1.0×10^7 to 1.2×10^8
Copper (Cu)	1356	1210	1.65×10^{-5}	1.1×10^{11} to 1.2×10^{11}	1.7×10^{-4}	2×10^8 to 4×10^8
Gold (Au)	1336	1305	1.42×10^{-5}	7.9×10^{10}	2.35×10^{-4}	1×10^8 to 3×10^9
Indium (In)	1835	937	3.3×10^{-5}	1.1×10^{10}	9.0×10^{-2}	5.0×10^6
Silver (Ag)	1234	1025	1.9×10^{-5}	5.9×10^{10} to 7.8×10^{10}	1.59×10^{-2}	2.0×10^7 to 1.0×10^8

* From Reference 46.

** From Reference 48.

The literature [46] indicates that gold films have good conductivity. However, they have a high transmittance [47] in the visible region, thus the reflectivity is lower than that of the other metals. Silver, aluminum, and indium have been reported [47] to have low transmission in the optical region and therefore are good candidates for reflecting films. Although the silver films have the best reflectance of the four metals, the silver surface was reported to degrade in time and is reported to degrade rapidly in sulpher-containing environments [47]. As far as transmission losses are concerned, the best metals to use are aluminum and indium.

Surface reflectance was also found to depend upon the stress history of both the substrate and the metal film. The stress contributions between the metal and the polymer are very complex. Here, only two simplified contributions are discussed.

The first contribution is intrinsic stress, which arises from film contamination and incomplete structural ordering processes occuring during film growth. These stresses are dependent upon the thickness, the condensation rate and the deposition temperature. Values of these stresses for the metals of interest are listed in the last column of Table (A-1) for films approximately 100 nm thick. The indium films have the lowest value of the intrinstic stress which corroborates the fact that the indium films are

uniform for both ambient and low temperature substrates.

The second contribution to stress history comes from the different thermal expansion coefficients of both the metal and the polymer that occur as the substrate and metal are allowed to equilibrate from a low temperature to an ambient one. The thermal strain e_T, that occurs between the metal and the polymer layer is given by

$$e_T = (\alpha_f - \alpha_s) \Delta T \qquad\qquad (A-1)$$

where α_f and α_s are the average coefficients of expansion for the films and the substrate respectively and ΔT is the temperature difference in the substrate during evaporation relative to room temperature. The silicone polymer has a thermal expansion on the order of $10^{-4} K^{-1}$[48] and the metal has one of $10^{-5} K^{-1}$ (Table (A-1)). Thus, when the temperature returns from a low temperature to an ambient one, the low strength metal film will crack due to the expansion of the polymer.

Table (A-1) shows that indium has the lowest modulus and it was observed in the experiments that indium does not crack as readily as the other metals. Thus, indium has both good reflectivity and thermomechanical properties for the low temperature process.

APPENDIX B : ELECTRONIC BREAKDOWN VOLTAGE

In applying polymers as an insulating layer in elec-
tronic devices, it is of practical importance to understand
the limitations in usefulness of these materials as insula-
tors. In particular, there exists a critical voltage gradi-
ent across the materials above which the polymer no longer
acts to insulate the electrical conductor. The critical
voltage gradient across the polymer is referred to as its
electric strength or breakdown strength. Knowledge of the
breakdown voltage (or strength) is very important for the
design of the microelectronic components.

Several authors [8,9,49,50] have presented experimental
breakdown results on polymers. For most polymer materials,
the dielectric strength is between 10^5 and 10^7 V/cm. If it
is assumed that the dielectric strength is independent of
film thickness [51], then

$$V_d = E_d \times D \qquad\qquad (B-1)$$

where V_d is the breakdown voltage, E_d is the dielectric
strength of the material, and D is the thickness of the
insulting layer.

It was the purpose of this research to find out the
possible breakdown mechanism which might destroy the devices
and determine the maximum voltage (D.C.) which could be
applied to a silicone microstructure.

Siddell [52] showed that the breakdown frequently originates at pinholes, voids and defects in the film where electrode materials can move through to short them out. Impurities [53], especially as a second phase, and inhomogeneities at electrodes can lower E [54], by providing local regions of enhanced electrical stress. As discussed by Klein and Gafin [54], three types of breakdowns are common with carefully prepared films: local, self-propagating and maximum voltage breakdowns. First, if a voltage is supplied, the breakdown points can travel randomly across the electrodes. This self-propagating breakdown can give a characteristic tree pattern on the electrode and is illustrated in Figure (B-1). Second, the insulator can short at weak points, caused by dust,etc. on the surface of the substrate (due to insufficient cleaning). Figure (B-2) illustrates this form of breakdown.

A simple experiment was set-up to determine the maximum voltage (D.C.) which could apply to the silicone polymer. First, a thin layer of Aluminum (100 nm) was evaporated on a clean microscope slide. Second, the silicone polymer (System A or System B) was spun onto the surface of the metal and was then exposed under the ultraviolet light for 15 minutes. After curing, the crosslinked polymer was metallized with a thin layer of Aluminum (6 nm) at 100 K. Finally, a D.C. voltage was applied across the two metallized layers. The deformation of the surface was observed under the microscope.
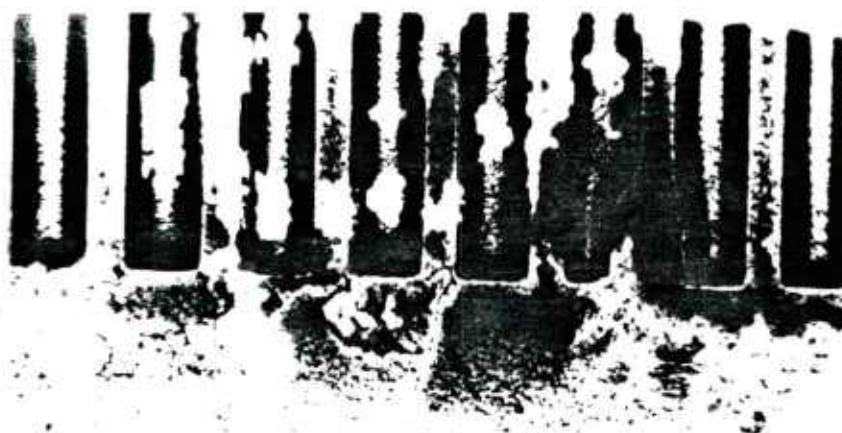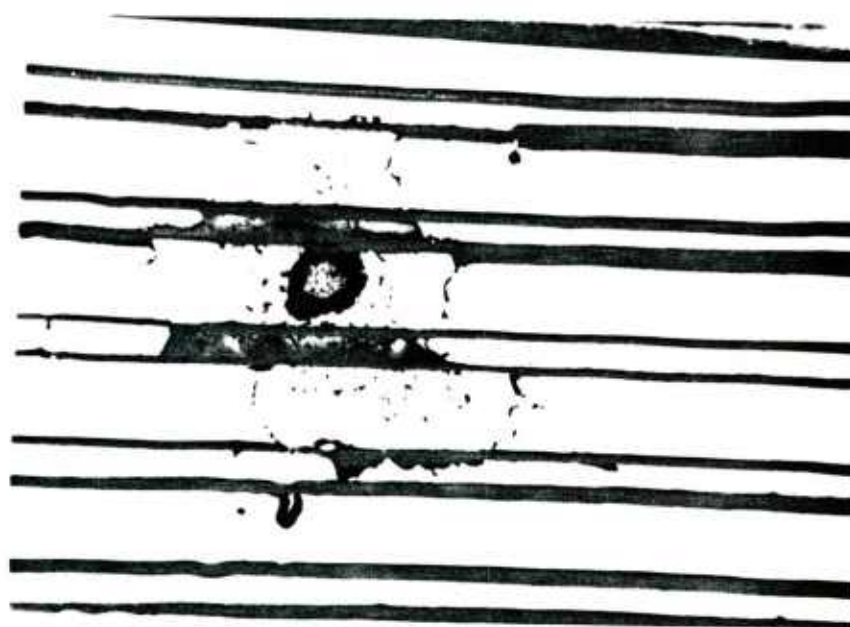
FIGURE B-1   Self-Propagating Breakdown
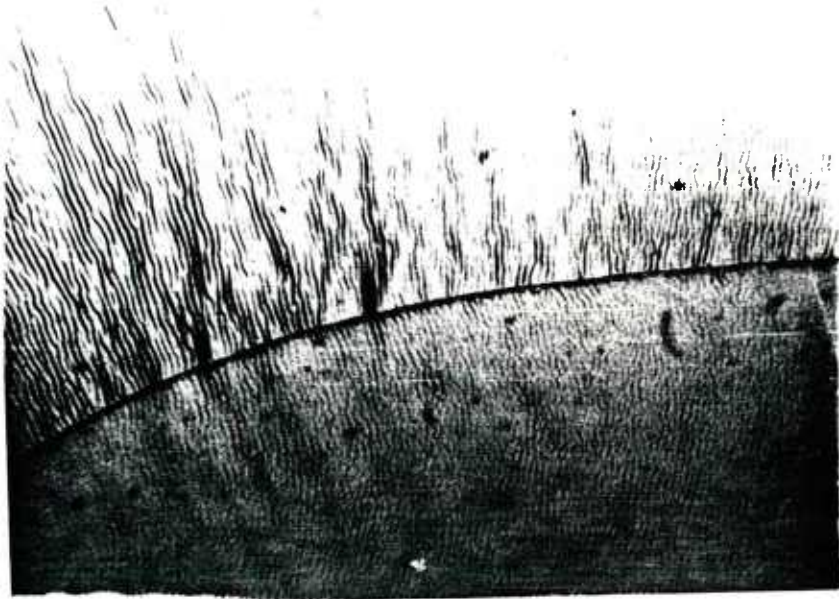

FIGURE B-2   Electrostatic Breakdown

FIGURE B-3

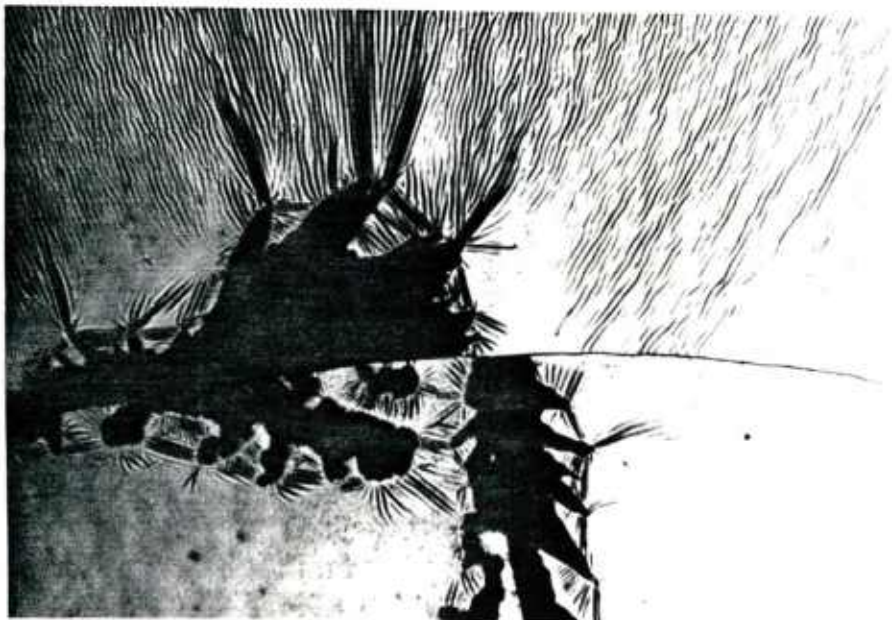Metallized Polymer Surface (before applying voltage)

FIGURE B-4

Metallized Polymer Surface (after applying voltage)

REFERENCES

1. M.G. Broadhurst, S. Edelman, and G.T. Davis, Org. Coat. and Plast. Chem. Prep., ACS Div. Org. Coat. Plast. Chem., 42, 241 (1980).

2. G.C. Martin, T.T. Su, P.Kornreich, and S.T. Kowel, Org. Coat. and Plast. Chem. Prep., ACS Div. Org. Coat. Plast. Chem., 43, 390 (1980).

3. S.T. Kowel, E. Balizer, T.T. Su, I.H. Loh, D. Cleverly, G.C. Martin, P.G. Kornreich, 'Polymeric Microelectronics', U.S. Army Report DAAK 70-80-C-0053-1 (1981).

4. T.T. Su, M.S. Thesis, Syracuse University (1981).

5. S.T. Kowel, and P.G. Kornreich, 'Polymer Microelectronics', Proposal submitted to the N.S.F., Syracuse University (1978).

6. G.C. Martin, T.T.Su, E.Balizer, I.H. Loh, S.T. Kowel, and P. Kornreich, J. Appl. Phys.. 53, 797 (1982).

7. J. Blok and D.G. LeGrand, J. Appl. Phys., 40, 288 (1969).

8. W.G. Lawson, Nature, 206, 1248 (1965).

9. K.H. Stark and C.G. Garton, Nature, 176, 1225 (1955).

10. P.J. Flory, "Principles of Polymer Chemistry", Cornell University Press, Ithaca, New York, 1953.

11. L.R.G. Treloar, "The Physics of Rubber Elasticity", 3rd Ed., Clarendon Press, Oxford, 1975.

12. J.E. Mark, J. Chem. Educ., 58, 898 (1981).

13. F. Rodriguez, J. Chem. Educ., 50, 764 (1973).

14. L.K. Nash, J. Chem. Educ., 56, 363 (1980).

15. J.E. Mark and P.J. Flory, Rubber Chem. Technol., 41, 1141 (1968).

16. P.J. Flory, Rubber Chem. Technol., 41, G41 (1968).

17. A.N. Gent, Wear, 29, 111 (1974).

18. L.S. Porter and E.A. Meinecke, Rubber Chem. Technol., 53, 1133 (1980).

19. A.N. Gent and E.A. Meinecke, Polym. Eng. Sci., 10, 48 (1970).

20. A.N. Gent, J. Polym. Sci., Polym. Symp., 48, 1 (1974).

21. A.N. Gent, R.L. Henry, and M.L. Roxbury, J. Appl. Mech., 41, 855 (1974).

22. F.R. Eirich, "Science and Technology of Rubber", Academic Press, New York, 1978.

23. R.V. Southwell, "An Introduction to the Theory of Elasticity", Clarendon Press, Oxford, 126, 1941.

24. J.E. Long, "Bearings in Structural Engineering", Wiley, New York, 12, 1974.

25. J.M.Schultz, "Polymer Materials Science", Prentice-Hall Press, New Jersey, 1974.

26. "Silicon Compounds Register & Review", Petrarch System Inc., 1980.

27. K.E. Polmanteer, Rubber Chem. Technol., 54, 1051 (1981).

28. Personal communication with Dr. Y.John Chou, Dow Corning Corporation. (Oct. 21, 1981).

29. L.T. Thompson,and R.E. Kerwin, Ann. Rev. Mat. Science, 6,267 (1967).

30. O.S. Heavens , "Optical Properties of Thin Solid Films", Butterworth Scientific Publications, London, 227, 1955.

31. A.E. Brenneman, A. V. Brown, M.Hatzakis, A.J. Speth, and R.F.M. Thornley, IBM J. Res. Dev., 11, 520 (1967).

32. S.T. Kowel, J. Franklin Inst., 297, 135 (1974).

33. M. Lacombat,G. M. Dubroeucq, J. Massin, and M. Brevignon, Solid State Technol., 8, 115 (1980).

34. A. Yariv, "Quantum Electronics", 2nd ed., Wiley, New York, 113, 1975.

35. L. Levi, "Applied Optics", Wiley, New York, 468, 1968.

36. Dow Corning Corporation, Midland Michgan.

37. R.A. Becker, B.L. Sopori, and W. S. C. Chang, Appl. Opt., 17, 1069 (1978).

38. T.W. Martin, M.A. Sandhu, and D.J. Savage; "Photocrosslinkable, High-Temperature-Resisted Polymers and Their use in Color Imaging Devices", U.S. Patent 4,267,961 (1981)

39. A.T. Brault, W.A. Light, and T.W. Martin; "Method for Making A Solid-State Color Imaging Device Having a Integral Color Filter and the Device", U.S. Patent 4,081,277 (1978).

40. R. Cohen, High Technology, $\underline{1}$(2), Nov./Dec. (1981).

41. L. Bohn, "Polymer Handbook", ed. by J. Brandrup and E.H. Immergut, 2nd ed., Wiley, New York, II-241, 1975.

42. S. Proskow; "Photosensitive Compositions Containing Thermoplastic Ionomeric Elastomers Useful in Flexographic Printing Plates", U.S. Patent 4,272,608 (1981).

43. P. Richter, H. Stutz, L.Metzinger, O. Volkert, H. Werther, and A. Wigger; "Laminates for the Manufacture of Flexographic Printing Plates", U.S. Patent 3,948,665 (1978).

44. R. Ikeda, ed., "Ultraviolet Light Induced Reaction in Polymers", ACS Symposium Series 25, Wiley, New York, 1972.

45. J.M. Cowie and I.J. McEwen, Polymer, $\underline{14}$, 423 (1973).

46. L. Marton and C. Marton, ed., "Methods of Experimental Physics", $\underline{14}$, Ch. 8, Academic Press, New York, 1979.

47. W. Goldie, "Metallic Coating of Plastics", Vol. 1, Electro-Chemical Publications, England, 1968.

48. R.W. Hoffman, "Physics of Thin Films", ed. by G. Hass and R. Thun, Academic Press, New York, $\underline{3}$, 211, 1966.

49. J. Blok and D.G. LeGrand, J. Appl. Phys., $\underline{40}$, 288 (1968).

50. Y. Inuishi and D.A. Powers, J. Appl. Phys., $\underline{28}$, 1017 (1957).

51. L.I. Maissel and R. Glang, "Handbook of Thin Film Technology", McGraw-Hill, New York, 1970.

52. G. Siddall, Vacuum, $\underline{9}$, 274 (1959).

53. G.C. Wood and C. Peason, Corrosion Sci., $\underline{7}$, 119 (1967).

54. R. Cooper, Brit. J. Appl. Phys., $\underline{17}$, 149 (1966).

55. N. Klein and H. Gafni, IEEE Trans. Electron Devices, $\underline{Ed-13}$, 281 (1966).

56. P.F. Bruins, "Silicone Technology", Applied Polymer Symposia No.14, Interscience Publishers, New York, 1970.

57. I.H. Loh, The Fabrication and Characterization of Polymer Microelectronics Devices, MS Thesis Syracuse University July 1982.

58. E.D. Roberts, E. Beam Crosslinking of Positive and Negative Resists, Phillips Tech. Rev., v35, n2-3, 1975, pp. 41-52.

59. E.D. Roberts, Preparation and Properties of a Polysiloxane Electron Resist, J. Electochemical Soc., v120, n12, Dec. 1973, pp. 1716-21.

60. Dror Sarid, Analysis of Bistability in a Ring Channel Waveguide, Optics Letters, Vol. 6, 1981, pp. 552-553.

NOMENCLATURE

A	sample area under stress
Δb	depth of focus
C	capacitance
D	thickness of microstructure prior to deformation
d	thickness of microstructure after deformation
d_ℓ	diameter of the light beam
Δd	deformation (D-d)
E	tensile modulus
E_d	dielectric strength of the materials
E_e	electrical energy
E_s	strain energy of the polymer gels
E_t	total energy stored in the deformed microstructure
e_T	thermal strain
F	F number of the lens (f/d)
F_e	electrical force
F_s	mechanical force
F_z	force along the Z-direction
F_1	homogeneous compression force
F_2	the additional force due to the hydrostatic pressure in the interior of the rubber
f	lens focus length
f_1	force per unit area
f_ℓ	constant coefficient

G	shear modulus
H	strain energy per unit volume
K	numerical factor (3/4)
n	refractivity index
P	hydrostatic pressure
s	minimum focused beam spot size
S	shape factor
T_g	glass transition temperature
V	applied voltage
V_d	breakdown voltage
V_m	maximum applied voltage
W	width of the microstructure
x	displacement of the interference fringe
α_f	thermal expansion coefficient for the films
α_s	thermal expansion coefficient for the substrate
λ	light wavelength
λ_x	linear extension ratio in X-direction
λ_y	linear extension ratio in Y-direction
λ_z	linear extension ratio in Z-direction
ϵ	dieletric constant of the polymer gel
ϵ_0	permittivity constant
θ	angular divergence of the laser beam